UNIVERSITI SAINS MALAYSIA

Laporan Akhir Projek Penyelidikan Jangka Pendek

Study On The Cooling Performance Of Multi Piezoelectric Fans on The High on The Powered Light Emitting Diod (LED) For Different Arrangement

by
Prof. Ir. Dr. Mohd Zulkifly Abdullah
Dr. Nadiahnor Md. Yusop
Dr. Farzad Ismail

2015

UNIVERSITI SAINS MALAYSIA

UNIVERSITY RESEARCH GRANT FINAL REPORT
Geran Penyelidikan Universiti Laporan Akhir

A.	**PARTICULARS OF RESEARCH** / *MAKLUMAT PENYELIDIKAN:*
(i)	**Title of Research: Study on the cooling performance of multi piezoelectric fans on high powered light emittiing diode (LED) for different arrangement** *Tajuk Penyelidikan:*
(ii)	**Account Number: 1001/PMEKANIK/814163** *Nombor Akaun:*
B.	**PERSONAL PARTICULARS OF RESEARCHER** / *MAKLUMAT PENYELIDIK:*
(i)	**Name of Research Leader: Prof. Ir. Dr. Mohd Zulkifly bin Abdullah** *Nama Ketua Penyelidik:*
	Name of Co-Researcher: Dr. Nadiahnor Md. Yusop **Dr. Farzad Ismail** *Nama Penyelidik Bersama:*
(ii)	**School/Institute/Centre/Unit : School of Mechanical Engineering** *Pusat Pengajian /Institut/Pusat/Unit :*
C.	**Research Platform (Please tick (/) the appropriate box):** *Pelantar Penyelidikan (Sila tanda (/) kotak berkenaan):* [ ] **A. Life Sciences** *Sains Hayat* [ ] **B. Fundamental** *Fundamental* [√] **C. Engineering & Technology** *Kejuruteraan & Teknologi* [ ] **D. Social Transformation** *Transformasi Sosial* [ ] **E. Information & Communications Technology (ICT)** *Teknologi Maklumat & Komunikasi* [ ] **F. Clinical Sciences** *Sains Klinikal* [ ] **G. Biomedical & Health Sciences** *Bioperubatan Sains Kesihatan*

D. **Duration of this research :**
Tempoh masa penyelidikan ini :

***Duration :** .....3 Years.....
Tempoh :

From : .....15 July..... 2015__ **To** : .....14 July..2015
Dari: *Ke :*

E. **ABSTRACT OF RESEARCH**

(An abstract of between 100 and 200 words must be prepared in **Bahasa Malaysia and in English**. This abstract will be included in the Annual Report of the Research and Innovation Section at a later date as a means of presenting the project findings of the researcher/s to the University and the community at large)

Abstrak Penyelidikan

(Perlu disediakan di antara 100 - 200 perkataan di dalam **Bahasa Malaysia dan juga Bahasa Inggeris**.
Abstrak ini akan dimuatkan dalam Laporan Tahunan Bahagian Penyelidikan & Inovasi sebagai satu cara untuk menyampaikan dapatan projek tuan/puan kepada pihak Universiti & masyarakat luar).

Kipas piezoelektrik (kipas getaran) adalah mesin getaran mikro yang beroperasi digunakan sebagai alat penjana aliran angin bagi membantu menghilangkan haba pada peranti mikroelektronik. Peranti ini adalah boleh-percaya, mempunyai jangka hayat yang tinggi, memerlukan kuasa rendah, bebas bising dan boleh digunakan pada ruang yang kecil. Dalam kajian ini, gabungan analisis eksperimen dan berangka telah dijalankan untuk mengkaji prestasi kipas piezoelektrik sebagai fungsi pembebasan haba. Kajian pengetar laser digunakan untuk menentukan frekuensi tegun kipas getaran. Kajian pengukur halaju imej zarah menunjukkan medan aliran terhasil dengan kombinasi susunan berbeza kipas bergetar. Simulasi 3D berdasarkan skim jejaring dinamik dijalankan menggunakan perisian FLUENT dan ABAQUS bersama kod gabungan anataramuka MpCCI bagi mengkaji perubahan fana keatas suhu dan medan aliran terhasil dengan kipas getaran. Kaedah ini juga digunakan pada sebuah penyejukan untuk membebaskan haba daripada pakej LED berkuasa tinggi. Pakej LED terdedah secara langsung pada susunan dual kipas bergetar mengikut konfigurasi A (susunan buju ke buju kipas) dan konfigurasi B (susunan muka ke muka kipas). Ia mendapati dua kipas telah meningkatkan prestasi pemindahan haba lebih kurang 2.3 kali bagi konfigurasi A dan 2.4 kali bagi konfigurasi B. Kombinasi penyerap haba dengan dua dan empat kipas bergetar untuk menyejukkan pakej LED bagi memaksimumkan pembebasan haba telah dijalankan. Kajian ini menunjukkan kipas piezoelektrik mampu digunakan dalam pengurusan terma bagi susunan LED dan boleh dicadangkan dalam penggunaan bagi menyejukkan cip LED komersial. Pada keadaan ini, peningkatan pemalar pemindahan haba melebihi 88% tercapai berbanding melalui proses perolakan tabie.

Piezoelectric fans (vibrating fans) are micro vibrating machines that can be potentially used as airflow generators to help dissipate heat in microelectronic devices. They are reliable, have longer life span, consume low power, noise-free and it's adaptable in very small spaces. In this work, a combination of experimental and numerical analyses (CFD) was performed to investigate the performance of piezoelectric fans on heat dissipation function. Laser vibrometer study was carried out to determine the resonance frequency of vibrating fans. Particle image velocimetry study presented the flow field induced by combination of different vibrating fans arrangements. 3D simulations based on a dynamic meshing scheme were performed in FLUENT and ABAQUS with the use of code coupling interface MpCCI to investigate transient changes on the temperature and flow fields achieved by vibrating fans. This successful approach was then exploited as a cooling device to dissipate heat from high power LEDs package. The LEDs package were directly exposed to the dual vibrating fans arranged according to configuration A (for edge to edge fans arrangement), and configuration B (for face to face fans arrangement). It was found that the dual fans enhanced heat transfer performance approximately by 2.3 times for configuration A and 2.4 for configuration B. Combination of heat sink with dual and quadruple vibrating fans to cool the LEDs package for maximizing the heat dissipation was also explored. This research has established the ability of piezoelectric fans for thermal management of LEDs arrays and recommends it for use as commercial cooling of LEDs chips. At this condition, an enhancement in convective heat transfer coefficient exceeding 88% is achieved, compared to natural convection.

F. **SUMMARY OF RESEARCH FINDINGS**

Ringkasan dapatan Projek Penyelidikan

Piezoelectric fans (vibrating fans) are micro vibrating machines that can be potentially used as airflow generators to help dissipate heat in microelectronic devices. They are reliable, have longer life span, consume low power, noise-free and it's adaptable in very small spaces. In this work, a combination of experimental and numerical analyses (CFD) was performed to investigate the performance of piezoelectric fans on heat dissipation function. Laser vibrometer study was carried out to determine the resonance frequency of vibrating fans. Particle image velocimetry study presented the flow field induced by combination of different vibrating fans arrangements. 3D simulations based on a dynamic meshing scheme were performed in FLUENT and ABAQUS with the use of code coupling interface MpCCI to investigate transient changes on the temperature and flow fields achieved by vibrating fans. This successful approach was then exploited as a cooling device to dissipate heat from high power LEDs package. The LEDs package were directly exposed to the dual vibrating fans arranged according to configuration A (for edge to edge fans arrangement), and configuration B (for face to face fans arrangement). It was found that the dual fans enhanced heat transfer performance approximately by 2.3 times for configuration A and 2.4 for configuration B. Combination of heat sink with dual and quadruple vibrating fans to cool the LEDs package for maximizing the heat dissipation was also explored. This research has established the ability of piezoelectric fans for thermal management of LEDs arrays and recommends it for use as commercial cooling of LEDs chips. At this condition, an enhancement in convective heat transfer coefficient exceeding 88% is achieved, compared to natural convection. The output of the project:

1) One PhD student - graduated in 2014
2) One MSc student- graduated in 2013
3) 4 papers are published in International journals with ISI impact
4) Established networking with Dept. of Mechanical Eng., Prince Songkhla University, Hatyai, Thailand.
5) Experimental facility for piezoelectric study was developed in Aerodynamic Laboratory, school of Aerospace Eng.

G. **COMPREHENSIVE TECHNICAL REPORT**

Laporan Teknikal Lengkap

Applicants are required to prepare a comprehensive technical report explaining the project.
(This report must be attached separately)
Sila sediakan laporan teknikal lengkap yang menerangkan keseluruhan projek ini.
[Laporan ini mesti dikepilkan]

List the key words that reflectour research:

Senaraikan kata kunci yang mencerminkan penyelidikan anda:

English	Bahasa Malaysia
LED package cooling	Penyejukan pakej LED
Piezoelectric fans	Kipas piezoelektrik
Fan synchronization	Kipas mengaktifakan

H. a) **Results/Benefits of this research**
Hasil Penyelidikan

No. *Bil:*	Category/Number: *Kategori/ Bilangan:*	Promised	Achieved
1.	**Research Publications (Specify target journals)** *Penerbitan Penyelidikan (Nyatakan sasaran jurnal)*	4	4
2.	**Human Capital Development**		
	a. Ph. D Students	**1**	**1**
	b. Masters Students	**1**	**1**
	c. Undergraduates (Final Year Project)	**0**	**0**
	d. Research Officers		
	e. Research Assisstants		
	f. Other: Please specify		
3.	**Patents** *Paten*	0	0
4.	**Specific / Potential Applications** *Spesifik/Potensi aplikasin*		
5.	**Networking & Linkages** *Jaringan & Jalinan*	1	1
6.	**Possible External Research Grants to be Acquired** *Jangkaan Geran Penyelidikan Luar Diperoleh*		

- Kindly provide copies/evidence for Category 1 to 6.

b) Equipment used for this research.
Peralatan yang telah digunakan dalam penyelidikan ini.

Items *Perkara*	Approved Equipment	Approved Requested Equipment	Location
Specialized Equipment Peralatan khusus	1 unit IR Thermal Imaging Camera	1 unit IR Thermal Imaging Camera	Aerodynamic Laboratory, PPKAero
Facility Kemudahan			
Infrastructure Infrastruktur			

- Please attach appendix if necessary.

I. **BUDGET** / *BAJET*

Total Approved Budget	: RM 175,318.00
Total Additional Budget	: RM -
Grand Total of Approved Budget	: RM 175,318.00

Yearly Budget Distributed

Year 1	: RM 80,518.00
Year 2	: RM 58,400.00
Year 3	: RM 36,400.00

Additional Budget Approved

Year 1	: RM
Year 2	: RM
Year 3	: RM

Total Expenditure	: RM 175,318.00
Balance	: RM 175,318.00

- **Please attach final account statement from Treasury**

Signature of Researcher
Tandatangan Penyelidik

11-7-2016
Date
Tarikh

H.	**COMMENTS OF PTJ'S RESEARCH COMMITTEE** *KOMEN JAWATANKUASA PENYELIDIKAN PERINGKAT PTJ*

General Comments:
Ulasan Umum:

The research team has made an excellent contribution with four high impact journal publications and two postgraduate students.

.....

Signature and Stamp of Chairperson of PTJ's Evaluation Committee
Tandatangan dan Cop Pengerusi Jawatankuasa Penilaian PTJ

PROFESOR DR. MANI MARAN A/L RATNAM
Deputy Dean
(Research, Postgraduate & Networking)
School of Mechanical Engineering
Universiti Sains Malaysia, Kampus Kejuruteraan
14300 Nibong Tebal, Pulau Pinang.

Date : .....
Tarikh : .....

Signature and Stamp of Dean/ Director of PTJ
Tandatangan dan Cop Dekan/ Pengarah PTJ

PROF. ZAINAL ALIMUDDIN B. ZAINAL ALAUDDIN
Dean
School of Mechanical Engineering
Engineering Campus
Universiti Sains Malaysia
14300 Nibong Tebal, Pulau Pinang.

Date : .....
Tarikh : .....

FINAL REPORT

Research Title: **Study on the cooling performance of multi piezoelectric fans on high powered light emitting diode (LED) for different arrangement**

Grant no : 1001/PMEKANIK/814163

Researchers:

Professor Ir. Dr. Mohd Zulkifly bin Abdullah (Leader)
Dr. Nadiahnor Md. Yusop
Dr. Farzad Ismail

Executive Summary

Piezoelectric fans (vibrating fans) are micro vibrating machines that can be potentially used as airflow generators to help dissipate heat in microelectronic devices. They are reliable, have longer life span, consume low power, noise-free and it's adaptable in very small spaces. In this work, a combination of experimental and numerical analyses (CFD) was performed to investigate the performance of piezoelectric fans on heat dissipation function. Laser vibrometer study was carried out to determine the resonance frequency of vibrating fans. Particle image velocimetry study presented the flow field induced by combination of different vibrating fans arrangements. 3D simulations based on a dynamic meshing scheme were performed in FLUENT and ABAQUS with the use of code coupling interface MpCCI to investigate transient changes on the temperature and flow fields achieved by vibrating fans. This successful approach was then exploited as a cooling device to dissipate heat from high power LEDs package. The LEDs package were directly exposed to the dual vibrating fans arranged according to configuration A (for edge to edge fans arrangement), and configuration B (for face to face fans arrangement). It was found that the dual fans enhanced heat transfer performance approximately by 2.3 times for configuration A and 2.4 for configuration B. Combination of heat sink with dual and quadruple vibrating fans to cool the LEDs package for maximizing the heat dissipation was also explored. This research has established the ability of piezoelectric fans for thermal management of LEDs arrays and recommends it for use as commercial cooling of LEDs chips. At this condition, an enhancement in convective heat transfer coefficient exceeding 88% is achieved, compared to natural convection. The output of the project:

1) One PhD students - graduated in 2014
2) One MSc student- graduated in 2013
3) 4 papers are published in International journals

4) Established networking with Dept. of Mechanical Eng., Prince Songkhla University, Hatyai, Thailand.
5) Experimental facility for piezoelectric study was developed in Aerodynamic Laboratory, school of Aerospace Eng.

1.0 Introduction

Modern day gadgets such as computers, LED packages and portable electronic devices (mini-laptops, tablets, and cellular phones) are rapidly emerging in lighter, slimmer, and more compact forms with high functionalities to meet consumer demands. This tremendous growth in advance electronics necessitates modern solutions to be adapted with the new challenges of thermal management. Currently, the thermal management for such commercially available devices is mostly confined to passive cooling because of its typical simplicity in implementation. One such example is the thermal management of LED packages. LED is based on the principle of solid-state lighting (SSL) technology which converts electricity into visible light using semiconductors. Over the last 10 years, LED technology has seen tremendous progress on account of its numerous advantages over the traditional lighting sources. This success of LED will continue to dominate the lighting market; completely replace the traditional lighting and outperform the incandescent and the fluorescent lighting in future. Only a small portion of the LED power input converts into a visible light of particular wave length, and the rest appears as unwanted heat which seriously affects the maintainability of low LED die temperature.

Approximately 80% of the power that is applied to LED is converted into unwanted heat and must be dissipated to the ambient (Petroski, 2002). Therefore, thermal management has become the major issue related to high-power LEDs. In order to achieve longer lifetime, higher luminous efficacy and stable emission wavelength of light output, LEDs should be sustained in lower junction temperature (Shyu et al., 2011). Thus, in order to exploit these advantages, heat dissipation solutions for LEDs become crucial. It is well known that cooling efficiency is very low for passive cooling mechanism. Moreover, the modern electrical devices need higher heat dissipation requirements and their demands have significantly increased over time, which draws out attention towards more effective cooling techniques. Presently, the heat transfer enhancement methods are broadly classified as either active (e.g. piezoelectric fans, surface vibration, electric or magnetic fields, and so on) or passive (e.g. extended surfaces, swirl flow devices, vortex generators) (Lin, 2012). The piezoelectric fan stands out amongst all the methods due to its operational simplicity, small size and low power consumption.

The piezoelectric fan is an airflow generator that induces the flow with a vibrating flexible blade. It has recently been proposed as an alternative device for microelectronic cooling. It consists of a flexible blade bonded with piezoelectric material near its base end. An input signal applied to the piezoelectric material causes an oscillatory motion at the free end of the blade. This signal can induce the surrounding flow with low power consumption. Piezoelectric fan has several advantages and is an attractive thermal management alternative. It consumes very little power and can be typically operated in the range of 1-40 mW. This makes it an ideal choice for applications where power consumption is a key issue particularly for use in cell phone, PDA, or other mobile device. Another important advantage is that it can easily fit into any geometric constraint and make use of available volume. Significantly, this device is driven at frequencies under 100 Hz. Consequently, their acoustic energy and noise levels were very low to an extent

that their first mode of resonance was outside the range of frequencies audible to the human ear. This ensured near silent operation thereby avoiding unnecessary noise in the system. Another major advantage of this device when compared to a traditional rotary fan was that it had no moving parts, which ultimately led to longer life and better reliability.

Presently, LED cooling has been carried out using heat sinks and other passive cooling methods. (Jang et al., 2012) optimized the cooling performance and mass of a pin-fin radial heat sink for LED lighting applications. (Dehuai et al., 2012) improved the thermal characteristics of high-power LED package by using phase change heat sink. (Kim et al., 2007) reported the thermal characterization of high power LED arrays cooled by a heat pipe. In another work, (Li et al., 2013b) proposed a combination of loop heat pipe heat sink with dual complete parallel condensers for high power integrated LED cooling. These methods have limited scope and they are not very efficient.

The use of piezoelectric fan based cooling of LED's has never been carried out in any of the previous work. LED offers several advantages over other illumination devices and are therefore now very popular alternative. It is also well established that the performance of LED based electronic devices can be considerably improved at lower junction temperatures. The LED itself being low power consuming device, the use of conventional cooling techniques requiring higher power inputs is not justifiable. On the other hand, the piezoelectric fan based cooling technique has been proved to be very useful in several microelectronic cooling applications requiring very minimal power (AÇikalin et al., 2004). Combining these two major power saving devices not only would add to the efficiency of the LED's but would also reduce the overall power consumption to a very large extent.

1.1 Problem Statement

The exponential increase in miniaturization of electronic components and the growing demand for small scale tablet PC has put the focus on thermal management engineers. The heat dissipated from modern electronic devices is a major concern and is the driving force behind thermal management research. The conventional way to dissipate heat was to employ fan based forced convection technique. The small size electronic devices, increased heat flux on the processing platform and impetus on clean operation with minimal or no noise has propelled the need for improved cooling techniques that suit the modern electronic industries. Traditional rotary fans are no longer practical as it has reached their utmost limit in size reduction. Moreover, it requires large space, high power consumption, and the high speed moving parts cause noise and vibrations. Thus, it is very crucial to develop newer cooling techniques suiting the modern electronic devices for dissipation of associated heat generated.

Presently, piezoelectric fans, surface vibration, electric or magnetic fields are most widely used active cooling methods (Lin, 2012). Among all these methods, piezoelectric fans are very strong candidate for cooling the next generation microelectronic devices. It stands out amongst all the methods due to its operational simplicity, small size and low power consumption. Many studies have demonstrated its usefulness and discussed the related flow and thermal analysis of single piezoelectric fan (Liu et al., 2009). Despite the simple structure of piezoelectric fans, the airflow patterns developed by these fans have not been completely understood. Not much has been reported about the flow field induced on account of piezoelectric fan orientation.

Although, some studies on multiple piezoelectric fans have been carried out, but the underlying flow interaction and their optimized arrangement for best possible heat dissipation have not been given importance (Kimber and Garimella, 2009a). The flow field induced by two neighboring piezoelectric fans can be highly influenced by the vibration phase (Ihara and Watanabe, 1994). This calls for further investigations into the study of characteristic of multiple vibrating fans to assess the influence of different phase angles between two vibrating fans on the resulting flow and heat transfer. In addition to this, most of the researches with respect to multiple piezoelectric fans were based on the findings of dual fans. There is much to be realized on the appropriate arrangement of these fans for best possible heat transfer capabilities. Besides, the use of quadruple fans and their combination with heat sinks and performance of these fans at different power inputs have not been explored yet. In addition to this, most of the researchers focused the use of vibrating fans to cool a single heat source, whereas studies involving multiple heat sources (such as LEDs packages) have found no takers.

LED is an application of solid-state lighting (SSL) technology which converts electricity into a visible light by utilizing semiconductors. It is anticipated that LED will dominate the lighting market and outperform the incandescent and the fluorescent lighting in future, thereby replacing the traditional lighting sources completely. Light output of the conventional incandescent and newer compact fluorescent light bulb is much higher than the single LED output. As a result, multiple numbers of LEDs are used to be packaged in arrays to provide the preferred lighting for various applications of general illumination systems. Although, LED's have high luminous efficiency, about 80% of the power supplied is lost in the form of waste heat. It is highly recommended to maintain the junction temperature below 125°C (398K) to run the LED's for maximum lifetime(OSRAM, 2005). Therefore, the thermal problem caused by the heat generated within the LED itself constitutes an obstacle and limits the stability, reliability and lifetime of high power LED. It has been reported that, the average time to failure for most high power LED devices would reduce approximately by 50% when the specific operating junction temperature increases by an excess of (Zou et al., 2007). On the other hand, thermal behavior of LEDs packages is essentially affected by ambient temperature and multiple chips. Moreover, packaging the LED chips in small space causes increase in the thermal stresses. Therefore, it is necessary to develop LED packages with effective thermal design having very low thermal stresses in order to enhance the performance of LED. The advantages of dual piezoelectric fans in dissipate heat from LEDs package have not been studied. In addition to this, quadruple piezoelectric fan design for cooling of LEDs chips and their effectiveness in heat dissipation needs further investigation. Combining these two major power saving devices not only would add to the efficiency of the LED's but would also reduce the overall power consumption to a very large extent. This is the basic thrust of this research and as a part of this work several studies are carried out to evaluate the effect of using vibrating fans to cool LED arrays.

1.2 Research Objective

The main objectives of the present research are:

1. To carry out experimental studies to investigate the flow field induced by single and multi piezoelectric fans
2. To carry out 3D numerical simulation to estimate the transient flow and temperature profile of single and multiple piezoelectric fans

3. To study the transient flow field induced by single vibrating fan and thermal characteristics with different orientations of the fan over single heat source.
4. To examine the characteristics of different phase angles between dual vibrating fans on the resulting flow and heat transfer.
5. To investigate the thermal characteristics of high power LED array cooled by multiple vibrating fans.

1.2 Experimental Set-up and Procedure

A commercial piezoelectric fan consisting of a bimorph Lead Zirconate Titanate (PZT) patch bonded to a thin Stainless steel blade was used in this investigation for cooling purpose, due to its high elongation properties at relatively low power input (see Table 1 for the specifications).

TABLE 1 Specifications of the piezoelectric fan (Piezo Systems Inc., USA)

Specification	Value
Material	Stainless steel
Size (m)	0.047 (l_P)×0.012 (D_{pf})×0.0004 (t_P)
Height without patch (m)	0.023 (l_u)
Resonance frequency (Hz)	112
Power consumption (mW)	42
Weight (kg)	0.002

In this study the spacing effects on the piezoelectric fan were performance experimentally. The spacing between the neighboring walls and the fan side edges was defined as side gap (G_s), while the (δ) is the ratio of the fan tip spacing to the height of the side wall. The experimental procedure was performed with three tests; (A) measurements of piezoelectric fan amplitude by means of laser displacement sensor (KEYENCE LK-G152), (B) flow visualization using PIV technique, and (C) thermal analysis to assess the coupled effect of the δ and G_s on a heat surface (chip) with an objective of maximizing the heat dissipation.

1.2.1 Fan Amplitude Testing

A laser displacement sensor (KEYENCE LK-G152) was utilized to detect the fan tip deflection and also measure the amplitude. The measurement point of the focal laser beam to the fan surfaces was (2 mm) from the fan tip. A digital storage (DSO3062A Oscilloscope) connected with the inverter drive circuit were provided for tuning the frequencies and supplying the input signals to the fan. The inverter circuit was also joined with an input channel provided by a direct current (DC) dual power supply (GW instek GPS2303) to offer the voltages required for the fan operation and the other channel was fed the chip (heat source). The inverter circuit was used to convert a DC to AC to drive the piezoelectric fan, and the frequency was adjusted by turning the trimmer pot on the PCB. The piezoelectric fan was driven at the resonance frequency (approximately 112 Hz), with the input of 42mW. When the piezoelectric fan was running, the IMC DAQ system recorded the input displacement with frequency signal of the sensor, and collected it into the computer. The amplitude was measured for G_s values of 1mm to 11mm, with 1mm increment for each δ variation. The error of the displacement sensor was -/+ 0.02%.

1.2.2 Flow visualization

Particle image velocimetry (PIV) was employed to study the flow induced by the piezoelectric fan. The assembly of the piezoelectric fan and side walls was arranged inside a glass tunnel of size 50cm × 20cm×14cm. The flow was seeded by corn oil particles of diameters ranging from 1to 2 μm, using an atomizer Melling [18]. The PIV system consisted of a pulsed diode laser, a Flow Sense 2M 10bit camera, a synchronizing timing hub, and a Dell Precision Intel® Xeon™ CPU 3. 60GHz PC with 3.25 gigabytes of RAM. Flow Manager V4.6 Software was used to obtain images and compute the velocity fields. The flow was illuminated by a Nd: YAG laser (with a power of 850 mJ per pulse) which converted the IR light to visible green light of wavelength (λ) 532 nm. The laser cylindrical beam was adjusted into a thin sheet using a semi-cubical lens, and the sheet was horizontally steered into the test section. Images of the flow field were captured using a 1600 × 1186 pixel CCD camera with 10-bit intensity resolution. A Nikon 60 mm, 1:2.8D standard lens was used with variable zoom to obtain image magnifications lower than 3 μm / pixel. The laser sheet was positioned perpendicular to the camera to illuminate the flow particles from front (X-Y plane) side.

1.2.3 Experimental Set-up

The electronic package (chip) was imitated by an aluminum foil (size 52mm ×15mm ×1mm) which was heated with a uniform heat flux of 2610 W/m^2 by means of a stainless steel electrical heater attached beneath the foil. A heat sink compound RS® of highly conductivity was used to paste the heater with the foil. The foil-heater assembly was fixed into the cavity of a wooden platform such that, their top surfaces were coplanar. Two parallel adjustable side walls of 82mm length and 35mm height were arranged on the top surface of the platform on both sides of the foil. Fig. 1 and 2 are respectively shown the schematics of the experimental set up.

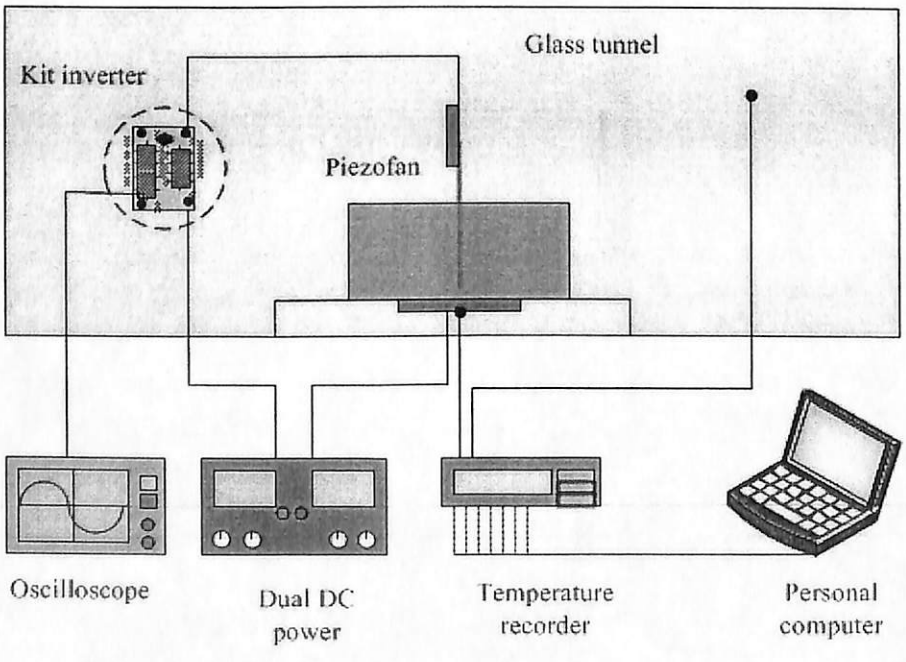

Fig. 1 Schematic of experimental setup for heat transfer study.

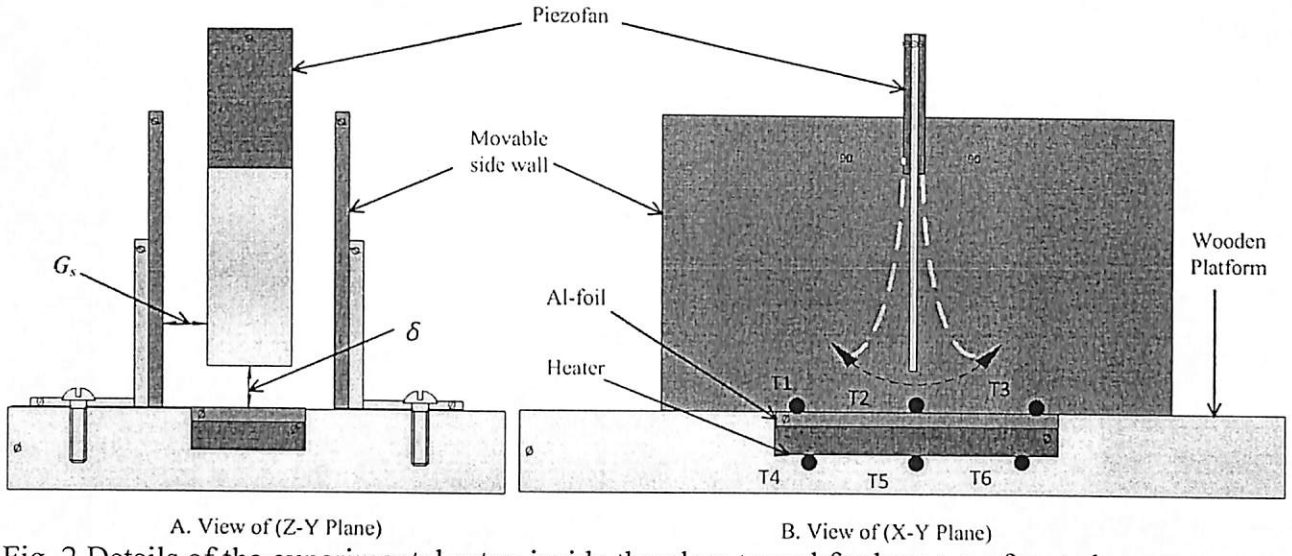

Fig. 2 Details of the experimental setup inside the glass tunnel for heat transfer study.

The piezoelectric fan was oriented vertically between the side walls, over the foil surface and held rigidly by adjustable stand (ON/OFF magnetic base type of MB-15) for height variety purpose. This arrangement was revealed to yield significant heat dissipation [7]. The heater was powered by a direct current (DC) output of a digital power supply to obtain a constant input ($Q°$) of 1.9W. Three thermocouples (K-type, TTK-36-SLE) were attached on the exposed surface of the foil to calculate the average surface temperature and three were mounted beneath the heater; All of these thermocouples were linked to a desktop PC utilizing a data acquisition system (Advantech USB-4718, 8-channel).The temperatures were recorded at every 60 seconds. Transient and steady state temperatures were recorded in natural and forced (with piezoelectric fan switched on) convection conditions. The ambient was always monitored at 25C°. The assembly of the chip, side walls embedded with piezoelectric fan was housed into the glass tunnel to reduce the ambient effects. The average heat transfer coefficient (h_{av}) was defined as:

$$h_{av} = \frac{q}{(T_f - T_a)} \tag{1}$$

The Reynolds number (Re) according to the fan tip deflection (ωA) was computed by:

$$Re = \frac{\omega\, A_t\, D_{pf}}{v} \tag{2}$$

2.3 Computational Modeling

The simulation model was also used to examine the correlation between the flow field induced by the piezoelectric fan and the heat removal from the chip surface. The 3D model used in this simulation consisted of aluminum foil, simple side walls and piezoelectric fan as shown in Fig. 3. The size of heat source was similar to the heater used in the experiment.

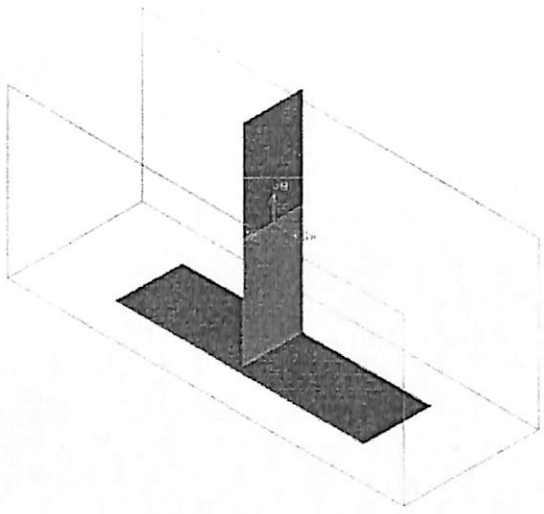

Fig. 3 Positions of piezoelectric fan and side walls

The clamp of the piezoelectric fan was neglected. The fan boundary was modeled as a moving adiabatic wall whose location in time was set by a UDF (user defined function) in FLUENT. The fan was modeled as infinitesimally thin wall with no thermal conduction allowed through it. No-slip boundary conditions were applied to the platform and side walls. Other boundaries were treated as pressure boundaries, permitting the air flow inward or outward. A combination of tetrahedral and quad literal elements (about half million) were used for meshing as shown in Fig.4.

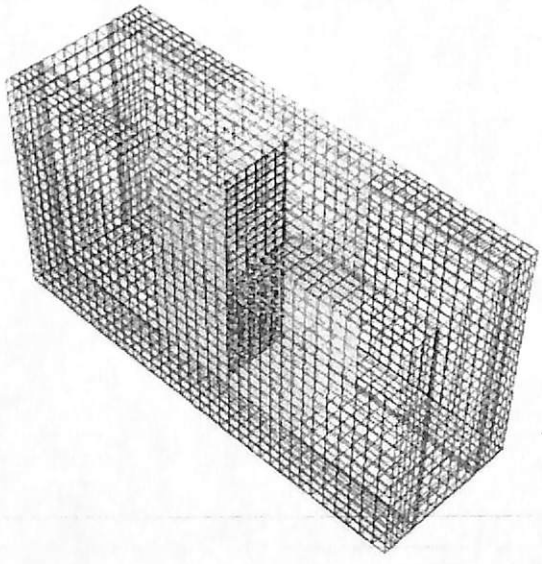

Fig. 4 Meshed models

The fluid domain was divided into two regions namely region 'a' and region 'b as shown in Fig. 5, and the boundary of these two regions is imposed as a fluid interface. The purpose of fluid

interface was to avoid damaged fluid cells since region 'a' of the fluid domain includes the deforming beam (piezoelectric fan). Only single cell spacing was included from the tip of the beam to the fluid interface to avoid stretching which might lead to failure of fluid cells. Region 'b' was distinguished by stationary fluid cells that interacted with region 'a' through the fluid interface. FLUENT offers many options on the dynamic mesh mechanism, but only smoothing and remeshing mechanisms were chosen. Smoothing considers the movement of the fluid zone to be a spring-like deformation while, remeshing is used to remesh the cells if their new volume is smaller than the prescribed value [19].

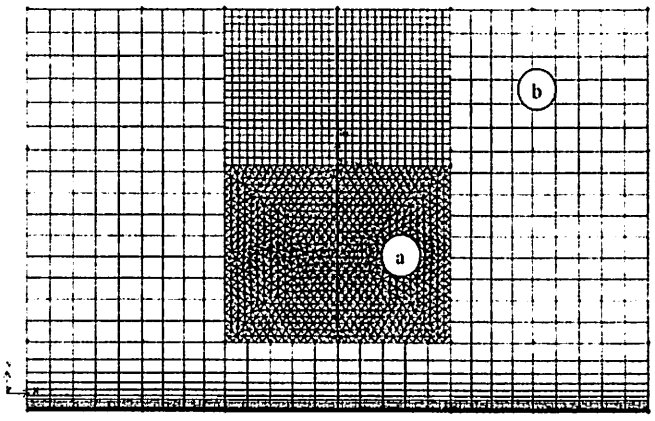

Fig. 5 Mesh generation regions

2.3.1 Mathematical Model

The flow was assumed incompressible and turbulent. The governing equations employed in FLUENT, for describing the transient fluid flow are as follows:

Continuity:

$$\frac{\partial \rho}{\partial t} + \frac{\partial}{\partial x_i}(\rho u_i) = 0 \tag{3}$$

Momentum (non-accelerating reference frame):

$$\frac{\partial}{\partial t}(\rho u_i) + \frac{\partial}{\partial x_j}(\rho u_i u_j) = -\frac{\partial P}{\partial x_j} + \frac{\partial \tau_{ij}}{\partial x_j} + \rho g_i + F_i \tag{4}$$

where; ρ is the fluid density, P is the pressure in the fluid, τ_{ij} is the viscous stress tensor and g_i and F_i are the gravitational acceleration and external body force in the i-direction, respectively.

However, FLUENT allows the user to simulate moving and deforming domains through the use of user define function (UDF). Dynamic meshes can be used to model flow where the shape of the domain is changing with time due to motion of the domain boundaries. The integral form of

the transport equation for a general scalar (Φ), on an arbitrary control volume (V), on a moving mesh is written as:

$$\frac{d}{dt}\int_V \rho\Phi dV + \int_{dV} \rho\Phi(\vec{u}-\vec{u}_g)dA = \int_{dV} \Gamma\nabla\Phi dA + \int_V S_\Phi dV \qquad (5)$$

where $\vec{u}$ is the flow velocity vector and $\vec{u}_g$ is the grid velocity of the moving meshes. The first and second terms on the left are the time derivative and the convective terms. The terms on the right are the diffusive and the source terms. Γ is the diffusion coefficient and S_Φ is the source term of Φ. ∂V represents the boundary of the control volume V and dA is the area movement.

Fluid energy:

$$\frac{\partial}{\partial t}(\rho E) + \frac{\partial}{\partial x_i}\left(u_i(\rho E + P)\right) = \frac{\partial}{\partial x_j}\left(k_{eff}\frac{\partial T}{\partial x_i} - \sum_{j'} h_{j'}J_{j'} + u_j(\tau_{ij})_{eff}\right) + S_h \qquad (6)$$

where k_{eff} is the effective conductivity ($k_f + k_t$, where k_t is the turbulent thermal conductivity, defined according to the turbulence model being used), and $J_{j'}$ is diffusion flux of species. The first three terms on the right-hands side of equation (6) represent energy transfer due to conduction, species diffusion, and viscous dissipation, respectively. S_h includes heat of chemical reaction, and any other volumetric heat sources defined. E is the total energy of moving fluid per unit mass and is defined as:

$$E = e + \frac{u_i^2}{2} = h - \frac{P}{\rho} + \frac{u_i^2}{2} \qquad (7)$$

where e is the fluids internal energy per unit mass and h the sensible enthalpy. For an incompressible fluid the viscous dissipation terms are neglected because the amount of energy produced by the viscous stress will be too small compared to the other sources of energy.

Solid energy:

$$\frac{\partial}{\partial t}(\rho h) + \frac{\partial}{\partial x_i}(\rho u_i) = \frac{\partial}{\partial x_i}\left(k_s\frac{\partial T}{\partial x_i}\right) + \dot{q}''' \qquad (8)$$

where $\dot{q}'''$ is the volumetric heat source. The second term on the left-hand side of equation (8) represents convective energy transfer due to rotational or translational motion of the solids; in this study, it is always set to zero since the solid boundaries are motionless. The first term on the right-hand side is the heat flux due to conduction.

2.3.2 Simulation Modeling

The first-order upwind discretization scheme was used both for momentum and energy equations, with the SIMPLE scheme for pressure-velocity coupling. For the treatment of the turbulent flow at the near-wall region (heat source surface), the y^+ value was set as 1. The shear stress transport (SST) k-ω model was used to describe the flow induced by the piezofan, which has local turbulence.The beam was assumed to vibrate at a frequency of 100Hz; this round off

(compared to the experimental value of 112Hz) was made for achieving numerical stability. Time-step size of 0.0001s was chosen for all the cases, with 100 time steps per cycle of fan vibration. This value was arrived at after three attempts to check the trend and proximity with the profiles investigated; for instance, the trials were done by increasing the mesh elements and decreasing the time steps. However, a problem arose when the mesh elements were increased, due to the negative volume or less memory detected in FLUENT during analysis. This problem is typically found in dynamic meshing setup. The total duration of the simulation is selected such that the temperature reaches a steady value during this period. It took 5,000 iterations, which corresponds to approximately three days of computation time per each case on a Pentium DualCore processor (each 2.8 GHz) computer with 2.0 GB of memory.

2.4 Results and Discussion

A. Experimental Results

2.4.1 Effect of δ and G_s on Re

The experimental measurements of *Re* are computed according to the fan amplitude [13]. The *Re* is plotted against the ratio of G_s to the fan width D_{pf} for each δ value, as shown in Fig. 6.Gradually increasing of *Re* is observed with increase of side gap until about (G_s/D_{pf} = 1.2) and then remains steady, which indicates that G_s has no further influence on *Re*. It is seen that the minimum Reynolds number is 2242 at (G_s/D_{pf} = 0.2) and (δ = 0.0285). As G_s decreases, the side walls cause damping on the vibrating piezoelectric fan, thereby reducing *Re*. However, it is worth noting that, at smaller tip gaps, despite the decrease of *Re*, we observed higher heat transfer coefficients; this is due to the proximity of peak velocity zone with the surface of heat source as will be elucidated in the next section.

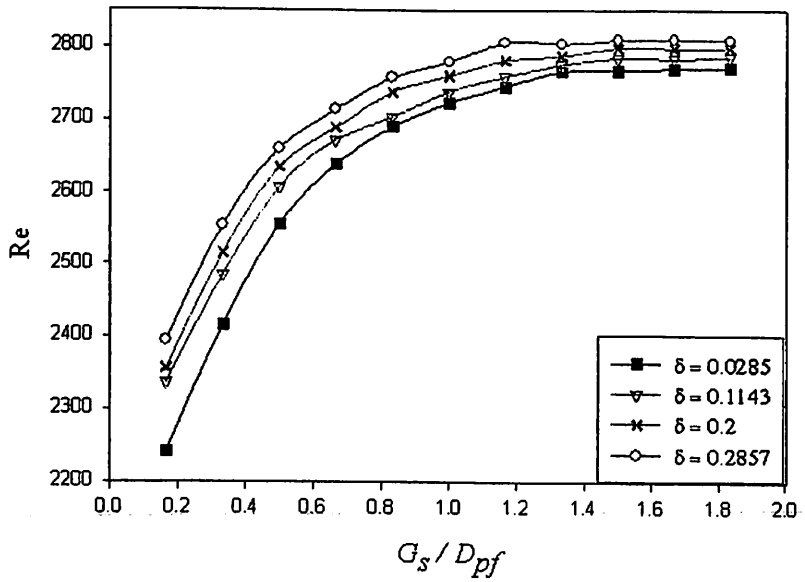

Fig. 6. Coupled effect of tip and side gaps on *Re*.

2.4.2 Heat transfer coefficient

The temperature histories under natural and forced convection modes are shown in Fig. 7. At t = 0 the heater was switched on in natural convection, and the steady state was achieved at t = 3600s; the piezofan was switched on at t = 3600s and the temperatures were recorded until fresh steady state was reached. It is evident that the piezoelectric fan caused drastic reduction in source temperature with more than (60%), due to the enhanced heat removal.

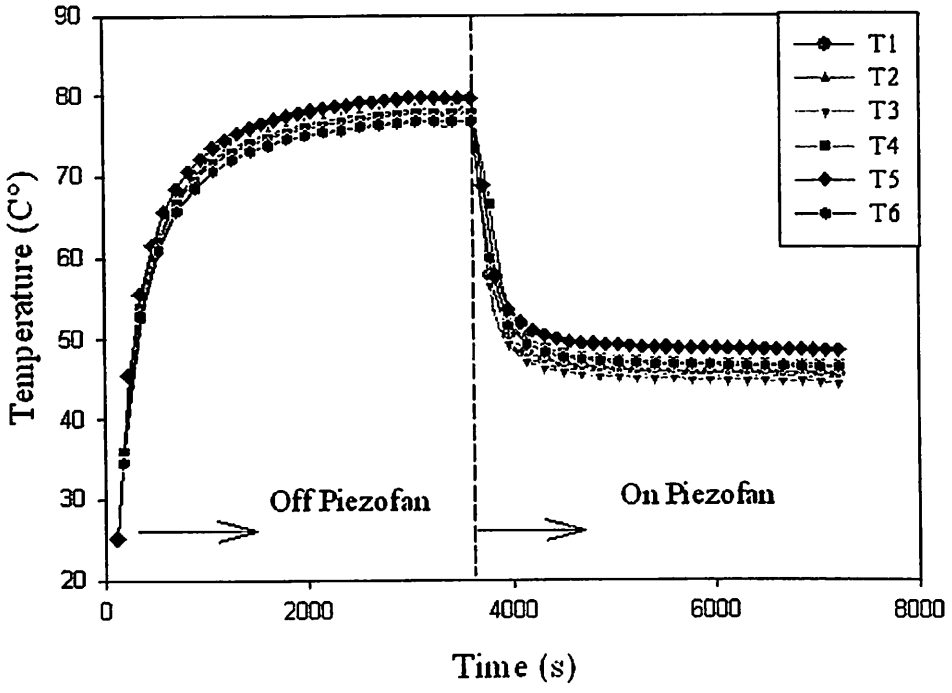

Fig. 7 Temperature histories in natural and forced convection conditions. C°

The average heat transfer coefficient h_{av} (force convection) in a representative experiment is shown in Fig. 8 according to the coupled effect of δ and G_s.In general lower δ enhances the h_{av} while lower G_s reduces h_{av}. The increase of G_s/D_{pf} from 0.2 to 1.2 increases h_{av}, and then remains steady. This indicates that for the minimum δ of 0.0285, there is a suitable G_s which provides maximum heat removal. However, δ is revealed to be more significant on h_{av} compared to G_s. It is also observed that h_{av} is decreased with the decrease of G_s/D_{pf} for each value of δ. At lower G_s, the piezoelectric fan amplitude decreases due to the viscous drag of the flow, thereby reducing the cooling capacity [9]. Based on the heat transfer performance, the optimum δ and G_s/D_{pf} in the present study were obtained to be as 0.0285 and 1.2 respectively.

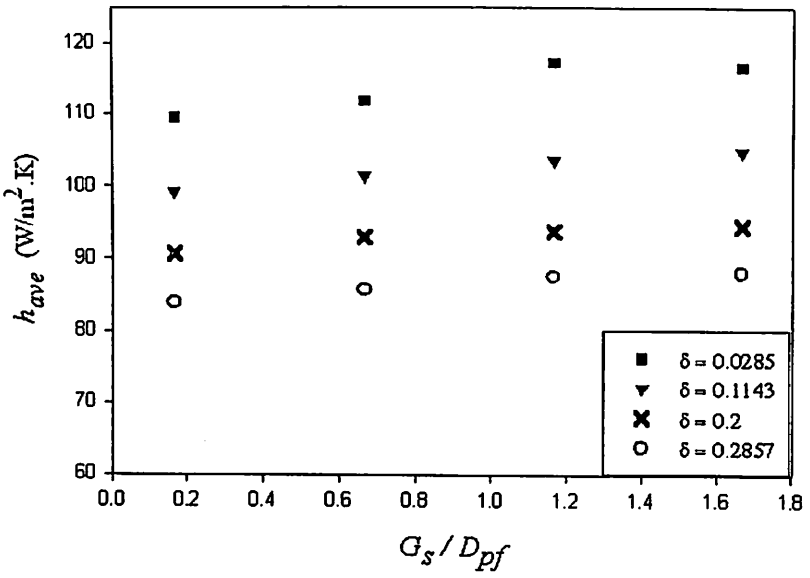

Fig. 8 Coupled effect of tip and side gaps on h_{ave}

B. Simulation results

From the heat transfer map which was presented experimentally in previous section, only two configurations were chosen to be simulated. These configurations namely (best case) and (worst case) were based on the higher and lower rate of heat transfer respectively (see Fig. 8), and that could engender confidence in the numerical solutions.

2.4.3 Temperature contours

The temperature contours of the force convection, for the best case and worst case configurations are shown in Fig. 9 and 10 respectively. Unlike the worst case, for the best case, it is observed that the fan could be able to agitate the thermal boundary of the heat source due to the small tip gap (δ). Therefore, the thermal boundary which is generated on the top of the heat source (chip) seems to be shuttered into two symmetrical regions on the left and right sides of the fan due to the fluid displacement, while the center zone shows significant drop in temperature gradient; this phenomenon could maximize the heat dissipation over the heater surface. This observation is expected to be reasonable according to the velocity profiles as will be elucidated in section VI.

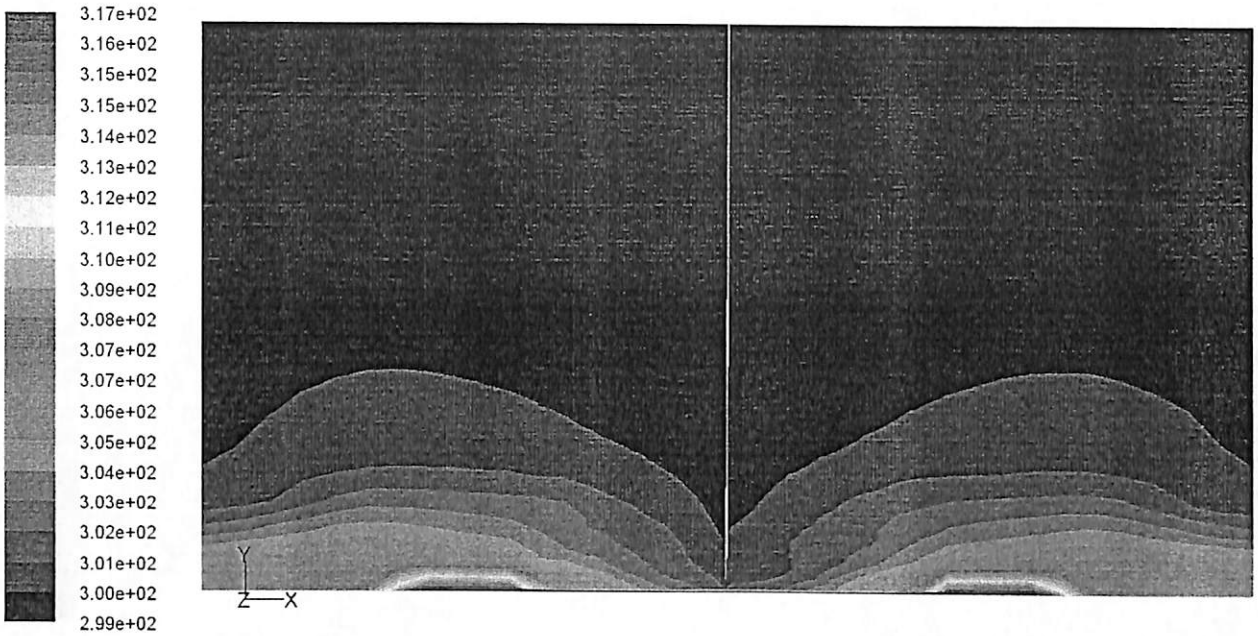

Fig. 9. Temperature contours (K) and labels for best case at $t = 0.5$s.

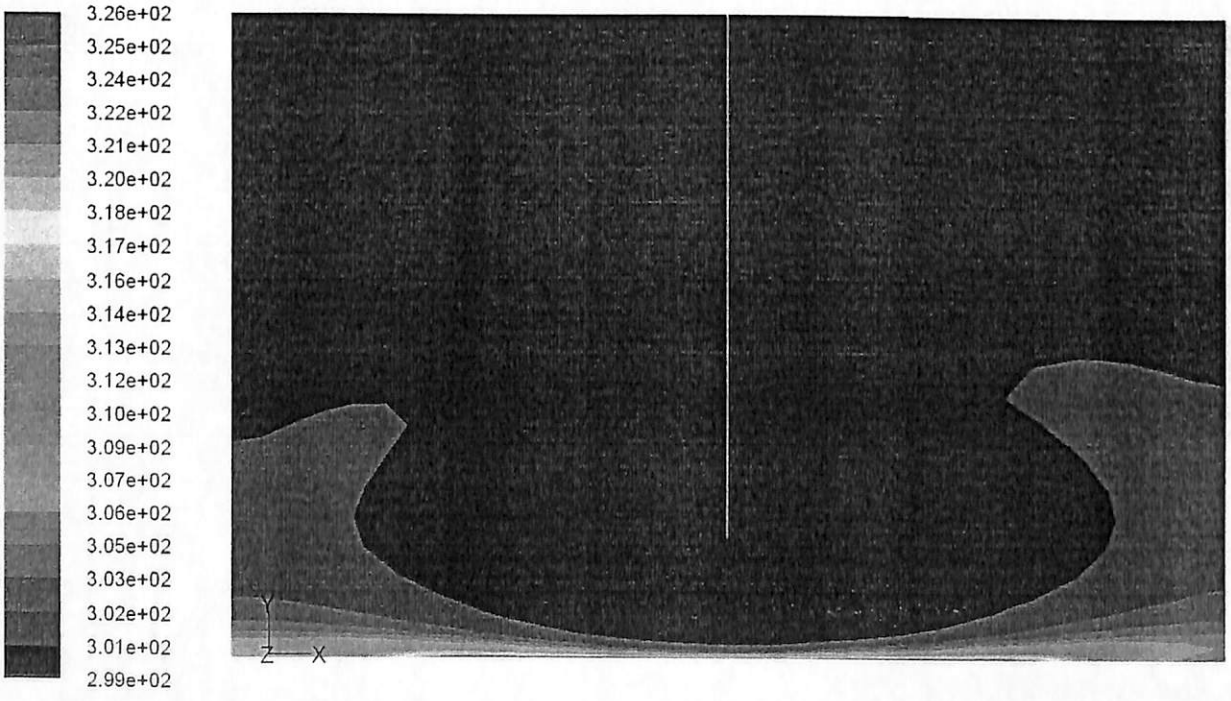

Fig. 10 Temperature contours (K) and labels for worst case at $t = 0.5$s.

Fig. 11 and 12 show the corresponding temperature contours on the foil, at $t = 0.5$s. For the best case, a droplet cooling zone is observed at the centre of the heated foil and this droplet appears to be symmetric in the direction of piezoelectric fan vibration. The droplet zones widen

laterally due to the induced swirling flow on both sides of the fan. However, for the other case, the temperature drop is lower than that of the best one due to the large tip gap with small side gap. The effects of side gap on the side edge of the foil are quite obvious, as evidenced by the hotter zones compared to the centre; this indicates that the flow at the side edges of foil was decelerated due to the small side gap (G_s=1mm) and the flow was accelerated along the center line. Both profiles agree that this droplet cooling zone is prominent at the central foil; this is attributed to the enhanced cooling of the central foil due to the presence of piezoelectric fan on both sides.

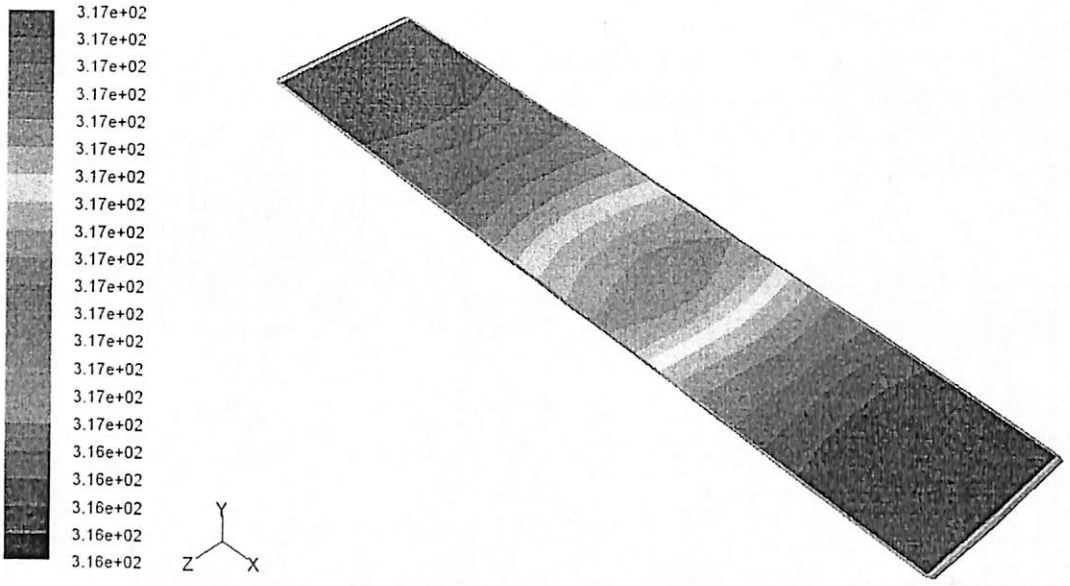

Fig. 11. Temperature contours (K) of the foil for the best case at t = 0.5s.

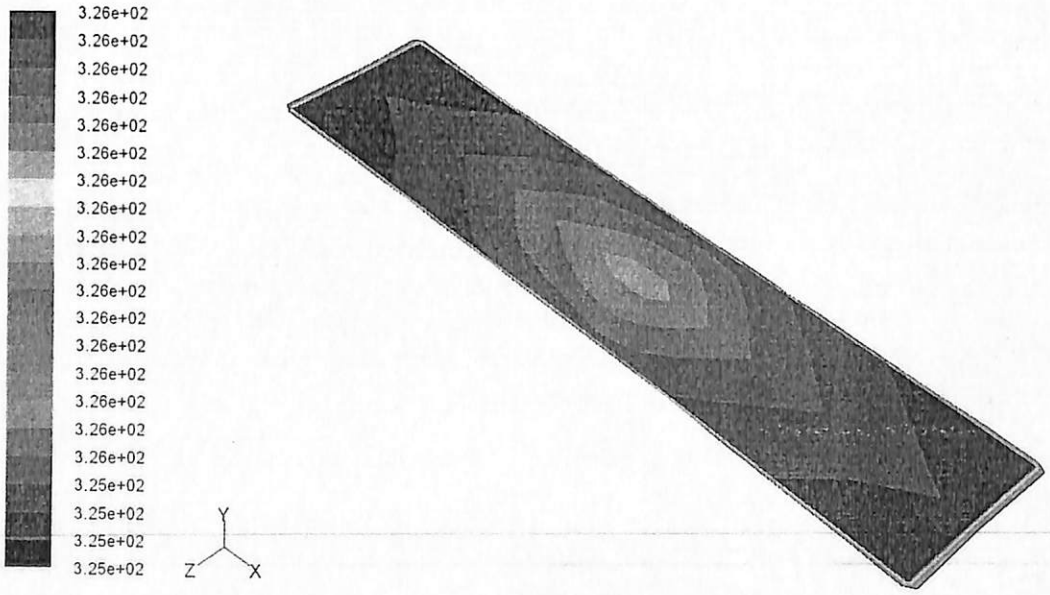

Fig. 12 Temperature contours (K) of the foil for the worst case at $t = 0.5$s.

C. Model validation

2.4.4 Heat transfer coefficient

Fig. 13 shows the predicted convection heat transfer coefficient along the horizontal centerline of the foil surface. In each case, the heat transfer coefficient decreases as it moves to the foil's center which is opposite to the fan amplitude zone. It is observed that the best case has dramatic increase in heat transfer coefficient compared to the worst case which indicates that δ and G_s have significant role on the heat removal performance.

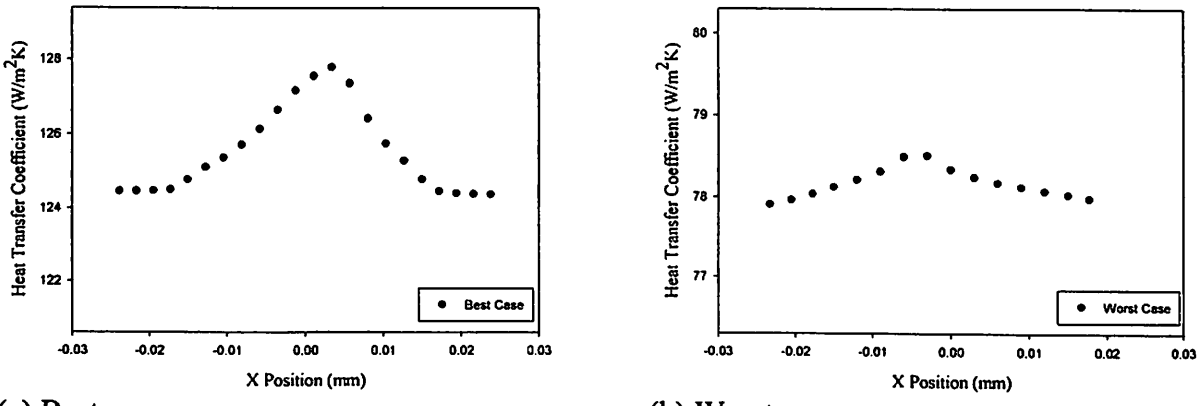

(a) Best case (b) Worst case

Fig. 13. Heat transfer coefficient plots on the reference line for the comparison of the cases

Figure 14 shows the measured and computed heat transfer coefficients for the best and worst cases at the heat source. It might be said that the general agreement is good. A maximum of 7% under-prediction is observed in the simulation, which is attributed to the omission of radiation effect in the numerical model and the slightly different of the beam frequency; this presumption was verified by deducting the experimentally determined radiative contribution from the predicted value.

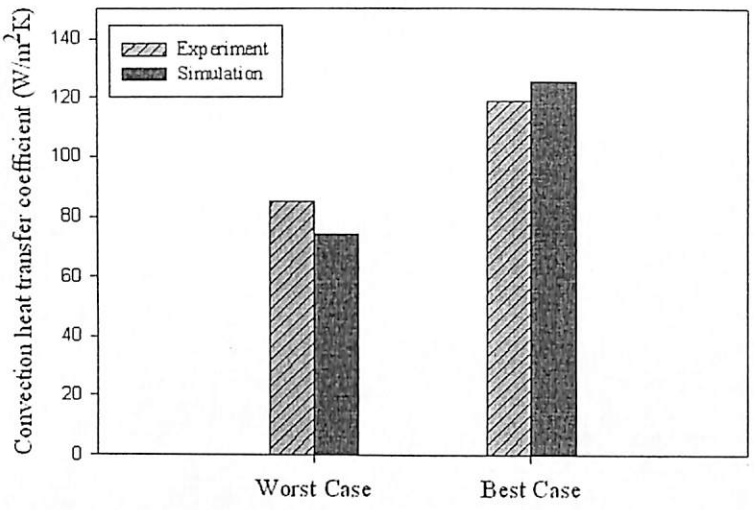

Fig. 14 Comparison of predicted and experimental heat transfer coefficients.

In addition, the thickness of the thermal compound in the simulation was treated as uniform in all the cases; the real thickness was not necessarily so, as the compound was manually applied. Furthermore, the ambient temperature in the experiments was measured with a single thermocouple, whereas the average fluid temperature inside the domain was used in the simulation.

2.4.5 Flow field

Apparently, the flow field induced by the vibrating fan is naturally unsteady, and the flow mechanisms are quite complex. For such a complex flow, the numerical solution has offered a practical approach for an accurate analysis which presented the flow profile with the boundary layers. In order to substantiate the prediction results, the flow field at the best and worst cases were also studied by using PIV system and validated against the numerical solution. Figure 15 shows the comparison of the captured flow field and velocity vectors from the PIV system, and the numerical result, for the best case at the approximate natural position of the piezoelectric fan. Counterclockwise and clockwise vortices are seen at the right and left sides respectively while vortices at the side are propagated due to the flow impingement (two vortex locations are encircled). As the tip gap is minimum, the piezoelectric fan vibration causes the air to be squeezed out in both directions and forcing the fluid to displace more rapidly. Thus the high velocity zone is mostly localized in the vicinity of the heater surface, enabling effective heat removal. The vortex zones at the best case are in direct contact with heater surface, which facilitates enhanced heat removal.

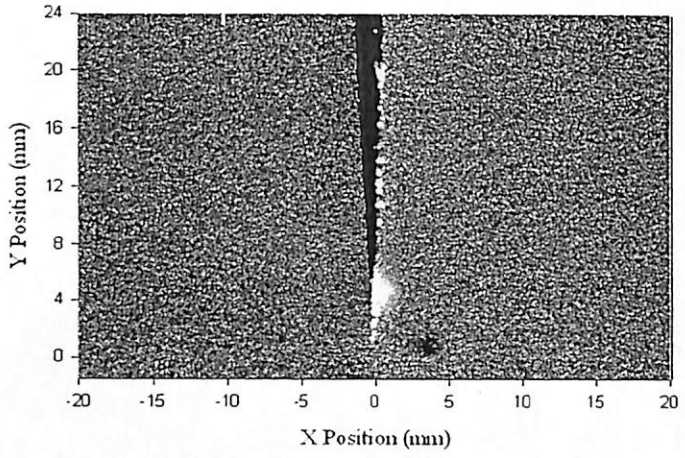

(a)

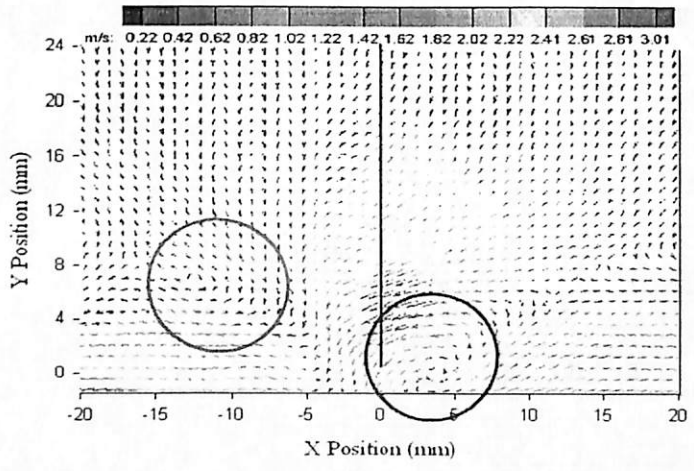

(b)

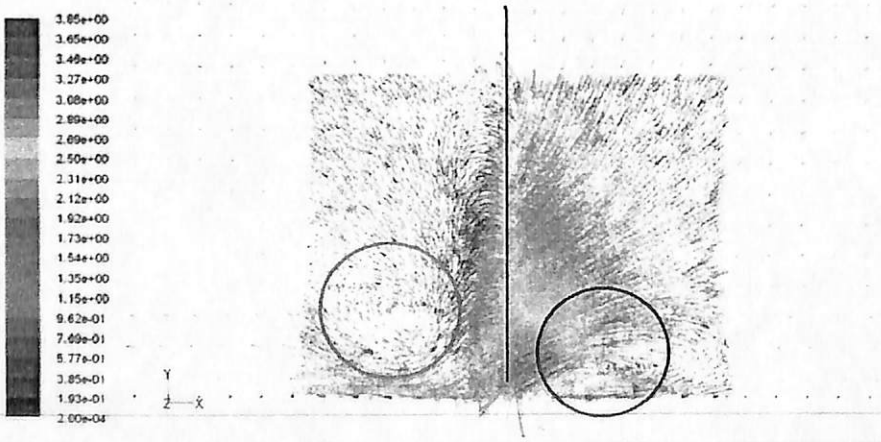

(c)

Fig. 15 Comparison of experimental and numerical flow fields for the optimum case.

Fig. 16 shows the comparison of PIV and numerical flow fields for the worst case. As the tip gap is maximal the fluid agitation near the hot surface is minimal. Moreover, as the high velocity zone is situated at the near-tip region which is relatively far from the heat source, it is not effectively exploited for cooling. It is also observed that the vortex zones on both sides of the fan (shown encircled) are larger and farther from the heat source, compared to the best case; this prompts the fluid to lose much momentum as it reaches the hot surface resulting in decreased heat transfer rates. In general, it is observed that the predicted velocity magnitudes as well as the flow pattern are in good agreement with the PIV results, and the thermal behaviors of the optimum and worst cases have been verified.

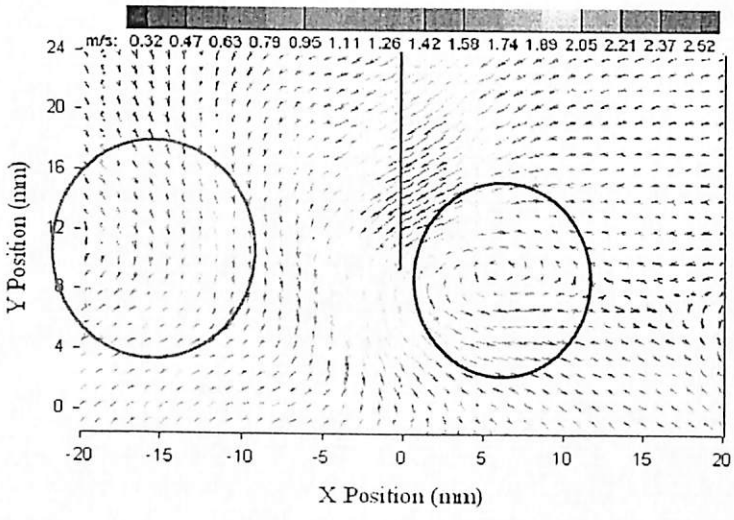

(a)

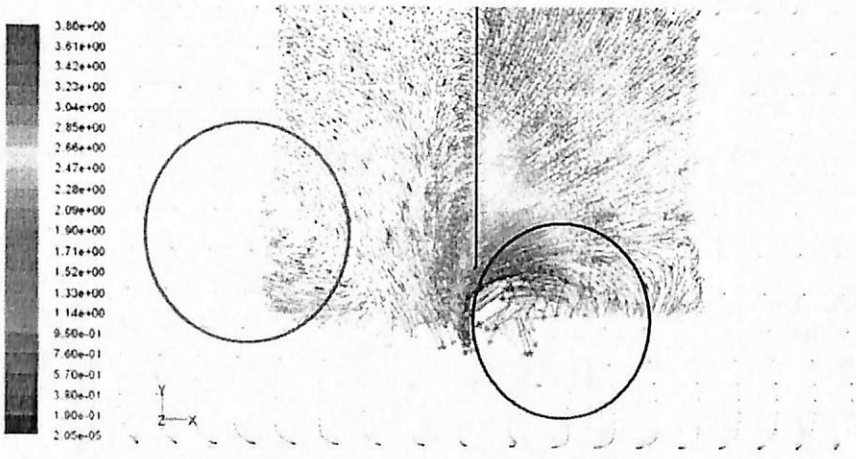

(b)

Fig. 16. The worst case flow field of (a) PIV velocity vectors, and (b) Numerical velocity vectors.

4.7 Combination of heat sink and piezoelectric fans for LED cooling

The previous section introduced the piezoelectric fan for horizontal hot surface. It was determined that, the LED junction temperature can be maintained at low temperature with the use of dual piezoelectric fans. Besides, various configurations of piezoelectric fan arrangement were explored for LED cooling. In this section, the combination of heat sink with piezoelectric fans to cool the LED package for maximizing the heat dissipation is carried out. The main goal of this work is to arrive at a profitable combination of heat sinks and piezoelectric fan to maintain desirable temperature of the LEDs.

4.7.1 Dual vibrating fans

Heat sink is well known in enhancing convection and is used extensively for enhancing heat dissipation. Its efficiency is further increased when subjected to forced convection. A sample experiment of the transient temperature history under natural and forced convection modes for various thermocouples locations on the heat sink is shown in Figure 17. At t = 0s the LED is switched ON subjected to natural convection (the set up of dual vibrating fans remained off). The temperature of heat sink began to rise as a result of the heat generated by LEDs. When the heat generated equals heat dissipated, the temperatures stabilize which indicates that the system has approximately reached steady sate. When the temperatures show no variation over a period of an hour (t = 3600s), it is assumed that steady-state has indeed been achieved. Subsequently, the dual fans are switched on at t = 3600s and a new steady state is achieved after approximately t = 7200s. It was observed from this experiment that the overall heat sink temperature was about 335 K when subjected to the natural convection mode. This was considerably lower than that determined without heat sink operating under natural convection as explained earlier in Figure4.32. When the dual fans are operated, the temperature further observes a sharp decline to about 315K. This clearly shows that, the combination of heat sink and dual fans contribute towards a significant fall in the temperature of heat sink. It is worth noting that the maximum temperatures in the figure are corresponding to the measurement of the solder point over the MCPCB, and not the junction temperature. The junction temperatures are then calculated according to the equation (Rjs= (Tj – Ts)/Q)

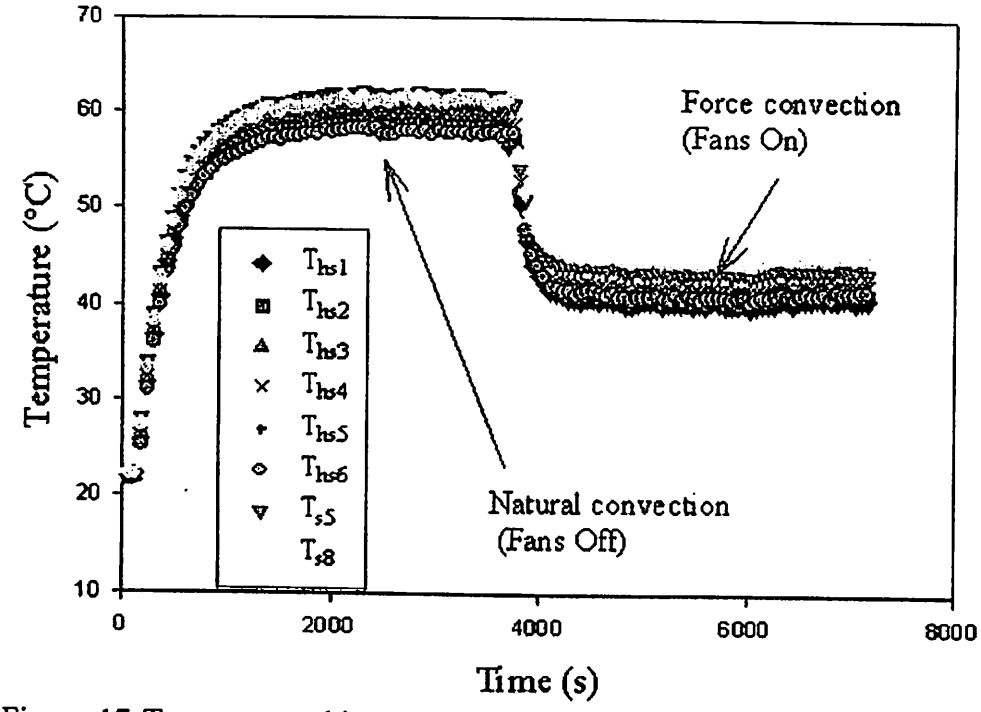

Figure 17 Temperature history of natural and forced convection conditions for heat sink-LED cooled by dual vibrating fans.

Thus, addition of heat sink to the LED package has significant impact in reducing the overall temperature when compared to MCPCB without heat sink. The overall temperature of the MCPCB with and without heat sink for the natural convection is shown in Figure 4.37. A decrease of about 43.5 % is detected with addition of only the heat sink to LED package under natural convection mode. This is further reduced when the dual vibrating fans are activated and the decrease in temperature is about 34% relative to the natural convection and about 42% with respect to only MCPCB without heat sink as shown in Figure 4.38.

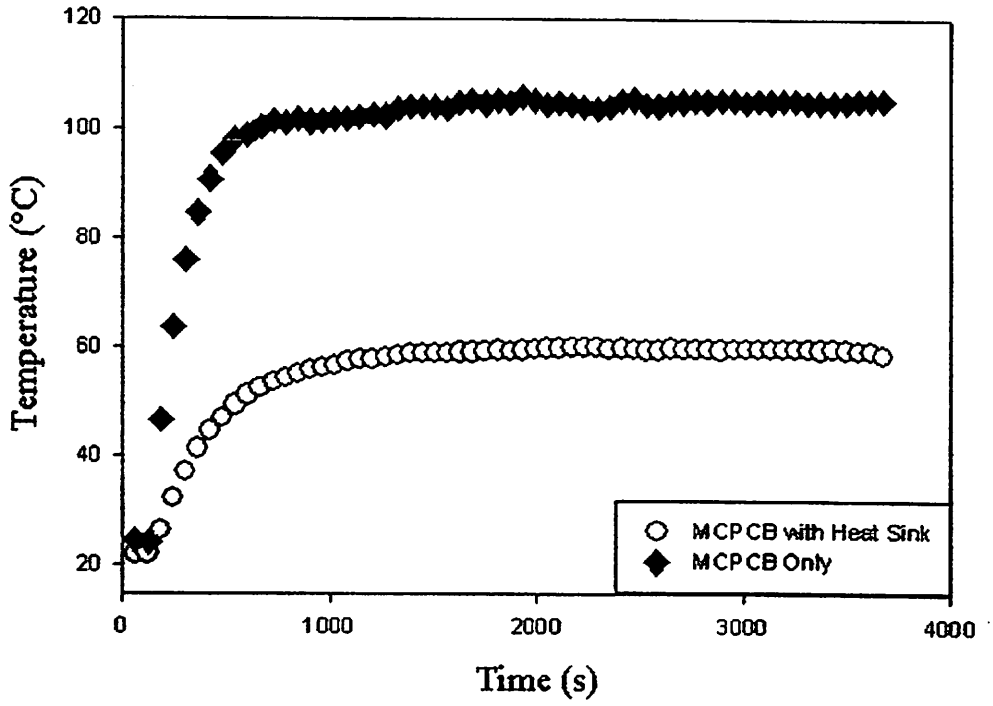

Figure 4.37 Temperature history of the LED package, MCPCB with and without heat sink subjected to natural convection.

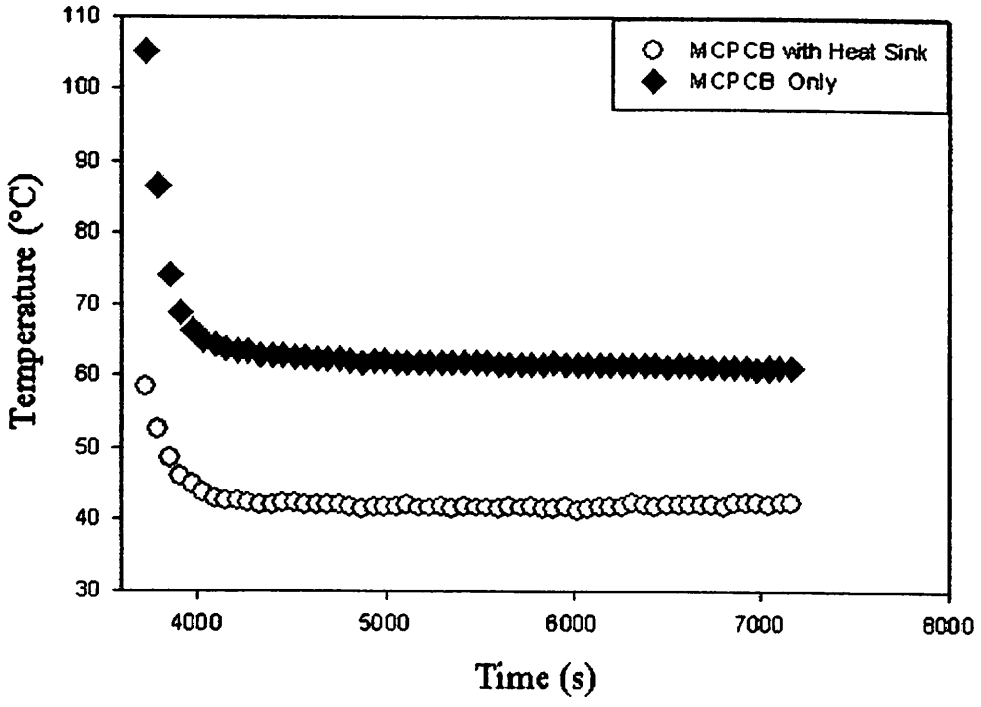

Figure 4.38 Temperature reduction history of LED package by dual vibrating fans for MCPCB with and without heat sink.

Figure 4.39 illustrates the temperature contours of assembly heat sink-LEDs during natural convection condition. The multi-chip LED package acts similar to the multi heat sources. The highest temperature magnitude observed at the junction was almost identical at every individual chip. Besides, there is gradual flow of heat from the chips to the fins exposed to the ambient atmosphere. On the contrary, a thicker thermal boundary layer formed with only the natural convection condition accumulating over the heated surfaces. This is because of the lower convection rate and can be attributed to smaller surface area available for heat dissipation. The highest temperature was 338K and the lowest was fixed to be 308 K in order to facilitate qualitative comparison with next cases of force convections.

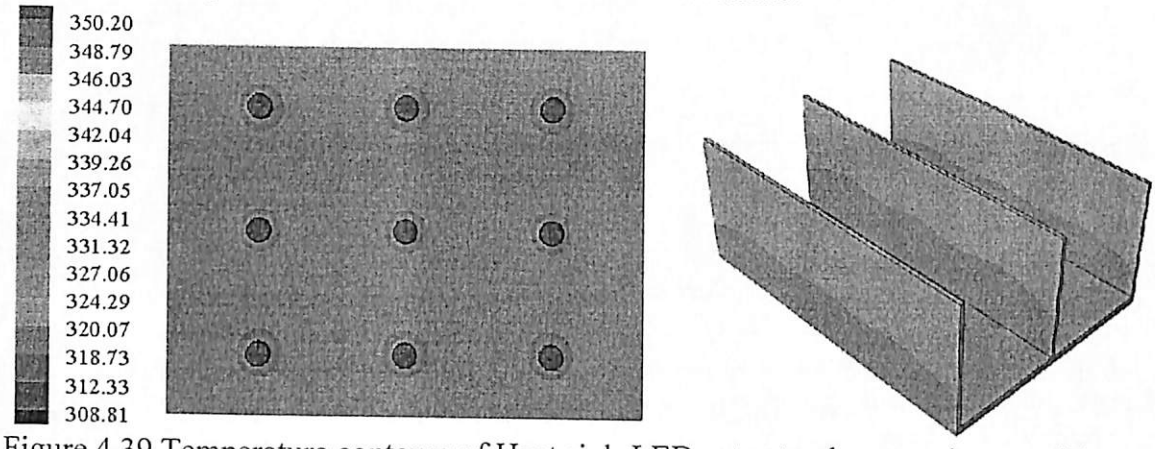

Figure 4.39 Temperature contours of Heat sink-LEDs at natural convection condition.

Figure 4.40 illustrates the local temperature distribution for the assembly heat sink-LED cooled by dual vibrating fans. The vibration envelope is overlaid on each slot of heat sinks' base and the solid line in the center represents the fan at its zero natural position with the remaining lines illustrating the extent of the vibration envelope, whose overall dimensions were twice the vibration amplitude. As the two fans vibrate, a droplet cooling zone is formed at the base as a lobed pattern and is observed at the middle of each slot of the heat sink surface (heat sink base). These lobes, which appear symmetric in the X and Z directions, indicate that the flow induced by the fan is also evenly separated; the flow could only be obtained with vertical fan orientation. Besides, droplet cooling zone is also formed as a lobe and is observed at the middle of each fin on the heat sinks. These droplet zones, which transition to a nearly diamond pattern symmetric in X direction, indicate that the flow induced by the fans' side edges is also interacting with sides wall (fins). The hot spots on the heat sink base are small circular patterns representing the contacting elements of LEDs slug with heat sink. These hot spots are the source of heat and in this case has faded at the center of heat sink (X=0) due to the large convection, which is attributed to presence of the fans. Nine of these slugs are representing nine heat sources spreading heat from their top to the bottoms to the MCPCB and ultimately to the heat sink.

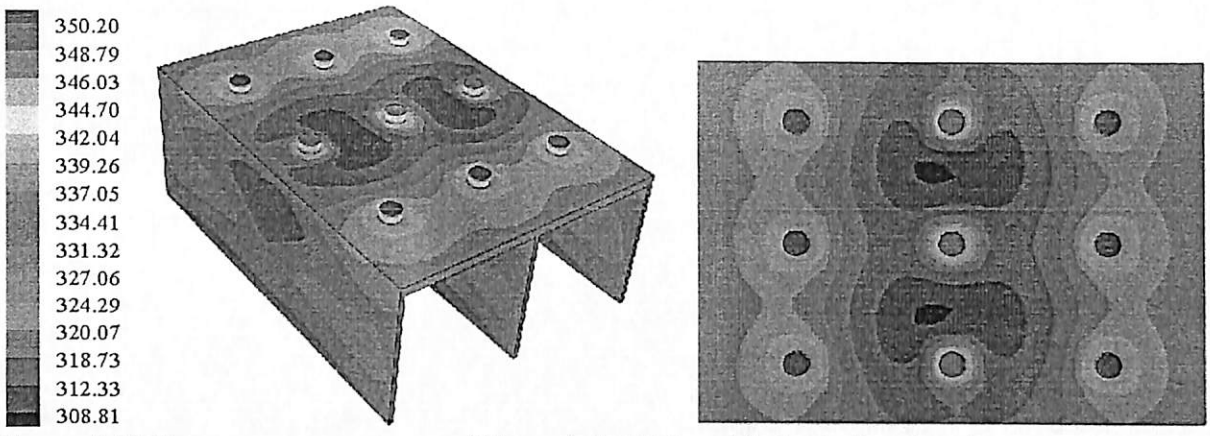

Figure 4.40 Temperature contours of Heat sink-LEDs with dual vibrating fans.

Figure 4.41 shows the cross section of single LED panel and its temperature distribution. The contours show the complex heat flow pattern in the LED slug on account of combined convection and conduction. Very high temperature gradient can be seen at top surface of the slug where the junction temperature is estimated. The high thermal conductivity of aluminum accelerates conjugate heat transfer via conduction by facilitating faster heat dissipation from the LED chips and then to heat sink to be dissipated to the surrounding atmosphere.

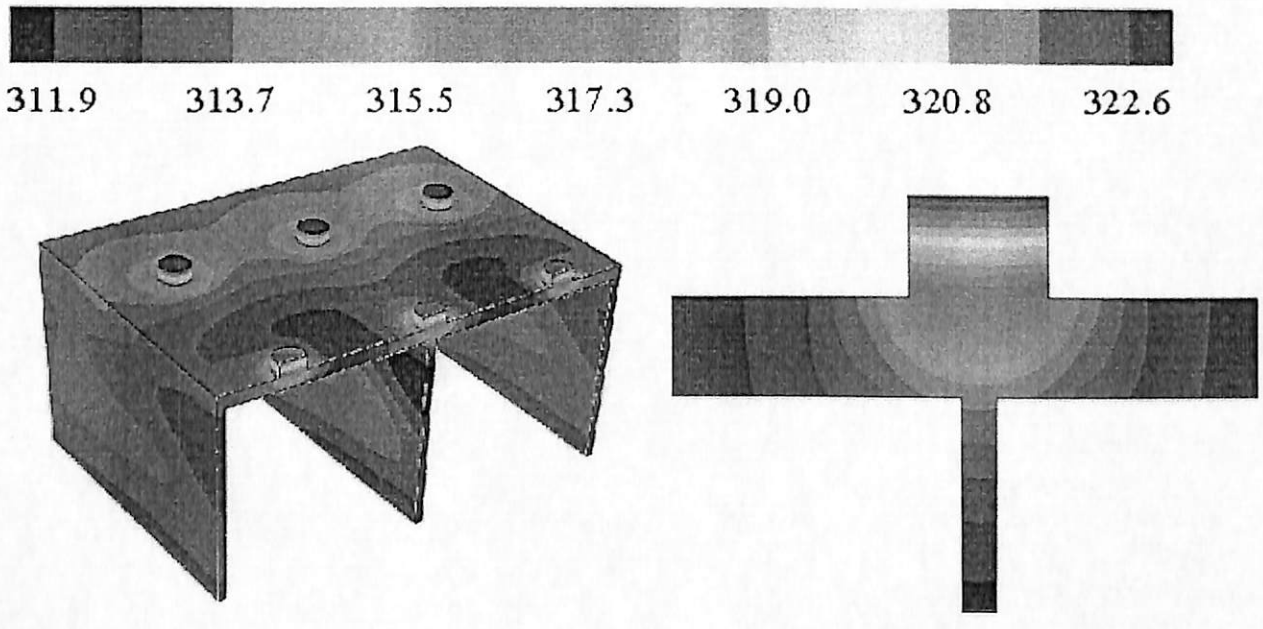

Figure 4.41 Temperature contours of single LED cross section.

5.0 Conclusion

The aim of this project was to establish a sensitive CFD method to simulate the interaction between flow and vibrating piezoelectric fan, and to use this method to investigate the

performance of a single and multiple vibrating fans. The following conclusions were drawn from the investigations:

1. Vertical orientation with minimal tip gap of the fan was proved the best cooling performance.
2. The largest amplitudes were detected at in-phase vibration $\Phi = 0°$ due to reduction in viscous drag and which could further increase vibration amplitudes; whereas the smallest amplitudes were detected at out-of-phase vibration $\Phi = 180°$.
3. No guarantee for in-phase (or out-of-phase) vibration to remain under in-phase or out-of-phase vibration condition over extended duration.
4. The single fan enhances heat transfer performance within approximately 2.3 times for the heated surface. By contrast, the dual fans enhance heat transfer performance within approximately 2.9 for out-of-phase vibration ($\Phi=180°$) and 3.1 for in-phase vibration ($\Phi=0°$).
5. Thermal characterizations of the assembly heat sink-LEDs cooled by dual and quadruple vibrating fans have been experimentally investigated.
6. 3D coupling based on a dynamic meshing scheme was conducted with FSI.

REFERENCES

1. Toda, M., *Theory of air flow generation by a resonant type PVF2 bimorph cantilever vibrator* Ferroelectrics, 1979. **22**: p. 911-918.
2. Toda, M., *Voltage-induced large amplitude bending device PVF2 bimorph its properties and applications.* Ferroelectrics, 1981. **32**: p. 127-133.
3. Schmidt, R.R., *Local and average transfer coefficients on a vertical surface due to convection from a piezoelectric fan.* Paper presented at the InterSociety Conference on Thermal Phenomena, 1994.
4. Ihara, A. and H. Watanabe, *On the flow around flexible plates, oscillating with large amplitude, Journal of Fluids and Structures* 1994. **8**: p. 601-619.
5. Po, P.I. and L. Byoung-Gook, *Feasibility of using ultrasonic flexural waves as a cooling mechanism.* Industrial Electronics, IEEE Transactions on, 2001. **48**(1): p. 143-150.
6. Acikalin, T., A. Raman, and S.V. Garimella, *Two-dimensional streaming flows induced by resonating, thin beams.* The Journal of the Acoustical Society of America, 2003. **114**(4): p. 1785-1795.
7. Kimber, M., S.V. Garimella, and A. Raman, *Local Heat Transfer Coefficients Induced by Piezoelectrically Actuated Vibrating Cantilevers.* Journal of Heat Transfer, 2007. **129**(9): p. 1168-1176.
8. Kimber, M. and S.V. Garimella, *Local Heat Transfer Coefficients Under Flows Induced by Vibrating Cantilevers.* Journal of Heat Transfer, 2007. **129**(8): p. 933-933.
9. Açıkalın, T., et al., *Characterization and optimization of the thermal performance of miniature piezoelectric fans.* International Journal of Heat and Fluid Flow, 2007. **28**(4): p. 806-820.
10. Abdullah, M.K., et al., *Numerical and experimental investigations on effect of fan height on the performance of piezoelectric fan in microelectronic cooling.* International Communications in Heat and Mass Transfer, 2009. **36**(1): p. 51-58.

11. Florio, L.A. and A. Harnoy, *Use of a vibrating plate to enhance natural convection cooling of a discrete heat source in a vertical channel.* Applied Thermal Engineering, 2007. **27**(13): p. 2276-2293.
12. Liu, S.-F., et al., *Heat transfer by a piezoelectric fan on a flat surface subject to the influence of horizontal/vertical arrangement.* International Journal of Heat and Mass Transfer, 2009. **52**(11–12): p. 2565-2570.
13. Kimber, M., et al., *Pressure and Flow Rate Performance of Piezoelectric Fans.* Components and Packaging Technologies, IEEE Transactions on, 2009. **32**(4): p. 766-775.
14. AÇIkalin, T., et al., *Experimental Investigation of the Thermal Performance of Piezoelectric Fans.* Heat Transfer Engineering, 2004. **25**(1): p. 4-14.
15. Petroski, J., M. Arik, and M. Gursoy, *Optimization of Piezoelectric Oscillating Fan-Cooled Heat Sinks for Electronics Cooling.* Components and Packaging Technologies, IEEE Transactions on, 2010. **33**(1): p. 25-31.
16. Lin, C.-N., *Analysis of three-dimensional heat and fluid flow induced by piezoelectric fan.* International Journal of Heat and Mass Transfer, 2012. **55**(11–12): p. 3043-3053.
17. Abdullah, M.K., et al., *Optimum tip gap and orientation of multi-piezofan for heat transfer enhancement of finned heat sink in microelectronic cooling.* International Journal of Heat and Mass Transfer, (0).
18. Melling, A., *Tracer particles and seeding for particle image velocimetry.* Meas. Sci. Technol, 1997. **8**: p. 1406-1416.
19. *Modeling Flows Using Sliding and Deforming Meshes FLUENT 6.3.26,*. FLUENT Inc. Lebanon, New Hampshire, , 2006. **Chapter 11.3.**

List of publications from the project:

No.	Latest Status of Publication (Published/accepted/under review/under preparation)	Authors	Title of Article/Journal/Book (complete with year, volume, pages, etc.)
1.	Published	S.F. Shaker, M.Z. Abdullah, M.K. Abdullah, J.J. Mohamed	Effect of side and tip gaps of a piezoelectric fan on microelectronic cooling, IEEE Trans. CPMT, 3(9), 2013, 1545-1553
2.	Published	S.F. Shaker, M.Z. Abdullah, J.J. Mohamed	Effect of synchronized piezoelectric fans on microelectronic cooling performance, Int. Comm. In Heat and Mass Transfer, 43, 2013, 81-89
3.	Published	Z. M. Fairuz, S.F. Shaker, M.Z. Abdullah, M. Zubair, M. S. Abdul Aziz	Effect of synchronized piezoelectric fan mode shape on the heat transfer characteristics, Int. Comm. In Heat and Mass Transfer, 52, 2014, 140-151
4.	Published	S.F. Sufian, Z. M. Fairuz, M. Zubair, M.Z. Abdullah, J.J. Mohamed	Thermal analysis of dual piezoelectric fans for cooling multi-LED package, Microelectronic Reliability, 54, 2014, 1534-1543

List of postgraduate students from the project:

1. Sufian Farid Shaker (Graduated 2014)- PhD student
2. Mohd Fairuz Zakariya (Graduated 2013)- MSc student

Effect of Side and Tip Gaps of a Piezoelectric Fan on Microelectronic Cooling

Shaker Farid Sufian, Mohd Zulkifly Abdullah, Muhammad Khalil Abdullah, and Julie Juliewatty Mohamed

Abstract—**A combination of experimental and numerical analyses is conducted to investigate the coupled effect of side gap (G_S) and tip gap (δ) on the performance of a piezoelectric fan in microelectronic cooling. Two parallel adjustable walls are set at the fan sides to facilitate the variation of G_S. The piezoelectric fan is oriented vertically to the heat source (chip). A 3-D simulation using FLUENT 6.3.2 is performed to assess the transient flow and the resulting heat transfer from the chip. The coupled effect of G_S and δ on the fan tip deflection is detected by a laser displacement sensor (KEYENCE LK-G152). Both G_S and δ had noticeable effects on the flow behavior and *Re*. The effect of δ is more significant on the heat-transfer coefficient than that of G_S. The flow profiles and the temperature contours are found to be consistent with each other, and the predictions are in good agreement with the experimental results. The piezoelectric fan enhances the heat-transfer coefficient 1.95 to 2.7 times, corresponding to the best and worst cases, respectively.**

Index Terms—**Enter electronic cooling, fluent, heat-transfer coefficient, piezoelectric fan, side gap, tip gap.**

NOMENCLATURE

A_{pf}	Amplitude of piezofan (mm).
A_{mc}	Exposed surface area of the foil (m^2).
c_p	Specific heat of air (J kg^{-1} K^{-1}).
D_{pf}	Width of piezofan (mm).
F	External body force (N).
G_s	Side gap (mm).
g	Gravitational acceleration (m s^{-2}).
$\overline{h}_n$	Average natural convection (Wm^{-2} K^{-1}).
$\overline{h}_{pf}$	Average force convection (Wm^{-2} K^{-1}).
k	Thermal conductivity (W m^{-1} K^{-1}).
l_{pf}	Length of piezofan (mm).
l_u	Length of un-patch piezofan (mm).
P	Static pressure (N m^{-2}).
Q°	Power input to the heat source (W).
q°	Heat flux (W m^{-2}).
T	Temperature (K).
T_a	Ambient temperature (K).
$\overline{T}_s$	Average surface temperature (K).
t	Time (s).
t_{pf}	Piezofan thickness (mm).
u	Velocity (m s^{-1}).
w	Beam position (mm).
$\dot{w}$	Beam velocity (rad s^{-1}).
x, y, z	Space coordinates.
i, j, k	Coordinate indices.

GREEK SYMBOLS

ω_b	Beam angular velocity (rad s^{-1}).
υ	Kinematic viscosity (m^2 s^{-1}).
β	Eigen value.
ξ	Convection enhancement ratio.
δ	Normalized tip gap.
ρ	Fluid density (kg m^{-3}).
τ_{ij}	Viscous stress tensor (N m^{-2}).

Manuscript received July 15, 2012; revised February 18, 2013; accepted February 24, 2013. This work was supported in part by the U.S. Department of Commerce under Grant BS123456 and the Universiti Sains Malaysia under RU Grant 1001/PMEKANIK/814163. Recommended for publication by Associate Editor M. Arik upon evaluation of reviewers' comments.

S. F. Sufian is with the School of Mechanical Engineering, Universiti Sains Malaysia, Nibong Tebal 14300, Malaysia (e-mail: sufianfarid@gmail.com).

M. Z. Abdullah is with the School of Mechanical Engineering, Universiti Sains Malaysia, Nibong Tebal 14300, Malaysia (e-mail:mezul@eng.usm.my).

M. K. Abdullah is with the Mechanical Section, Universiti Kuala Lumpur Malaysia Spanish Institute, Kulim 09000, Malaysia (e-mail: khalil80l@gmail.com).

J. J. Mohamed is with the School of Material and Mineral Resources Engineering, Universiti Sains Malaysia, Nibong Tebal 14300, Malaysia (e-mail: srjuliewatty@eng.usm.my).

Color versions of one or more of the figures in this paper are available online at http://ieeexplore.ieee.org.

Digital Object Identifier 10.1109/TCPMT.2013.2251759

I. INTRODUCTION

VARIOUS types of portable electronic devices, such as mini-laptops, tablets, and cellular phones, are rapidly emerging in lighter, slimmer, and more compact forms with high functionalities to meet consumer demands. The heat flux from electronic components of these devices has increased, and this trend is expected to continue in future generations. The thermal management for such devices is confined to passive cooling because of the limited space restrictions, power consumption, weight, and so on. The piezoelectric fan is an airflow generator that induces the flow with a vibrating flexible blade. It has recently been proposed as an alternative device for microelectronic cooling. It consists of a flexible blade bonded with piezoelectric material near its base end. An input signal applied to the piezoelectric material causes an oscillatory motion at the free end of the blade. This signal can induce the surrounding flow with low power consumption. Furthermore, it is adaptable in small spaces.

Many studies have been conducted on the cooling capabilities and flow schemes of piezoelectric fans. Toda [1], [2] proposed the essential models for vibration and airflow by performing experimental and analytical analyses. A study on the local and average heat-transfer coefficients on a vertical surface because of convection from a piezoelectric fan was performed by Schmidt [3]. Açıkalın *et al.* [4] examined the feasibility of placing fans in an actual laptop and cell

phone enclosure. They determined a significant increase in heat transfer in both cases. Ihara and Watanabe [5] investigated 2-D flows around the free ends of a flexible single blade and two blades, both oscillating with a large amplitude. Ro and Loh [6] studied the feasibility of using ultrasonic flexural waves as a cooling mechanism. Analytical, computational, and experimental investigations on incompressible 2-D streaming flows induced by resonating thin beams were conducted by Açıkalın *et al.* [7]. Closed-form analytical streaming solutions were presented for an infinite beam. These solutions were also used to construct a computational scheme to predict the streaming flows from a baffled piezoelectric fan. The predicted asymmetric streaming flows were in good agreement with the experimental flow profiles. Kimber *et al.* [8]–[10] experimentally investigated single and arrayed piezoelectric fans vibrating near an electrically heated stainless steel foil. The temperature field was measured using an infrared camera. 2-D contours of the local heat-transfer coefficient were presented for different vibration amplitudes and gaps. Moreover, correlations were developed with appropriate Reynolds and Nusselt number definitions that describe the area of average thermal performance of the piezoelectric fan with an error of less than 12%. An experimental analysis design for the effects of fan amplitude, tip gap, fan length at resonance frequency, and fan offset from the center of the heat source was reported by Açıkalın *et al.* [11]. The heat-transfer coefficient could be enhanced by as high as 375% with appropriate specifications of the design parameters. A simulation of 2-D computational fluid dynamics and an experimental analysis were performed by Abdullah *et al.* [12] to determine the effect of fan height on the performance of a single piezoelectric fan in horizontally oriented microelectronic cooling. A 2-D finite element method was reported by Florio and Harnoy to enhance the natural convection cooling of a discrete heat source in a vertical channel by using a piezoelectric fan [13]. An enhancement of up to 52% in the local heat-transfer coefficient was observed relative to that achieved by natural convection. Six piezoelectric fans with various blade geometries were constructed and tested on a flat heated surface by Liu *et al.* [14]. They experimentally investigated the influence of geometric parameters, including the horizontal/vertical arrangement and the location of the piezoelectric fan. They found that the heat-transfer augmentation of the piezoelectric fan came from the entrained airflow during each oscillation cycle and the jet-like air stream at the fan tip. The heat-transfer performance of the vertical arrangement exhibited a symmetrical distribution and peaked at the center region, whereas the horizontal arrangement possessed an asymmetrical distribution and demonstrated an early peak. The heat-transfer performance of the horizontal arrangement was not necessarily lower than that of the vertical arrangement. Kimber *et al.* [15] experimentally determined the relationship between the pressure and the flow rate generated by miniature piezoelectric fans. They considered the proximity of the surrounding walls using three different enclosures. The aerodynamic interactions between two vibrating fans were explored by Kimber *et al.* [16]. They found that damping is significantly influenced by the proximity of neighboring piezoelectric fans and by the vibration phase difference. Petroski *et al.* [17] discussed the effect of nozzles on the flow shaping with an unusual heat sink obtained through experimental and computational studies using a laser Doppler anemometry, and 3-D flow fields of the proposed cooling scheme with a piezoelectric fan were also presented. A comparative investigation between 2-D numerical flow simulations and experimental data on particle image velocimetry was conducted by Choi *et al.* [18], [19]. They observed the vortex formation and unsteady flow fields around single- and dual-vibrating fans in the free streams. Recently, an analysis of the 3-D heat and fluid flow induced by a single piezoelectric fan was reported by Lin [20]. Most of the experimental work in the literature focused on the variation of the separation distance between the fan tip and the bare-heated surfaces without considering the existing boundaries in real application, such as side walls. Abdullah *et al.* [21] reported an orientation of multipiezoelectric fan (set in an edge-to-edge arrangement) to enhance the heat transfer of finned heat sink in microelectronic cooling with a 3-D numerical simulation. Their results indicate that an enhancement in convective heat-transfer coefficient exceeding 88% compared with natural convection can be achieved.

Only a few studies [20], [21] have reported on the 3-D simulation of the thermal and flow field induced by the piezoelectric fan. Providing the side walls for the vibrating piezoelectric fan is expected in practical applications, and the effects of the geometric parameters on the fan performance should be considered. However, the coupled effect of the side gap (Gs) and tip gap (δ) of the piezoelectric fan on the thermal performance is currently under investigation. The optimization of these two parameters with the objective of maximizing the heat-transfer rates is vital. Against this background, this work aims to determine the effect of Gs and δ on the cooling performance of a single piezoelectric fan, which is vertically oriented between two adjustable walls. The heat source is an aluminum foil heated from the bottom using a stainless steel electrical heater attached beneath the foil. 3-D simulation using FLUENT 6.3.2 was performed with a user-defined function (UDF) to describe the motion of a vibrating fan. The transient flow and temperature were analyzed according to higher and lower rates of heat-transfer measurement.

II. Experimental Setup and Procedure

A commercial piezoelectric fan consisting of a bimorph-lead zirconate titanate patch bonded to a thin stainless steel blade was used in this investigation for cooling because of its high elongation properties at a relatively low power input (see Table I for the specifications).

The spacing effects on the piezoelectric fan were tested experimentally. The spacing between the neighboring walls and the fan side edges is defined as the side gap (G_s), and δ is the ratio of the fan-tip spacing to the height of the side wall. The experimental procedure was performed with the measurements of the piezoelectric fan amplitude obtained by a laser displacement sensor (KEYENCE LK-G152). With the objective of maximizing heat dissipation, thermal analysis was conducted to assess the coupled effect of δ and G_s on a heat surface (chip).

TABLE I
SPECIFICATIONS OF THE PIEZOELECTRIC FAN (PIEZO SYSTEMS INC., USA)

Specification	Value
Material	Stainless steel
Size (mm)	47 (l_{pf}) × 12 (D_{pf}) × 0.4 (t_{pf})
Height without patch (mm)	23 (l_u)
Power consumption (mW)	42
Weight (kg)	0.002

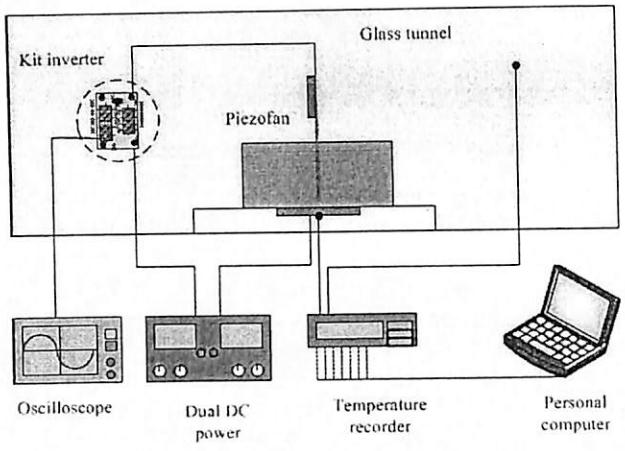

Fig. 1. Schematic of experimental setup for heat-transfer study.

A. Fan Amplitude Testing

A laser displacement sensor (KEYENCE LK-G152) was utilized to detect the fan-tip deflection and measure the amplitude. The measurement point of the focal laser beam to the fan surface was 1 mm from the fan tip. A digital storage (DSO3062A Oscilloscope) connected to an inverter drive circuit was provided to tune the frequencies and supply the input signals for the fan. The inverter circuit was also joined with an input channel provided by a DC dual power supply (GWinstek GPS2303) to deliver the voltages required for the fan operation. The other channel was fed the chip (heat source). The inverter circuit was used to convert DC to AC to drive the piezoelectric fan. The frequency was adjusted by turning the trimmer pot on the printed circuit board. The piezoelectric fan was driven at a resonance frequency (approximately 111 Hz) with an input of 42 mW. As the piezoelectric fan ran, the IMC DAQ system recorded the input displacement with a frequency signal of the sensor and stored it in the computer. The vibration amplitude was measured for the corresponding G_s and δ variations. The error of the displacement sensor was $-/+0.02\%$.

B. Thermal Analysis

The electronic package (chip) was simulated using an aluminum foil (size 52 × 15 × 1 mm), which was heated with a uniform heat flux of 2435.89 W/m^2 through a stainless steel electrical heater placed beneath the foil. A heat-sink compound RS of high conductivity was used to glue the heater to the foil. The foil-heater was fixed into the cavity of a wooden platform so that their top surfaces were coplanar. The wooden platform served as an isolator and enabled only the

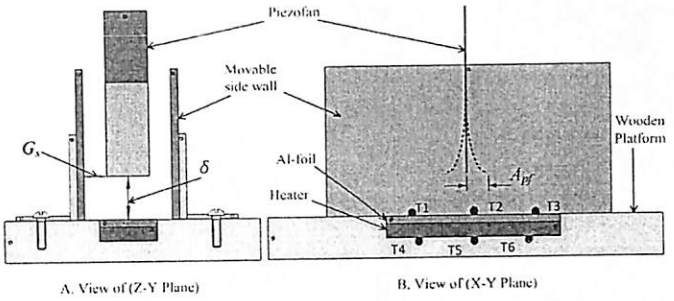

Fig. 2. Details of the experimental setup inside the glass tunnel for heat-transfer study.

top surface of the heated foil to be exposed to the ambient environment. Therefore; the heat loss through the wooden platform was assumed negligible. Two parallel adjustable side walls of 82 mm in length and 35 mm in height were arranged on the top surface of the platform on both sides of the foil. Figs. 1 and 2 exhibit the schematics of the experimental setup.

The piezoelectric fan was oriented vertically between the side walls over the foil surface and held rigidly by an adjustable stand (ON/OFF magnetic base type of MB-15) for the height variety. This arrangement yielded significant heat dissipation [8]. The heater was powered by the DC output of a digital power supply to obtain a constant input (Q°) of 1.9 W. Three thermocouples (K-type, TTK-36-SLE) were attached to the exposed surface of the foil to calculate the average surface temperature, and three were placed beneath the heater. All these thermocouples were linked to a desktop PC utilizing a data acquisition system (Advantech USB-4718, 8-channel). The temperatures were recorded every 60 s. Transient and steady-state temperatures were recorded in natural and forced (with the piezoelectric fan switched on) convection conditions. The ambient environment was always maintained at 25 °C. The assembly of the chip and side walls embedded with the piezoelectric fan was housed in a glass tunnel to reduce the ambient effects. The rate of heat flux (q°) generated by the heat source can be computed according to the following equation:

$$q^{\circ} = \frac{Q^{\circ}}{A_{mc}} \tag{1}$$

where Q° and A_{mc} are the power input (6.66 W) and surface area of the heated surface, respectively.The average heat-transfer coefficient ($\overline{h}$) is defined based on the difference between the average temperature of the heated surface and the ambient temperature

$$\overline{h} = \frac{q^{\circ}}{(\overline{T}_s - T_a)} \tag{2}$$

where $\overline{T}_s$ is the average temperature of the heated surface, and T_a is the ambient temperature. To assess the importance of the cooling result achieved by the piezoelectric fan, the enhancement ratio (ξ) [14] that represents the convection during fan operation is divided by that under natural convection

$$\xi = \overline{h}_{pf}/\overline{h}_n \tag{3}$$

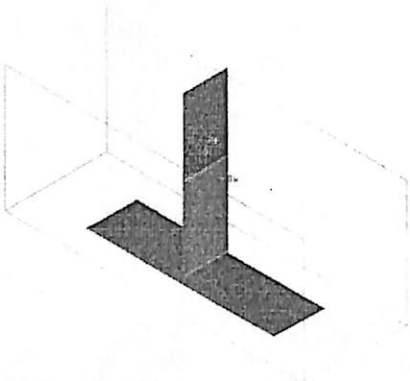

Fig. 3. Positions of piezoelectric fan and side walls.

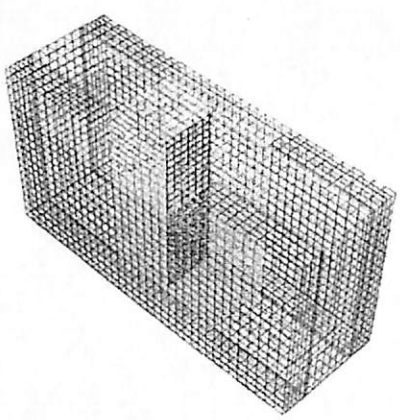

Fig. 4. Meshed models.

where $\overline{h}_{pf}$ is the average heat-transfer coefficient achieved under force convection (ON-piezoelectric fans), and $\overline{h}_n$ is the average heat-transfer coefficient achieved under natural convection condition (OFF-piezoelectric fans).

The Reynolds number (Re) according to the fan tip deflection (ωA) is computed by

$$Re = \frac{\omega_b A_{pf} D_{pf}}{\upsilon}. \tag{4}$$

III. Modelling and Numerical Methods

The simulation model was used to examine the correlation between the flow field induced by the piezoelectric fan and the heat removal from the chip surface. The 3-D model used in this simulation consists of aluminum foil, simple side walls, and a piezoelectric fan (Fig. 3). The size of the heat source is similar to that of the heater used in the experiment. The clamp of the piezoelectric fan was neglected. The fan boundary was modeled as a moving adiabatic wall with a location in time, set by a UDF in FLUENT. The fan was modeled as an infinitesimally thin wall with no thermal conduction passing through it. No-slip boundary conditions were applied to the platform and side walls. Other boundaries were treated as pressure boundaries, permitting the airflow inward or outward. A combination of tetrahedral and quad literal elements (approximately half a million) was used for meshing (Fig. 4).

The fluid domain was divided into two regions, namely, region a and region b (Fig. 5), and the boundary of these

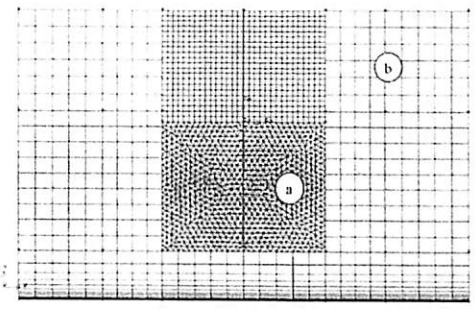

Fig. 5. Mesh generation regions.

two regions was imposed as a fluid interface. The purpose of the fluid interface is to avoid the damaged fluid cells because region a of the fluid domain includes the deforming beam (piezoelectric fan). Only single-cell spacing was included from the tip of the beam to the fluid interface to avoid stretching, which could lead to the failure of fluid cells. Region b is distinguished by stationary fluid cells that interact with region a through the fluid interface. FLUENT offers many options for the dynamic mesh mechanism, but only smoothing and remeshing mechanisms were selected. Smoothing considers the movement of the fluid zone as a spring-like deformation, and remeshing is used to remesh the cells if their new volume is smaller than the prescribed value [22].

A. Mathematical Model

The flow was assumed to be incompressible and turbulent. The governing equations used in FLUENT for describing the transient fluid flow are as follows:

Continuity

$$\frac{\partial \rho}{\partial t} + \frac{\partial}{\partial x_i}(\rho u_i) = 0. \tag{5}$$

Momentum (nonaccelerating reference frame)

$$\frac{\partial}{\partial t}(\rho u_i) + \frac{\partial}{\partial x_j}(\rho u_i u_j) = -\frac{\partial P}{\partial x_j} + \frac{\partial \tau_{ij}}{\partial x_j} + \rho g_i + F_i \tag{6}$$

where ρ is the fluid density, P is the pressure in the fluid, τ_{ij} is the viscous stress tensor, and g_i is the gravitational acceleration in the i-direction.

Energy

$$\frac{\partial}{\partial t}(\rho c_p T) + \frac{\partial}{\partial x_j}(\rho u_i u c_p T) = k\frac{\partial^2 T}{\partial x_j^2} \tag{7}$$

where c_p is the specific heat of air, T is the temperature, and k is the thermal conductivity. The mode shape of a vibrating fan is treated as a clamped-free beam such as that proposed in [21]. Assuming a sinusoidal driving, position of the beam is as follows:

$$w(x,t) = A_{pf} \cdot \begin{bmatrix} (\sin(\beta l_u) - \sinh(\beta l_u))(\sin(\beta x) - \sinh(\beta x)) \\ +(\cos(\beta l_u) - \cosh(\beta l_u))(\cos(\beta x) - \cosh(\beta x)) \end{bmatrix} \cdot \sin(\omega_b t). \tag{8}$$

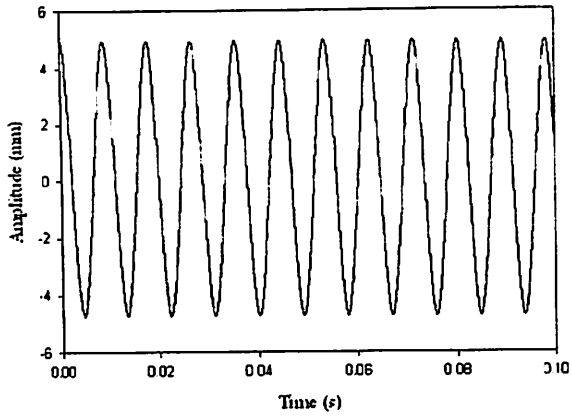

Fig. 6. Amplitude from a sample test of vibrating fan.

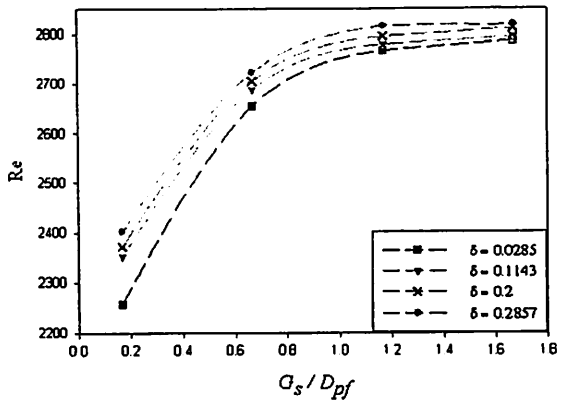

Fig. 7. Coupled effect of tip and side gaps on *Re*.

Differentiating this equation with respect to time provides the velocity of the beam.

$$\dot{w}(x,t) = A_{\mathrm{pf}} \cdot \left[\begin{array}{l} (\sin(\beta l_u) - \sinh(\beta l_u))(\sin(\beta x) - \sinh(\beta x)) \\ +(\cos(\beta l_u) - \cosh(\beta l_u))(\cos(\beta x) - \cosh(\beta x)) \end{array} \right] \cdot \omega_b \cos(\omega_b t) \quad (9)$$

where β values can be calculated from the frequency equation

$$\cos(\beta l_u) \cdot \cosh(\beta l_u) = -1. \quad (10)$$

This must be solved numerically, yielding infinity solutions of β. The β value corresponding to the first mode shape is

$$\beta = \frac{1.875}{l_u}. \quad (11)$$

B. Simulation

The first-order upwind discretization scheme was used for both momentum and energy equations with the SIMPLE scheme for pressure–velocity coupling. For the treatment of the turbulent flow in the near-wall region (heat source surface), the y^+ value was set as 1. The shear stress transport k-ω model was used to describe the flow induced by the piezofan, which has local turbulence. The beam was assumed to vibrate at a frequency of 100 Hz; this round-off (compared with the experimental value of 111 Hz) was done to achieve numerical stability. Time-step size of 0.0001 s was selected for all the cases, with 100 time steps per cycle of fan vibration. This value was determined after three attempts to check the trend and proximity with the profiles investigated; for instance, the trials were conducted by increasing the mesh elements and decreasing the time steps. However, a problem emerged when the mesh elements increased because of the negative volume or less memory detected in FLUENT during analysis. This problem is typically found in a dynamic meshing setup. The total duration of the simulation is selected such that the temperature reaches a steady value during this period. The simulation used 5,000 iterations, corresponding to approximately 3 days of computation time per case on a computer with a Pentium Dual Core processor (2.8 GHz) and 2.0 GB of memory.

IV. Results and Discussion

A. Experimental Results

1) Effect of δ and G_s on Re: A reading from the laser displacement sensor (output signal) of the fan amplitude is presented in Fig. 6. The oscillator (vibrating fan) history exhibits a traveling wave during time with a discrepancy of 0.43% between the output and input signals because the output frequency is 111.35 Hz and the inverter circuit input frequency is 111.84 Hz. The influence of δ and G_s on the corresponding *Re* is computed according to the vibrating fan amplitude [15]. The *Re* is plotted against the ratio of G_s to the fan width D_{pf} for each δ value (Fig. 7). A gradual increase in *Re* is observed with the increase in side gap until approximately $G_s/D_{\mathrm{pf}} = 1.2$, and then *Re* remains steady, which indicates that G_s has no further influence on *Re*. The minimum Reynolds number at $G_s/D_{\mathrm{pf}} = 0.2$ and $\delta = 0.0285$. As G_s decreases, the side walls cause damping on the vibrating piezoelectric fan, thus reducing *Re*. However, in the smaller tip gap, despite the decrease in *Re*, we observed a higher heat-transfer rate because of the proximity of the peak velocity zone to the heated surface, as will be elucidated in the next section.

2) Heat-Transfer Coefficient: The transient temperature history under natural and forced convection modes for different positions of thermocouples on the heat source is shown in Fig. 8. At $t = 0$, the heater was switched on in natural convection, and the steady state was achieved at $t = 3600$ s. The piezofan was switched on at $t = 3600$ s, and the temperatures were recorded until a fresh steady state was reached. The piezoelectric fan caused a drastic reduction in the source temperature because of the enhanced heat removal. The average heat-transfer coefficient obtained under natural convection $\bar{h}_{\mathrm{n}}$ (OFF-piezoelectric fan) is approximately 44 W/m^2·K. For the forced convection, the average heat-transfer coefficient $\bar{h}_{\mathrm{pf}}$ (ON-piezoelectric fan) in a representative experiment is presented in Fig. 9 according to the coupled effect of δ and G_s. Decreasing the separation distance δ between the blade tip and the heated surface results in an expected enhancement in the heat-transfer coefficient for all cases because the approximated vibrating blade, which enabled a jet velocity of air stream, stroked the heated surface efficiently. Approximated side walls from the vibrating fan yield to the reduction of amplitude, and

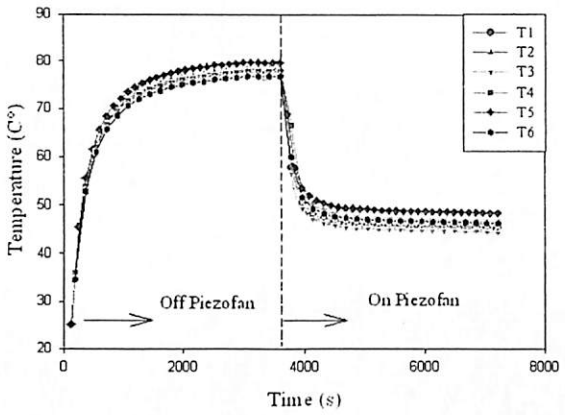

Fig. 8. Temperature histories for natural and forced convection conditions.

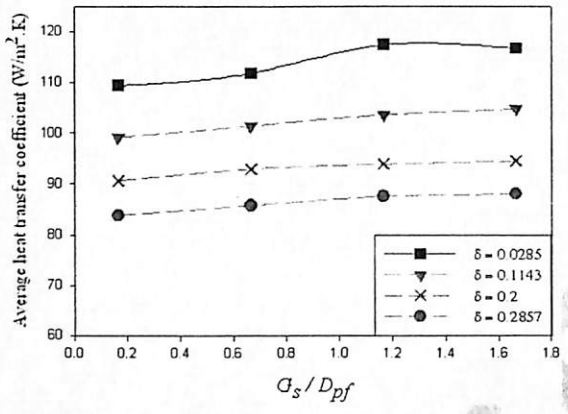

Fig. 9. Coupled effect of tip and side gaps on average heat-transfer coefficient.

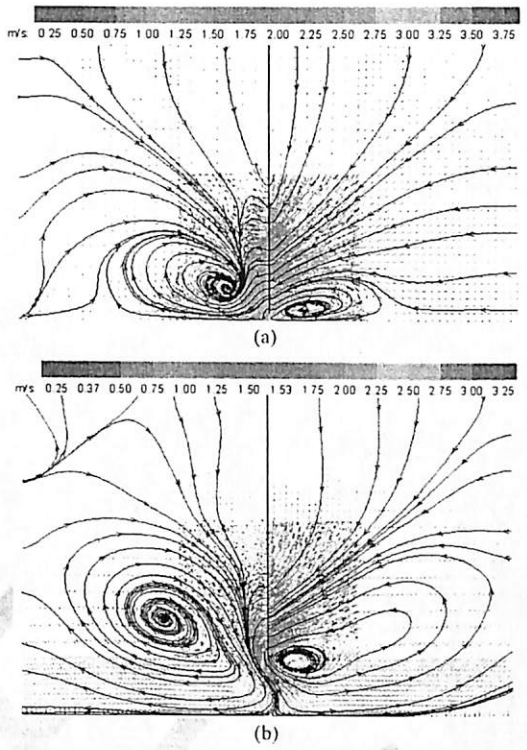

Fig. 10. Velocity vectors and streamlines for (a) best case and (b) worst case.

TABLE II
EXPERIMENTAL UNCERTAINTIES

Parameter	Maximum Uncertainty (%)
Temperature	±2.08
Average heat-transfer coefficient	±4.54
Enhancement ratio	±4.47
Re	±1.74

thus air stream is reduced under a specific vibrating frequency. The piezoelectric fan amplitude decreases because of the viscous drag of the flow, thus reducing the cooling capacity [11]. The increase in G_s/D_{pf} from 0.2 to 1.2 increases $\overline{h}_{pf}$ and then remains steady. Thus, for the minimum δ of 0.0285, G_s is suitable in providing maximum heat removal. However, δ is more significant in $\overline{h}_{pf}$ compared with G_s. Based on the heat-transfer performance, the optimum values of δ and G_s/D_{pf} in the present study were obtained as 0.0285 and 1.2, respectively.

The heat-transfer enhancement ratio ξ of the piezoelectric fan was evaluated based on (3) for the lower and higher convection rate cases. The piezoelectric fan enhances the heat-transfer performance approximately 1.95–2.7 times for the heated surface. These findings indicate that the geometric parameter for the installation process of the piezoelectric fan significantly affects effective heat removal and is an important factor to be considered in the actual implementation. The uncertainty analysis, as reported in [23], has been performed to check the accuracy of measurements in the present study. The experimental uncertainties for the above-mentioned parameters are summarized in Table II. It has been obtained after making five trials of measurements, which is based on average temperatures during the steady-state operation. For each parameter, the mean, standard deviation, and standard error are calculated. The results of the error analysis indicate that the measurements are within the acceptable accuracy limits.

B. Numerical Results

Based on the heat-transfer map, which was presented experimentally in the previous section, only two configurations were selected for simulation. These configurations, namely, best case and worst case, correspond to the higher and lower rate of heat transfer, respectively (Fig. 8).

1) Flow Field: The correlation between the flow field induced by the piezoelectric fan and heat-transfer behavior needs to be clarified. Therefore, the numerical solution offers a practical approach to obtain an accurate analysis for the complexity of the transient flow field induced by a vibrating fan. Fig. 10(a) and (b) present the velocity vectors and streamlines induced by a vibrating fan on the middle plane of the computational domain for the best and worst cases in the natural position of the fan. As the fan turns periodically to the right and left sides, two vortices are seen to be formed as a counterclockwise vortex on the right and a clockwise vortex on the left. The trajectory of these vortices is alternate as well as according to the direction of the fan. These two counter vortexes formed by the fan are comparable with those obtained by 2-D simulation in [11]. As the tip gap is minimal,

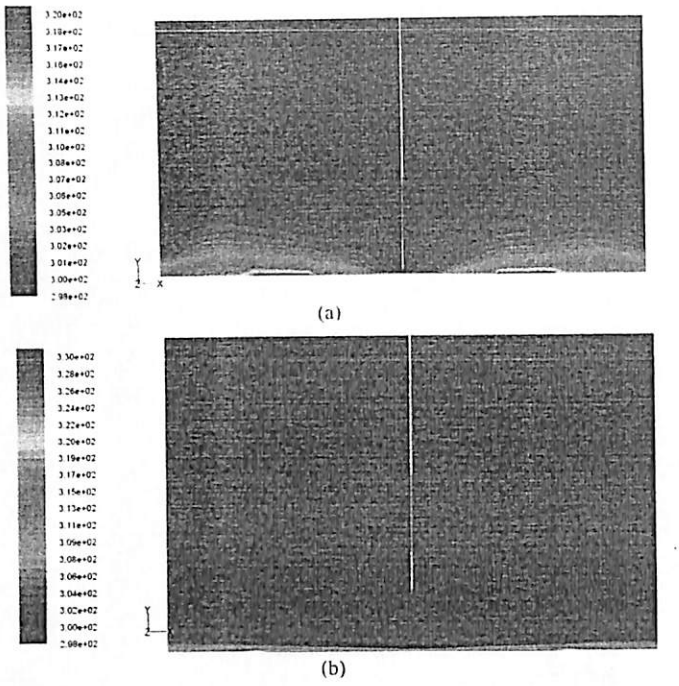

Fig. 11. Temperature contours (k) at middle plane of computational domain for (a) best case and (b) worst case.

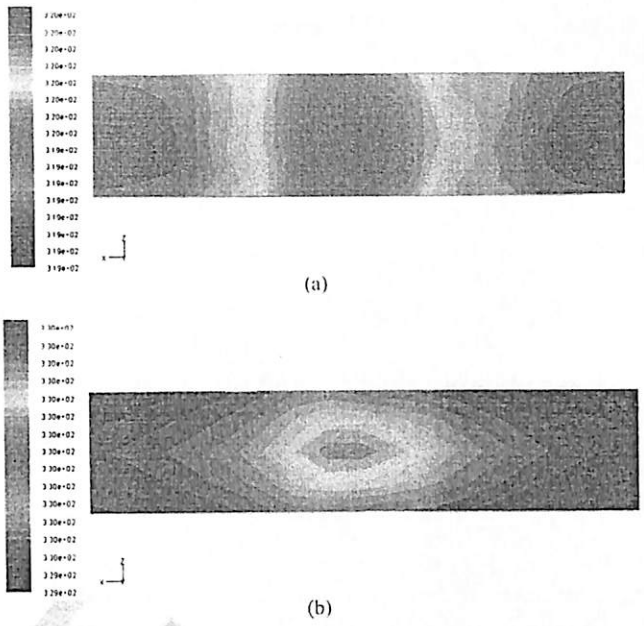

Fig. 12. Temperature contours (K) top view of the foil for (a) best case and (a) worst case.

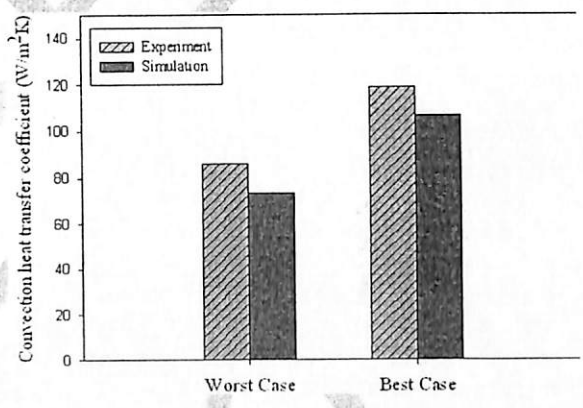

Fig. 13. Comparison of predicted and experimental heat-transfer coefficients.

the piezoelectric fan vibration causes the jet flow to be highly impinged on the heated surface, forcing the fluid to displace rapidly. Thus, the high-velocity zone is mostly localized in the vicinity of the heated surface, enabling an effective heat removal. The vortex zones in the best case are in direct contact with the heated surface, which facilitates the enhanced heat removal. For the worst case, the tip gap is maximum, whereas the fluid agitation near the hot surface is minimal. The highest velocity zone is situated in the near-tip region, which is relatively far from the heat source and is not effectively exploited for cooling. The vortex zones on both sides of the fan are larger and farther from the heated surface compared with those in the best case; this condition prompts the fluid to lose a significant amount of momentum as it reaches the hot surface, resulting in decreased heat-transfer rates.

2) Thermal Analysis: The temperature contours of the force convection on the middle plane of the computational domain for the best and worst case configurations are presented in Fig. 11(a) and (b), respectively. For the best case, as the separation distance between the fan and heated surface (δ) is minimal, the vibrating fan can agitate the development of the thermal boundary layer on the heated surface, resulting in high heat dissipation. Therefore, the thermal boundary generated on the heated surface seems to rupture into two symmetrical regions on the left and right sides of the vibrating fan because of the fluid displacement. The center zone, which is directed to the vibration envelope, exhibits a significant drop in temperature gradient; this phenomenon can maximize the heat dissipation over the heated surface. Moreover, increasing the side-gap (G_s) yield increases the vibrating amplitude as well, enabling a larger jet velocity of the flow stream impingement. Thus, the results of heat transfer improve. By contrast, the temperature decreases as the tip gap (δ) increases for the worst case. This result is attributed to the flow velocity reduction on the heated surface, thus resulting in a lower rate of heat transfer relative to that obtained by the best case. This observation is expected to be reasonable according to the velocity profiles, as previously explained.

Fig. 12(a) and (b) exhibit the corresponding temperature contours on the heated surface. For the best case, a droplet cooling zone is observed at the center of the heated foil, and this droplet appears to be symmetric in the direction of the piezoelectric fan vibration. The droplet zones widen laterally because of the induced swirling flow on both sides of the vibrating fan. However, for the other case, the temperature drop is lower than that of the best one because of the large tip gap with a small side gap. The effects of the side gap on the side edge of the foil are obvious, as evidenced by the hotter zones compared with the center. This result indicates that the flow at the side edges of the foil was decelerated because of the small side gap ($G_s = 1$ mm), and the flow was accelerated along the center line. Both profiles agree that this droplet cooling zone is prominent at the center of the foil. This

result is attributed to the enhanced cooling of the central foil because of the presence of the piezoelectric fan in both cases.

Fig. 13 illustrates the comparison between measured and computed heat-transfer coefficients for the best and worst cases achieved on the heated surface. The general agreement is good. The deviations between numerical simulation and experimental work are estimated to be 15% and 11.3% for the worst and best cases, respectively, which are attributed to the omission of the radiation effect in the numerical model and the slightly different effect of the beam frequency. This presumption was verified by deducting the experimentally determined radiative contribution based on the predicted value. Moreover, the thickness of the thermal compound in the simulation was treated as uniform in all cases; the real thickness was not necessarily so, as the compound was manually applied. Furthermore, the ambient temperature in the experiments was measured with a single thermocouple, and the average fluid temperature inside the domain was used in the simulation.

V. Conclusion

The coupled effect of the side gap and tip gap on the cooling performance of a single piezoelectric fan was investigated experimentally and then numerically analyzed. The influence of geometric parameters was enhanced by the objective of maximizing the average of heat-transfer coefficient. A 3-D model using FLUENT 6.3.2 was employed to simulate the best and worst cases to clarify the flow field and the resulting heat transfer. Detailed amplitude measurement and transient flow were conducted to substantiate the heat-transfer study. The estimated results were compared with the experimental findings, and the agreement was good.

The following conclusions were drawn.

1) Tip and side gaps are crucial to the flow induced by the piezoelectric fan and the resulting heat removal from the chip. In general, lower tip gaps and moderate side gaps are recommended.
2) For a given tip gap, a range of the side gaps exist that affect the flow velocity, beyond which the side gap has no influence on the induced flow.
3) The tip gap must be as minimal as possible, and the side gap needs to be carefully selected to maximize the heat-transfer rates.
4) The piezoelectric fan enhances the measured heat-transfer coefficient 1.95 times to 2.7 times, corresponding to the best and worst cases, respectively.

References

[1] M. Toda, "Theory of air flow generation by a resonant type PVF2 Bimorph cantilever vibrator," *Ferroelectrics*, vol. 22, no. 1, pp. 911–918, 1979.

[2] M. Toda, "Voltage-induced large amplitude bending device PVF2 Bimorph its properties and applications," *Ferroelectrics*, vol. 32, no. 1, pp. 127–133, 1981.

[3] R. R. Schmidt, "Local and average transfer coefficients on a vertical surface due to convection from a piezoelectric fan," in *Proc. Inter Soc. Conf. Thermal Phenomena Electron. Syst.*, May 1994, pp. 41–49.

[4] T. Açikalin, S. M. Wait, S. V. Garimella, and A. Raman, "Experimental investigation of the thermal performance of piezoelectric fans," *Heat Transf. Eng.*, vol. 25, no. 1, pp. 4–14, 2004.

[5] A. Ihara and H. Watanabe, "On the flow around flexible plates, oscillating with large amplitude," *J. Fluids Struct.*, vol. 8, no. 7, pp. 601–619, 1994.

[6] P. I. Po and L. Byoung-Gook, "Feasibility of using ultrasonic flexural waves as a cooling mechanism," *IEEE Trans. Ind. Electron.*, vol. 48, no. 1, pp. 143–150, Feb. 2001.

[7] T. Acikalin, A. Raman, and S. V. Garimella, "Two-dimensional streaming flows induced by resonating, thin beams," *J. Acoust. Soc. Amer.*, vol. 114, no. 4, pp. 1785–1795, 2003.

[8] M. Kimber, S. V. Garimella, and A. Raman, "Local heat transfer coefficients induced by piezoelectrically actuated vibrating cantilevers," *J. Heat Transf.*, vol. 129, no. 9, pp. 1168–1176, 2007.

[9] M. Kimber and S. V. Garimella, "Measurement and prediction of the cooling characteristics of a generalized vibrating piezoelectric fan," *Int. J. Heat Mass Transf.*, vol. 52, nos. 19–20, pp. 4470–4478, 2009.

[10] M. Kimber and S. V. Garimella, "Cooling performance of arrays of vibrating cantilevers," *J. Heat Transf.*, vol. 131, no. 11, pp. 111401-1–111401-5, 2009.

[11] T. Açikalin, S. V. Garimella, A. Raman, and J. Petroski, "Characterization and optimization of the thermal performance of miniature piezoelectric fans," *Int. J. Heat Fluid Flow*, vol. 28, no. 4, pp. 806–820, 2007.

[12] M. K. Abdullah, M. Z. Abdullah, M. V. Ramana, C. Y. Khor, K. A. Ahmad, M. A. Mujeebu, Y. Ooi, and Z. M. Ripin, "Numerical and experimental investigations on effect of fan height on the performance of piezoelectric fan in microelectronic cooling," *Int. Commun. Heat Mass Transf.*, vol. 36, no. 1, pp. 51–58, 2009.

[13] L. A. Florio and A. Harnoy, "Use of a vibrating plate to enhance natural convection cooling of a discrete heat source in a vertical channel," *Appl. Thermal Eng.*, vol. 27, no. 13, pp. 2276–2293, 2007.

[14] S.-F. Liu, R.-T. Huang, W.-J. Sheu, and C.-C. Wang, "Heat transfer by a piezoelectric fan on a flat surface subject to the influence of horizontal/vertical arrangement," *Int. J. Heat Mass Transf.*, vol. 52, nos. 11–12, pp. 2565–2570, 2009.

[15] M. Kimber, K. Suzuki, N. Kitsunai, K. Seki, and S. V. Garimella, "Pressure and flow rate performance of piezoelectric fans," *IEEE Trans. Compon. Packag. Technol.*, vol. 32, no. 4, pp. 766–775, Dec. 2009.

[16] M. Kimber, R. Lonergan, and S. V. Garimella, "Experimental study of aerodynamic damping in arrays of vibrating cantilevers," *J. Fluids Struct.*, vol. 25, no. 8, pp. 1334–1347, 2009.

[17] J. Petroski, M. Arik, and M. Gursoy, "Optimization of piezoelectric oscillating fan-cooled heat sinks for electronics cooling," *IEEE Trans. Compon. Packag. Technol.*, vol. 33, no. 1, pp. 25–31, Mar. 2010.

[18] M. Choi, C. Cierpka, and Y. H. Kim, "Vortex formation by a vibrating cantilever," *J. Fluids Struct.*, vol. 31, pp. 67–78, May 2012.

[19] M. Choi, S.-Y. Lee, and Y.-H. Kim, "On the flow around a vibrating Cantilever pair with different phase angles," *Eur. J. Mech., B/Fluids*, vol. 34, pp. 146-157, Feb. 2012.

[20] C.-N. Lin, "Analysis of three-dimensional heat and fluid flow induced by piezoelectric fan," *Int. J. Heat Mass Transf.*, vol. 55, nos. 11–12, pp. 3043–3053, 2012.

[21] M. K. Abdullah, N. C. Ismail, M. A. Mujeebu, M. Z. Abdullah, K. A. Ahmad, M. Husaini, and M. N. A. Hamid, "Optimum tip gap and orientation of multi-piezofan for heat transfer enhancement of finned heat sink in microelectronic cooling," *Int. J. Heat Mass Transf.*, vol. 55, nos. 21–22, pp. 5514–5525, 2012.

[22] *Modeling Flows Using Sliding and Deforming Meshes FLUENT 6.3.26*, FLUENT Inc. Lebanon, NH, USA, 2006.

[23] J. Taylor, *An Introduction to Error Analysis: The Study of Uncertainties in Physical Measurements*, 2nd ed. Sausalito, CA, USA: University Science Books, 1997, pp. 94–104.

Shaker Farid Sufian received the Graduate degree in mechanical engineering from the University of Technology, Baghdad, Iraq, in 2003, and the Masters degree in computational fluid dynamics from Universiti Sains, Malaysia, in 2010. He is currently pursuing the Ph.D. degree in advanced cooling technique in microelectronics.

His current research interests include electronics cooling, fluid/structure interaction, fluid mechanics, and heat transfer.

Mohd Zulkifly Abdullah received the Bachelors degree in mechanical engineering from the University of Wales, Swansea, U.K., and the M.Sc. and Ph.D. degrees from the University of Strathclyde, Glasgow, U.K.

He has been a Professor of mechanical engineering with Universiti Sains Malaysia, Malaysia, since 2010. He has authored numerous publications in international journals and conference proceedings. His current research interests include CFD, heat transfer, electronic packaging, and electronic cooling.

Muhammad Khalil Abdullah received the B.Eng, M.Sc. and Ph.D. degrees in mechanical engineering from the School of Mechanical Engineering, Prestige and Accelerated Programme for Excellence (APEX) University, Universiti Sains Malaysia, in 2004, 2007, and 2012, respectively.

He is currently a Senior Lecturer in mechanical section from Universiti Kuala Lumpur Malaysia Spanish Institute, Kuala Lumpur, Malaysia. His current research interests include heat transfer, fluid flow, electronic packaging and cooling, CFD and polymer theology.

Julie Juliewatty Mohamed received the Bachelors degree in materials and mineral resources engineering and the M.Sc. and Ph.D. degrees from Universiti Sains Malaysia, Malaysia.

She has been a Lecturer of materials and mineral resources engineering with Universiti Sains Malaysia, since 2008. She has authored numerous publications in international journals and conference proceedings. Her current research interests include piezoelectric and dielectric electroceramic, intermetallic, and composites materials.

International Communications in Heat and Mass Transfer 43 (2013) 81–89

Contents lists available at SciVerse ScienceDirect

International Communications in Heat and Mass Transfer

journal homepage: www.elsevier.com/locate/ichmt

Effect of synchronized piezoelectric fans on microelectronic cooling performance ☆

S.F. Sufian [a,*], M.Z. Abdullah [a], J.J. Mohamed [b]

[a] School of Mechanical Engineering, Universiti Sains Malaysia, Engineering Campus, 14300 Nibong Tebal, Penang, Malaysia
[b] School of Material and Mineral Resources Engineering, Universiti Sains Malaysia, Engineering Campus, 14300 Nibong Tebal, Penang, Malaysia

ARTICLE INFO

Available online 1 March 2013

Keywords:
Electronic cooling
Piezoelectric fan
Transient numerical simulation
Fluent
MpCCI
Heat transfer enhancement

ABSTRACT

This study reports on the influence of dual vibrating fans on flow and thermal fields through numerical analyses and experimental measurements. Two piezoelectric fans were arranged face to face and were vertically oriented to the heat source. 3D simulation was performed with FLUENT and ABAQUS with the use of code coupling interface MpCCI to calculate the velocity and temperature distribution on the horizontal hot plate. The fans' motion was described as deformable parts by ABAQUS at their first mode vibration. The effects of vibration phase difference between the fans corresponding to in-phase ($\Phi = 0°$) and out-of-phase ($\Phi = 180°$) vibrations were explored in terms of transient temperature and flow fields. The purpose is to enhance heat dissipation from the microelectronic component. Comparison with the performance of a single fan is made to assess the significance of the additional fan on thermal performance. Good comparison results were achieved through accurate modeling of the most important features of the fans and through heat transfer. Computed results show that the single fan enhanced heat transfer performance within approximately 2.3 times for the heated surface. By contrast, the dual fans enhanced heat transfer performance within approximately 2.9 for out-of-phase vibration ($\Phi = 180°$) and 3.1 for in-phase vibration ($\Phi = 0°$).

1. Introduction

Computers and portable electronic devices, such as cellular phones, laptops, and tablets, are rapidly emerging in lighter, slimmer, and more compact forms with high functionalities to meet consumer demands. However, the cooling requirements for such devices are crucial, and perhaps, traditional rotary fans have become impractical because of installation restrictions into limited space. Piezoelectric fans are microvibrating machines that have been recently proposed as airflow generators to help dissipate heat. They consist of a cantilever beam bonded with a piezoelectric material near their base ends. An input signal to the piezoelectric material causes oscillatory motion at the free end of the beam; this signal could induce the surrounded flow with low power consumption. Piezoelectric fans are also noise-free and adaptable in small spaces.

Numerous studies have been conducted on the cooling capabilities and flow schemes of piezoelectric fans. Toda [1,2] proposed the essential models for vibration and airflow by performing experimental and analytical analyses. A study on the local and average heat transfer coefficients on a vertical surface because of convection from a piezoelectric fan was performed by Schmidt [3]. Açıkalın et al. [4] examined the feasibility of placing fans in an actual laptop and cell phone enclosure. They determined a significant increase in heat transfer in both cases. Ihara and Watanabe [5] investigated quasi 2D flows around the free ends of a flexible single plate and two plates, both oscillating with a large amplitude. Ro and Loh [6] studied the feasibility of using ultrasonic flexural waves as a cooling mechanism. Analytical, computational, and experimental investigations on incompressible 2D streaming flows induced by resonating thin beams were conducted by Açıkalın et al. [7]. Closed-form analytical streaming solutions were presented for an infinite beam; these solutions were also used to motivate a computational scheme to predict the streaming flows from a baffled piezoelectric fan. The predicted asymmetric streaming flows were in good agreement with the experimental flow profiles. Kimber et al. [8–10] experimentally investigated single and arrayed piezoelectric fans vibrating near an electrically heated stainless steel foil. The temperature field was measured by an infrared camera. 2D contours of the local heat transfer coefficient were presented for different vibration amplitudes and gaps. Moreover, correlations were developed with appropriate Reynolds and Nusselt number definitions that described the area average thermal performance of the piezoelectric fan with an error of less than 12%. An experimental analysis design for the effects of fan amplitude, tip gap, fan length at resonance frequency, and fan offset from the center of the heat source was reported by Açıkalın et al. [11]. The heat transfer coefficient could be enhanced by as much as 375% with appropriate specifications of the design parameters. 2D computational fluid dynamics simulation and experimental analysis were performed by Abdullah et al. on the effect of fan height on the performance of a single piezoelectric fan in microelectronic cooling horizontally oriented [12]. A 2D finite element method was reported by Florio and Harnoy to

☆ Communicated by W.J. Minkowycz.
* Corresponding author.
E-mail address: sufianfarid@gmail.com (S.F. Sufian).

0735-1933/$ – see front matter © 2013 Elsevier Ltd. All rights reserved.
http://dx.doi.org/10.1016/j.icheatmasstransfer.2013.02.013

Nomenclature

A_{pf}	amplitude of piezofan (mm)
A_{mc}	exposed surface area of the microelectronic component (m^2)
l_{pf}	length of piezofan (mm)
D_{pf}	width of piezofan (mm)
t_{pf}	piezofan thickness (mm)
l_u	length of un-patch piezofan (mm)
q''	heat flux (W m^{-2})
Q''	power input to the heat source (W)
$\overline{h}$	average heat transfer coefficient (W m^{-2} K^{-1})
$\overline{T}_s$	average temperature of heated surface (K)
T_a	ambient temperature (K)
$\overline{h}_{pf}$	average force convection (W m^{-2} K^{-1})
$\overline{h}_n$	average natural convection (W m^{-2} K^{-1})
$\vec{u}$	velocity vector
u	velocity (m s^{-1})
$\vec{u}_g$	local grid velocity
f	volume force
x, y, z	space coordinates
i, j, k	coordinate indices
t	time (s)
P	static pressure (N m^{-2})
g	gravitational acceleration (m s^{-2})
c_p	specific heat of air (J kg^{-1} K^{-1})
T	temperature (K)
k	thermal conductivity (W m^{-1} K^{-1})
CCW	counter-clockwise
CW	clockwise

Greek symbols

Φ	vibration phase angle (degree)
	traveling wave phase angle (degree)
ξ	heat transfer coefficient enhancement ratio
δ	dimensionless spacing between fan tip and heated surface
ρ	fluid density (kg m^{-3})
σ	Cauchy stress tensor
τ_{ij}	viscous stress tensor (N m^{-2})

enhance the natural convection cooling of a discrete heat source in a vertical channel with the use of a piezoelectric fan [13]. An enhancement of up to 52% in the local heat transfer coefficient was observed relative to that achieved by natural convection. Six piezoelectric fans with various blade geometries were made and tested on a flat heated surface by Liu et al. [14]. They experimentally investigated the influence of geometric parameters, including horizontal/vertical arrangement and location of the piezoelectric fan. They found that the heat transfer augmentation of the piezoelectric fan came from the entrained airflow during each oscillation cycle and the jet-like air stream at the fan tip. The heat transfer performance for the vertical arrangement showed a symmetrical distribution and peaked at the center region, whereas the horizontal arrangement possessed an asymmetrical distribution and showed an early peak. The heat transfer performance for the horizontal arrangement was not necessarily lower than that of the vertical arrangement. Kimber et al. [15] experimentally determined the relationship between the pressure and flow rate generated by miniature piezoelectric fans. They considered the proximity of surrounding walls with the use of three different enclosures. The aerodynamic interactions between two vibrating fans were explored by Kimber et al. [16]. They found that damping is significantly influenced by the proximity of neighboring piezoelectric fans and by vibration phase difference. A comparative investigation between 2D numerical flow simulations and experimental data on particle image velocimetry was conducted by Choi et al. [17,18]. They observed the vortex formation and unsteady flow fields around single and dual vibrating fans in free stream. Lin [19,20] recently analyzed 3D heat and fluid flow induced by a single piezoelectric fan on flat and cylindrical heat surfaces. His experimental and numerical results indicated that the piezoelectric fan improved the heat transfer coefficient by 1.2 to 2.4 times. Abdullah et al. [21] reported an orientation of multiple piezoelectric fans (set in edge-to-edge arrangement) to enhance the heat transfer of finned heat sink in microelectronic cooling with 3D numerical simulation. Their results showed that an enhancement in convective heat transfer coefficient exceeding 88% may be achieved compared with natural convection.

In the literature, the thermal and flow behavior of single vibrating fans has been extensively studied. By contrast, characterizations on the thermal performance of dual piezoelectric fans, which have important practical applications, have not been sufficiently explored. Only Kimber and Garimella [10] experimentally investigated the thermal performance of dual vibrating fans in consideration of an identical vibration phase angle. Ihara and Watanabe's [5] experiments on the visualization of the flow field around dual vibrating fans established that the vibration phase angle significantly affected the flow field. However, further characteristics need to be determined to assess the influence of different phase angles between dual vibrating fans on the resulting heat transfer. Discussions are also lacking in the literature on the complexity of mechanisms such as dual fans with varying vibration phase angles. Therefore, this study explores experimental and numerical analyses on the flow and thermal performance of dual vibrating fans that are arranged face to face with different vibration phases. Two vibrometers (laser displacement sensors KEYENCE LK-G152) are employed to detect the phase angle and measure the vibration amplitude for each fan individually. 3D simulations based on a dynamic meshing scheme are performed in FLUENT and ABAQUS with the use of code coupling interface MpCCI to investigate transient changes on the temperature and flow fields achieved by dual vibrating fans with in-phase ($\Phi = 0°$) and out-of-phase ($\Phi = 180°$) vibration. The thermal performance of the dual fans is compared relative to the single fan, and the estimated results are also compared with experimental findings.

2. Experimental setup and procedure

A dual commercial piezoelectric fan consisting of a bimorph lead zirconate titanate patch bonded to a thin stainless steel blade was used in this study. The fan has high elongation properties at a relatively low power input (Table 1). The fans were arranged face to face with a spacing of 25 mm and were vertically oriented to the heated surface. Each fan was rigidly held by an adjustable stand to vary the tip gap. Two vibrometers (laser displacement sensors KEYENCE LK-G152) were set oppositely and positioned near the fans' tip to measure the vibration amplitude for each fan individually. The measurement points of the focal laser beam to the fan surfaces were (1 mm) from the fan tip. The error of the displacement sensor was −/+ 0.02%. Slightly different resonance frequencies existed between the fans because of discrepancy in manufacturing, which would occur as phase differences between their motions. Therefore, one of the main challenges in these

Table 1
Specifications of the piezoelectric fan (Piezo Systems Inc., USA).

Specification	Value
Material	Stainless steel
Size (mm)	47 (l_{pf}) × 12 (D_{pf}) × 0.4 (t_{pf})
Length without patch (mm)	23 (l_u)
Resonance frequency (Hz)	110
Power consumption (mW)	42
Weight (kg)	0.002

measurements was tuning the movement of the fans in terms of in-phase and out-of-phase as perfectly as possible. Fig. 1 shows the different vibration phases between dual vibrating fans. The fans that vibrate in the same direction are defined as in-phase, whereas the fans that vibrate opposite the other are defined as out-of-phase. The output signal of the vibration phase angles between the fans was detected by the vibrometers. The input signal of the fans was carefully monitored with two-channel digital storage (DSO3062A oscilloscope) connected with two inverter drive circuits. These circuits independently tune the frequencies for each fan. Each inverter circuit was also joined with an input channel provided by a direct current (DC) dual power supply (GW Instek GPS2303) to obtain the voltages required for fan operation. These inverter circuits were used to convert DC to alternating current to drive the fans. The frequency was adjusted by turning the trimmer pot on the printed circuit board of each circuit. Both fans were driven at their approximate resonance frequencies, with a fixed input of 42 mW for each. During the fans' operation, the IMC DAQ system recorded the output fans' displacement and frequencies from both sensor, as well as inputted the information into the computer.

The microelectronic component was simulated by an aluminum foil (size 82 mm×60 mm×0.8 mm) heated with a uniform heat flux of 1350 W/m^2 by means of a stainless steel electrical heater attached beneath the foil. A heat sink compound RS® of high conductivity was used to paste the heater with the foil. The foil-heater assembly was fixed into the cavity of a wooden platform so that their top surfaces were coplanar. Six thermocouples (K-type, TTK-36-SLE) were attached on the outer surface of the plate to determine the average surface temperature, and one thermocouple was used to measure the ambient temperature. All thermocouples were linked to a desktop PC that utilized a data acquisition system (Advantech USB-4718, eight-channel). The temperatures were recorded every 60 s, and the ambient temperature was always monitored to be 22 °C. Figs. 2 and 3 show that the assembly of the microelectronic component and the piezoelectric fans were housed into a glass tunnel to reduce ambient effects. With the objective of maximizing heat dissipation, two essential parameters were investigated: the vibration phase of two vibrating fans and the separated distance between the fan tip and the heated surface.

The rate of heat flux (q'') generated by the heat source could be computed according to the following equation:

$$q'' = \frac{Q}{A_{mc}} \tag{1}$$

where (Q°) and (A_{mc}) are the power input (6.66 W) and surface area of the microelectronic component, respectively.

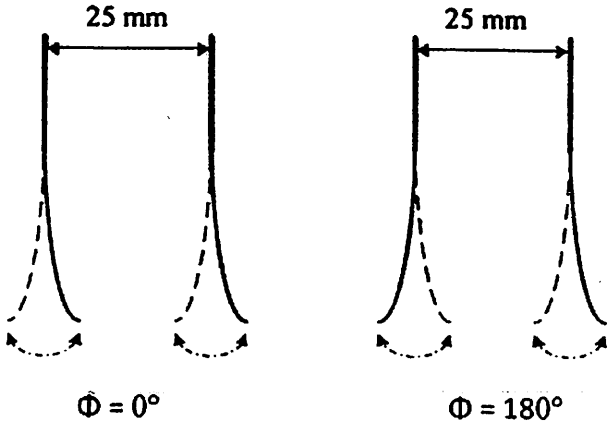

Fig. 1. Definition of the vibrating phase angles between two piezoelectric fans, in-phase vibration (Φ = 0°) and out-of-phase vibration (Φ = 180°).

The average heat transfer coefficient ($\bar{h}$) was defined based on the difference between the average temperature of the heated surface and the ambient temperature over the heated surface:

$$\bar{h} = \frac{q''}{(\bar{T}_s - T_a)} \tag{2}$$

where ($\bar{T}_s$) is the average temperature of the aluminum plate surface, and (T_a) is the ambient temperature.

To assess the importance of the cooling result achieved by the piezoelectric fan, the enhancement ratio (ξ) [14] that represented the convection during fan operation was divided by that under natural convection:

$$\xi = \bar{h}_{pf}/\bar{h}_n \tag{3}$$

where $\bar{h}_{pf}$ is the average heat transfer coefficient achieved under force convection (ON piezoelectric fans), and $\bar{h}_n$ is the average heat transfer coefficient achieved under natural convection condition, which was about 22 W/K m^2 (OFF piezoelectric fans).

3. Computational methods and boundary conditions

In the computational method, coupling code (MpCCI 3.1) was used to couple finite volume method (FVM)- and FEM-based software in the fluid and heat transfer analyses. Therefore, the transformation of analysis generated from the FEM code (ABAQUS 6.9) to the FVM code (FLUENT 6.3.26) was conducted with MpCCI 3.1. Real-time data were transferred from each code to the other. The forces induced from the solid acting on the fluid were directly solved by FLUENT. The deformations of the fluid domain were thus simultaneously calculated. The piezoelectric fans (beams 1 and 2) were defined as the coupled regions. However, ABAQUS as a solid solver was employed to impose the movement of the vibrating beams into the fluid domain. FLUENT was used to solve the fluid flow field around the beams and to simulate the heat rate of the microelectronic device.

The first-order upwind discretization scheme was used in FVM for momentum and energy equations, with the SIMPLE scheme utilized for pressure–velocity coupling. The y^+ value was set as 1 in treating turbulent flow at the near-wall region (heat source surface). Shear stress transport (SST) k-ω model was used to describe the flow induced by the vibrating fan, which has local turbulence. A uniform heat flux was applied on the heated surface according to the experimental setup, whereas the surrounded area (wooden platform) at the bottom boundary was insulated at wall $q = 0$ under no-slip condition. The top and four side boundaries of the computational domain were treated as pressure boundaries. The beams were defined as coupling surface boundaries. The dynamic mesh option was activated in FLUENT during the calculations. A time step size of 0.0001 s was chosen for all cases, with 100 time steps per cycle of fan vibration. The total duration of the simulation was selected, such that the temperature reached a steady value during this period. A total of 10,000 iterations were reached, which correspond to approximately five days of computation time per case on a Pentium Dual Core processor (2.8 GHz) computer with 2.0 GB memory.

The deformable structure for FEM includes the geometrical entities of the vibrating beam and the beam's corresponding mechanical properties. The components were modeled as homogeneous materials with isotropic material behavior, constant densities, and linear Young's modulus. To implement the beam motion in the structural model, dynamic implicit functions were applied. The beam was assumed to vibrate at a frequency of 100 Hz; this round off compared with the experimental value of 109 Hz was made to achieve numerical stability. The exact values of the beam vibration amplitudes A_{pf} were considered in performing the simulation according to experimental measurements.

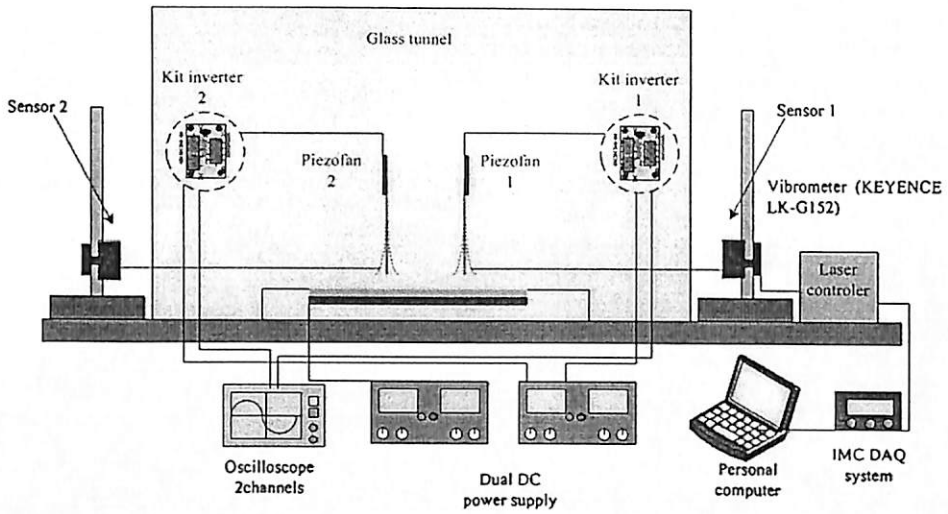

Fig. 2. Schematic of experimental setup for dual piezoelectric fans.

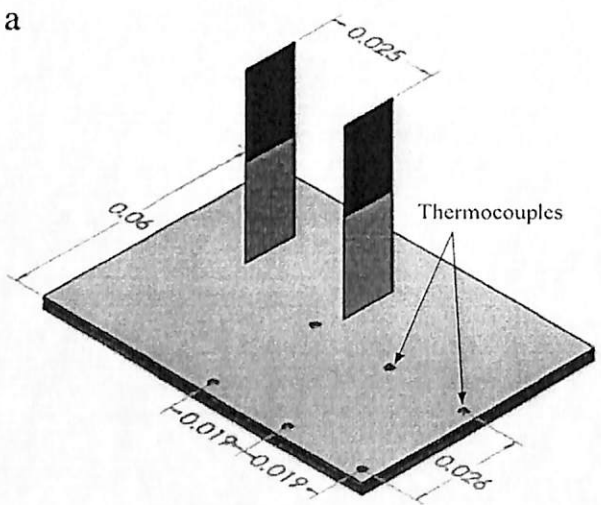

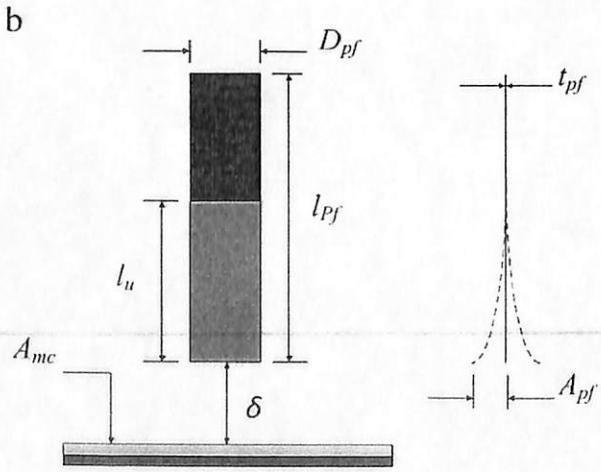

Fig. 3. Details of the experimental setup inside the glass tunnel showing (a) thermocouples positioned onto the heated surface and (b) various geometric parameters of piezoelectric fan.

4. Geometrical modeling and grid generation

Two types of 3D models were created for coupling purpose: (a) modeling of the fluid domain surrounding the heat surface and (b) modeling of the deformable beams, dimensions of the heated surface, calculation domain, and spacing between the vibrating fans (Fig. 4).

For the fluid domain, the surface and volume meshes were generated with GAMBIT 2.3.16 and exported to FLUENT 6.3.26 for analysis. The heated surface area of the microelectronic component was similar to that used in the experiment, and the clamp of the piezoelectric fan was neglected. Fig. 5(a) shows that a combination of tetrahedral and quad literal element grids was employed and interfaced into the fluid domain. The unstructured mesh of tetrahedral elements was clustered around beam surfaces to avoid damaged fluid cells. The fluid cells can be highly skewed because of beam movement [21]. A structured mesh of quadrilateral elements was required at the vicinity of the heated surface to treat turbulent flow at the near-wall region, and the y+ value was set to 1. Therefore, the fluid domains were meshed between 400,000 and 470,000 cells for different cases according to the spacing between the beams and the heated surface. The spacing from the fan tip to the heated surface was varied from 1.2 mm to 30 mm. Thus, (δ) is the ratio of the fan tip spacing to

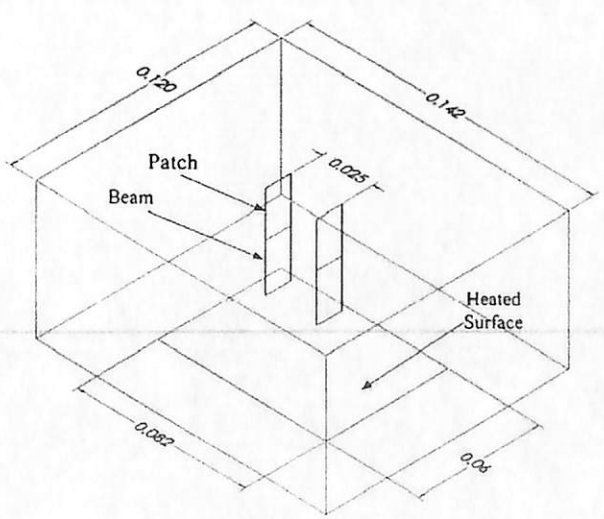

Fig. 4. Illustration of the computational domain.

the fan width (D_{pf}) ranging from 0.1 to 2.5. However, the deformable structures were created and meshed with FEM-based software (ABAQUS) according to the beam dimensions. The rigid beams were suspended in vertical ordination. Fig. 5(b) shows that the hexahedral is applied to generate the mesh of the structure's 380 elements for each beam. The surfaces on which pressures and displacements are coupled must be perfectly identical for the interfacing approach to perform the coupling solution.

4.1. Governing equations

The numerical solution coupled two separated numerical models with two topological surfaces, flow, and structural solvers. The coupling process for the numerical simulation requires the equation for mass and momentum in arbitrary Lagrangian–Eularian formulation. The conservation of mass and momentum equations of the continuum mechanic formulation for an incompressible medium are expressed as follows:

$$\nabla\cdot\left(\vec{u}-\vec{u}_g\right)=0 \tag{4}$$

$$\rho\cdot\left[\frac{\partial\vec{u}}{\partial t}+\left(\left(\vec{u}-\vec{u}_g\right)\cdot\nabla\right)\cdot\vec{u}\right]=\nabla\sigma+\vec{f} \tag{5}$$

where ρ is the density, $\vec{u}$ is the velocity vector, $\vec{u}_g$ is the local grid velocity, σ is the Cauchy stress tensor, and $\vec{f}$ is the volume force.

The kinematic and dynamic coupling conditions (i.e., corresponding to local normalized vector $\vec{n}$) for the data exchange via the topologically identical surface of the two computational domains must be identical. Thus, the equations are expressed as follows:

$$\vec{x}_{fluid}=\vec{x}_{solid} \tag{6}$$

$$\vec{u}_{fluid}=\vec{u}_{solid} \tag{7}$$

$$\vec{\sigma}_{fluid}=\vec{\sigma}_{solid} \tag{8}$$

where $\vec{x}$ is a position vector.

The governing equations employed in FLUENT to describe transient fluid flow are as follows:

Continuity:

$$\frac{\partial\rho}{\partial t}+\frac{\partial}{\partial x_i}(\rho u_i)=0 \tag{9}$$

Momentum (non-accelerating reference frame):

$$\frac{\partial}{\partial t}(\rho u_i)+\frac{\partial}{\partial x_j}\left(\rho u_i u_j\right)=-\frac{\partial P}{\partial x_j}+\frac{\partial\tau_{ij}}{\partial x_j}+\rho g_i+F_i \tag{10}$$

where ρ is the fluid density, P is the pressure in the fluid, τ_{ij} is the viscous stress tensor, and g_i and F_i are the gravitational acceleration and external body force in the i-direction, respectively.

Energy:

$$\frac{\partial}{\partial t}\left(\rho c_p T\right)+\frac{\partial}{\partial x_j}\left(\rho u_i u c_p T\right)=k\frac{\partial^2 T}{\partial x_j^2} \tag{11}$$

where c_p is the specific heat of air, T is the temperature, and k is the thermal conductivity.

5. Results and discussion

The results of this study aim to highlight two different aspects related to vibrating fans. The first aspect compares the cooling performance between single and dual vibration fans. The second aspect characterizes the vibration phase between these dual fans to assess their influence on the resulting heat transfer.

5.1. Flow interaction

The characterizations of the vibration phase differences between dual vibrating fans are presented based on (vibrometer) measurements. Fig. 6 illustrates the amplitude A_{pf} histories when the two fans begin to show the coupling interaction under in-phase and out-of-phase vibrations. Laser sensors (vibrometers) were positioned opposite each other to capture each fan tip deflection independently and to distinguish the oscillatory behavior of these fans (oscillators) synchronously. The oscillator history plot shows the traveling wave of each fan in the opposite direction with the other (traveling wave phase angle $=180°$) while both fan motions are in in-phase vibration (vibration phase angle $\Phi=0°$). Meanwhile, both traveling waves of the fans are in one direction (traveling wave phase angle $=0°$) while the fans are in out-of-phase vibration (vibration phase angle $\Phi=180°$). All experiments were conducted with a fixed input driving power (42 mW) for each fan. Every fan has its own particular fundamental resonance frequency, which is experimentally detected to be 109.64 and 110.80 Hz for fans 1 and 2, respectively. In both vibration phases, the amplitude of fan 1 is slightly larger than that of fan 2 because the latter is forcibly tuned with fan 1 according to the running vibration phases. The largest amplitudes are detected at $\Phi=0°$, which are attributed to the reduction viscous drag and which could

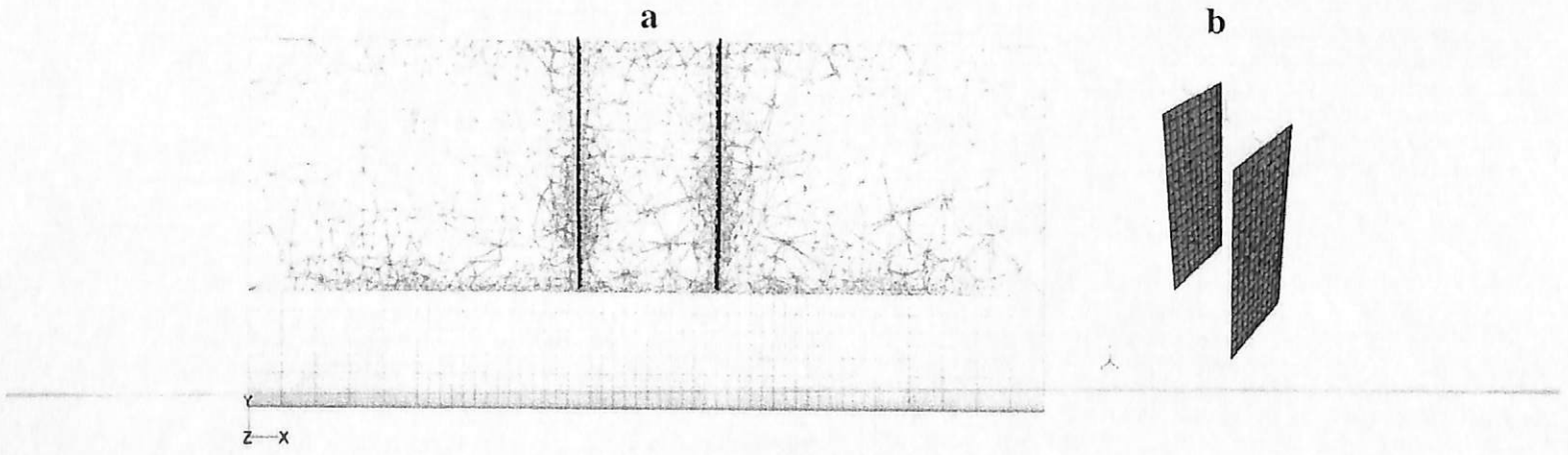

Fig. 5. The meshed model (a) fluid domain and (b) deformable beams.

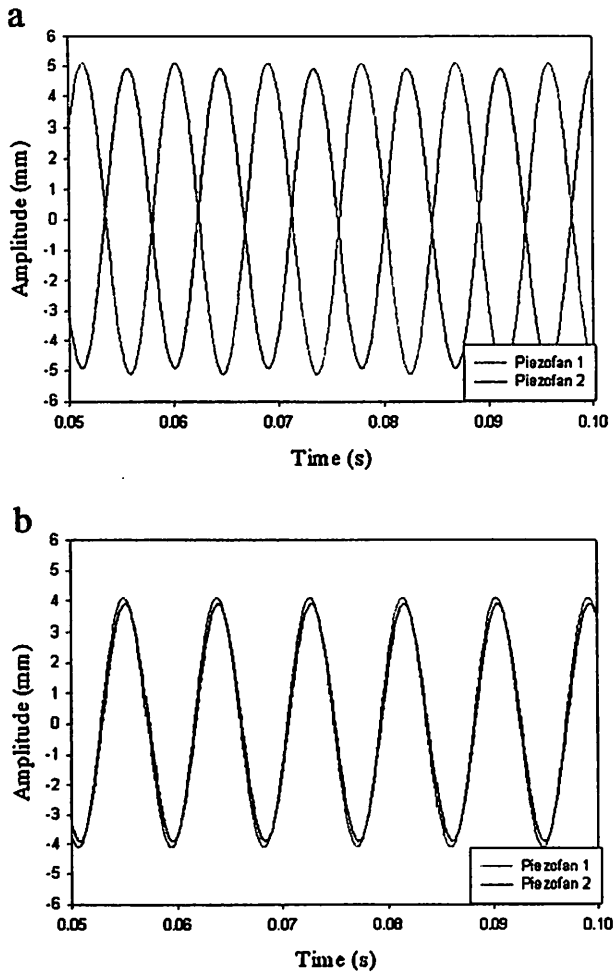

Fig. 6. Difference of vibration phase between two piezoelectric fans set in face to face arrangement (a) In-phase vibration $\Phi = 0°$. $= 180°$ and (b) out-of-phase vibration $\Phi = 180°$. $= 0°$.

further increase vibration amplitudes; the smallest amplitudes are detected at $\Phi = 180°$. Any two fans cannot have identical resonance frequencies because of inescapable variations during manufacturing processes. The discrepancies between the two fans could induce the interference yield to exchange the vibration phases approximately every 2 s during the fans' operation even with identical input signals. Therefore, in-phase (or out-of-phase) vibration cannot remain for long under in-phase (neither out-of-phase) vibration condition. As a result, numerical method is adopted to estimate the effect of vibration phase differences between the two fans on thermal performance.

5.2. Flow field

The flow field induced by a dual vibrating fan is naturally unsteady, and the flow mechanisms involved are quite complex. For such a complex flow, the numerical solution offers a practical approach to achieve accurate analysis, which clarifies the flow interaction between the two fans. Fig. 7 shows the velocity contours on the heated surface and the development of flow field induced by a dual vibrating fan at the middle plane of the fluid domain ($z = 0$ mm). The velocity vectors with streamlines at three different instant positions are shown; these positions correspond to a half cycle of the fans' motion for $\Phi = 0°$ and $\Phi = 180°$.

For $\Phi = 0°$, the parallel fans simultaneously move ahead from their natural position to the maximum deflection in the positive x-direction (Fig. 7a) as a newly clockwise (CW) vortex is formed aft each fan tip at the exact time. A counterclockwise (CCW) vortex is seen at the right side. The trajectory of these CW vortices frequently follows the parallel fans and moves toward one direction near the adjacent surface (heat source). As the fans return to their natural position (Fig. 7b), a new CCW vortex is formed, and the vortices follow the fans to the maximum deflection in the negative x-direction (Fig. 8c). Only one vortex is observed between the inner fans' surfaces. The vortices at the outer fans' surfaces formed during the previous period still exist before propagation. The two fans vibrate synchronously, so no flow separation exited between them. This flow separation could create a net flow between the fans, which increases the vibration amplitudes.

For $\Phi = 180°$, the fans move away from each other from their natural positions to the maximum deflection in the positive (fan 1) and negative (fan 2) x-directions (Fig. 7$\bar{a}$) as CW and CCW vortices are formed between the inner fans' surfaces. The flow between these fans appeared to be isolated along the y-direction at $x = 0$. Two counter vortices are seen at the inner fans' surfaces. However, a separation flow within the fluid domain is also observed, which is expected to influence heat convection negatively. When the two fans move toward each other (Fig. 7$\bar{b}$), a CCW vortex forms on the outer surface of fan 1, and a CW vortex forms on the outer surface of fan 2. These vortices follow the fans until their maximum deflections to the inner area are reached (Fig. 7$\bar{c}$). The vortices at the inner surfaces are propagated. Unlike the vortices formed at $\Phi = 0°$, the trajectory of these vortices also follows the motion of the fans, but the cross flow trajectory could not exceed the centerline ($x = 0$). Reverse flow results, which is also undesirable for heat convection. Therefore, the fans push the flow to the center when these fans become close to each other, and damping results. When the fans move away from each other, the flow is entrained from the center to the left and right sides. Drag results, which decreases the vibration amplitudes. The spread flow stream area over the heated surface for $\Phi = 0°$ is relatively larger than that for $\Phi = 180°$. This result is attributed to the constructive interference at $\Phi = 0°$, whereas $\Phi = 180°$ causes destructive interference within the fluid domain. Therefore, a high magnitude of velocity is found at $\Phi = 0°$. However, the fans' motion at $\Phi = 0°$ could systematically displace the flow at the adjacent surface in both x-directions without flow separation. This phenomenon is expected to enhance heat convection.

5.3. Thermal analysis

Fig. 8 shows the temperature contours under force convection with characterizations of the nine cases. The first column illustrates in-phase vibration ($\Phi = 0°$), the second column illustrates the out-of phase vibration ($\Phi = 180°$) of dual fans, and the last column illustrates the single fan. The single fan is qualitatively and quantitatively compared with the different cases. For each column, the results are shown at three different tip gap δ values of 0.1, 0.83, and 1.66. The heated surface (82 mm × 60 mm) shows a significant change in temperature distribution. For the single fan, a droplet cooling zone is formed as a lobed pattern and is observed at the heated surface center, whereas the fan is directed. These lobes, which appear symmetric in the X and Z directions, indicate that the flow induced by the fan is evenly separated; the flow could only be obtained with vertical fan orientation. The tip gap is minimal ($\delta = 0.1$), so the contour shows a semi-circular or rounded square shape with a high temperature drop. The contours show lateral widening to an elliptical shape at $\delta = 0.83$ and 1.66 with a low drop of temperature. This result indicates that the flow stream released from the fan to strike the heated surface could be more efficient as the fan becomes closer to the heated surface. The third column contours of the asymmetric lobes at the heated surface are very close to those presented by Kimber et al. in their heat thermal imaging experiments for a single vibrating fan [9]. The first and second columns in Fig. 8 show six cases with dual vibrating fans, and each column represents a different vibration phase. The contours of the smallest gap ($\delta = 0.1$) for both vibration phases demonstrate two lobed patterns shaped with two separated fans at the heated surface. Each appears to be

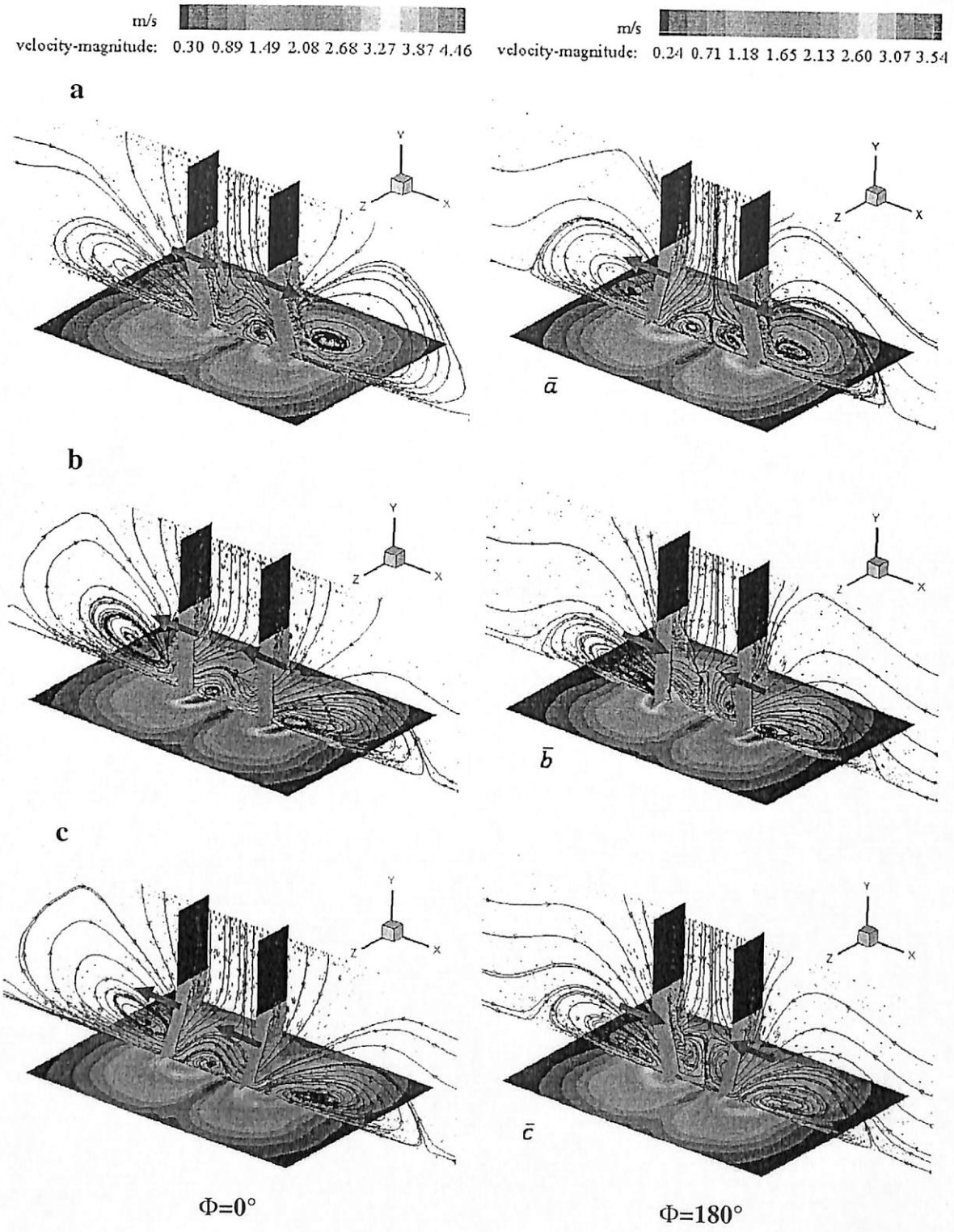

Fig. 7. Flow field induced with dual vibrating fan.

similar to that formed by a single fan. The difference is the lower magnitude of the temperature for these cases compared with their corresponding single-fan case. Larger lobes of $\Phi = 0°$ are observed as the cooling zone between them is enhanced, whereas the lobes of $\Phi = 180°$ are smaller than those of $\Phi = 0°$. The semi-isolated zone between these lobes is also observed. Furthermore, the temperature magnitude is higher than the $\Phi = 0°$ case. This result is attributed to the fan amplitude increase for $\Phi = 0°$, which results in flow acceleration and cooling enhancement. The opposite is true for $\Phi = 180°$ as explained earlier. As the gap δ increases, a higher temperature magnitude and transitions are noted from a circular pattern at $\delta = 0.1$ to an elliptical pattern at $\delta = 0.83$ and 1.66 for both vibration phases. The elliptical lobes of $\Phi = 0°$

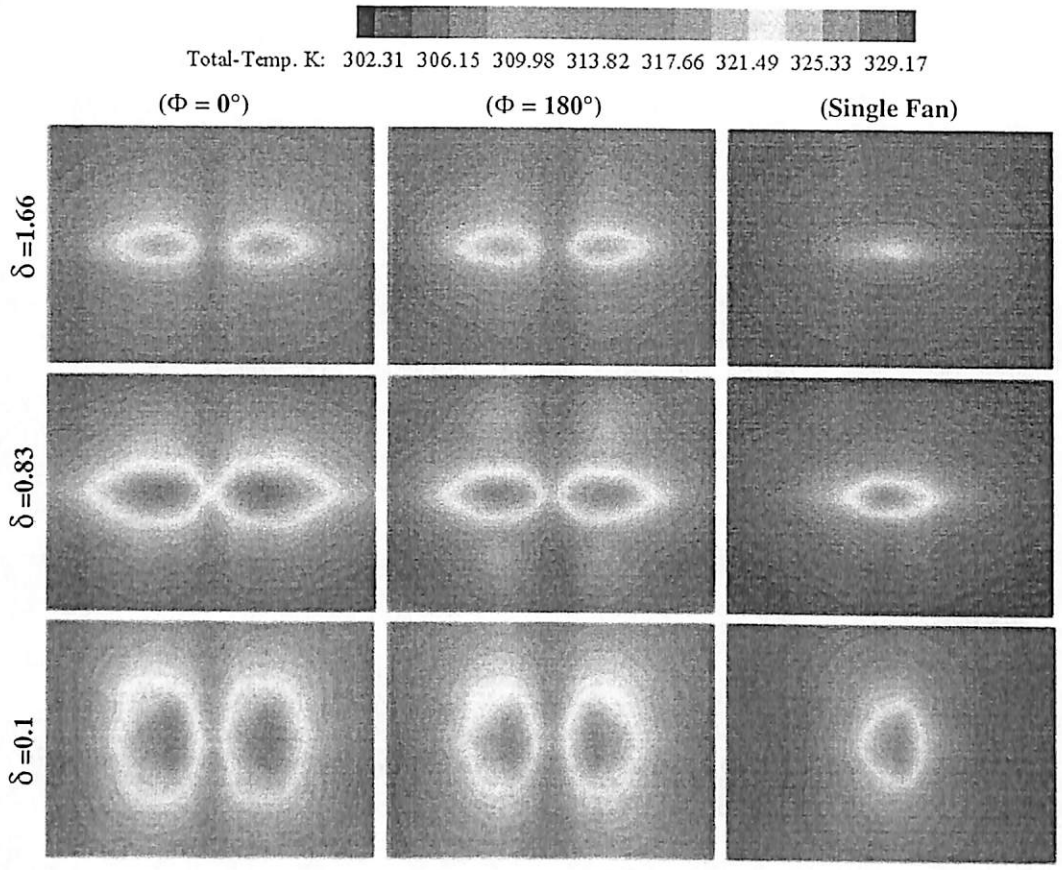

Fig. 8. Temperature contours under force convection for dual vibrating fans with in-phase vibration ($\Phi = 0°$) first column, out-of-phase vibration ($\Phi = 180°$) second column, and the last column for single vibrating fan. Each column represents a different tip gap corresponding to $\delta = 0.1$, 0.83, and 1.6. The heated surface shown is 82 mm × 60 mm.

are larger than those of $\Phi = 180°$ with the enhancement of the cooling zone between them. The middle zone between these lobes of $\Phi = 180°$ shows an isolated zone with a high temperature magnitude. For $\Phi = 0°$, the temperature reductions are noticeable compared with $\Phi = 180°$ of dual fans for the same gap. Therefore, the adverse influence of cooling is observed for $\Phi = 180°$, which is attributed to the destructive interference within the fluid domain. This finding is consistent with those in references [5,10], in which constructive interference was observed under certain conditions for dual fans vibrating in-phase. The general map of temperature shows that dual fans improve cooling performance regardless of the vibration phase compared with a single fan.

Fig. 9 shows variations in the computed and measured average heat transfer coefficients achieved under force convection on the heated surface with dimensionless fan tip gap δ. The heat transfer experiments indicate that the steady state under force convection (ON piezoelectric fans) could be achieved at least after 30 min for a certain case. Meanwhile, the vibration phase is periodically changed approximately every 2 s during the fans' operation because of the discrepancy of natural frequencies between these two fans. Therefore, the heat transfer rate does not achieve steady state solely within in-phase (or out-of-phase). In the heat transfer measurements, the average of both vibration phases is considered under quasi-steady state to justify the numerical solution. In the simulation, the fans' amplitudes A_{pf} were set exactly according to vibrometer measurements to allow reliable prediction. However, the overall magnitude of h_{ave} increases with a decrease in δ, which indicates that the cooling performance is high for minimal gaps. This outcome is expected because the flow velocity at the vicinity of the heated surface decreases with an increase in separation distance and thus results in a low convective heat transfer coefficient. Regardless of the vibration phase, the heat transferred achieved with a dual vibrating fan is significantly higher than that achieved with a single fan. The influence of dual fans actuated at $\Phi = 0°$ accordingly results in large amplitudes and yields flow acceleration. The fluid is forced to displace rapidly in both directions (negative and positive X-axis). Therefore, the higher velocity zone is mostly localized in the vicinity of the heated surface, and this localization enables effective heat removal. Therefore, maximum heat transfer is observed at $\Phi = 0°$. An almost adverse behavior for $\Phi = 180°$ is noted; the influence of dual fans vibrating against each other at $\Phi = 180°$ results in relatively smaller amplitudes that yield flow deceleration and lower heat transfer. The influence of vibration phase decreases with an increase in δ, and the maximum difference

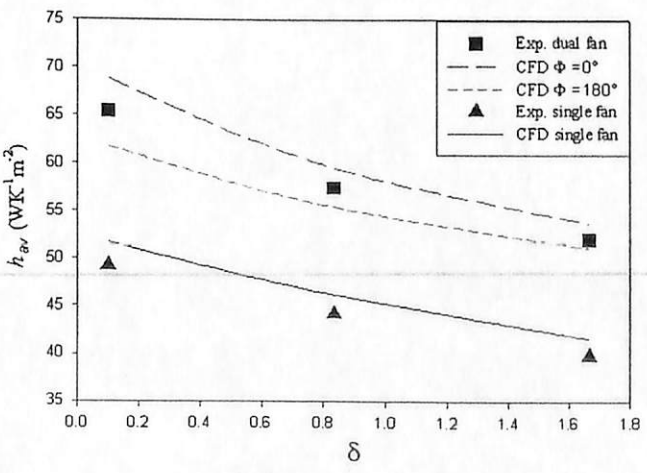

Fig. 9. Average of heat transfer coefficient.

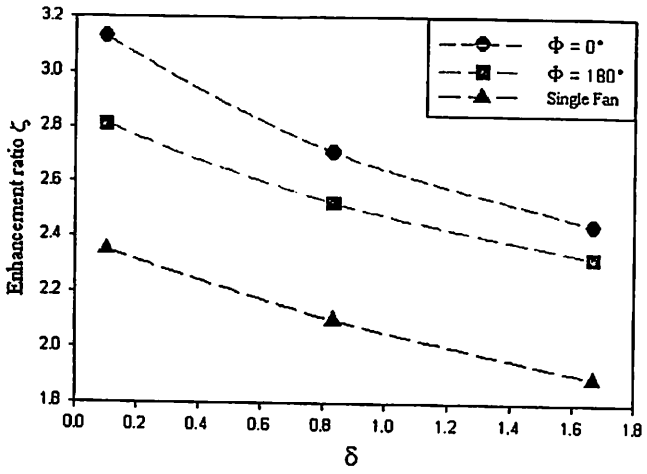

Fig. 10. Enhancement ratio.

between the vibration phases of the computed average heat transfer is 12.3% at $\delta = 0.1$. The computed heat transfer for $\Phi = 0°$ is higher than that determined from the experimental measurement. For $\Phi = 180°$, the computed heat transfer is low because the vibration phases of the fans' motion are accurately monitored in simulations. The combined performance of dual fans and the improvement relative to a single fan were observed. The results show a good general agreement of the estimated and measured results. Fig. 10 depicts the heat transfer enhancement ratio of the single and dual fans for three different fan tip distances to the heated surface. In each case, the enhancement ratio decreases as the separation distance between the fan tip and the heated surface increases. The single fan enhances heat transfer performance within approximately 1.9 to 2.3 times for the heated surface, whereas the dual fans enhance heat transfer performance within approximately 2.3 to 2.9 for out-of-phase vibration ($\Phi = 180°$) and 2.4 to 3.1 for in-phase vibration ($\Phi = 0°$). These findings indicate that adding a second fan significantly affects effective heat removal and is an important factor to be considered in the actual implementation of these dual fans.

6. Conclusion

The characterizations of the average heat transfer coefficient for single and dual vibrating fans have been experimentally investigated, followed by numerical analysis. With the objective to maximize heat dissipation, the interactions between the dual fans for in-phase ($\Phi = 0°$) and out-of-phase ($\Phi = 180°$) vibrations are explored. Varying separation distance between the fans and the heated surface is conducted in the range of $\delta = 0.1$, 0.83, and 1.66. 3D coupling based on a dynamic meshing scheme is conducted with FLUENT and ABAQUS with the use of code coupling interface MpCCI to examine the flow field and the resulting heat transfer. The thermal performance of the dual fans is compared with that achieved with the single fan. The estimated results are compared with experimental findings to substantiate the numerical solution. However, the maximum heat transfer rate is observed at in-phase vibration ($\Phi = 0°$). The influence of vibration phase decreases with an increase in δ, and the maximum difference between the vibration phases of the computed heat transfer is 12.3% at $\delta = 0.1$. The single fan enhances heat transfer performance within approximately 2.3 times for the heated surface. By contrast, the dual fans enhance heat transfer performance within approximately 2.9 for out-of-phase vibration ($\Phi = 180°$) and 3.1 for in-phase vibration ($\Phi = 0°$).

Acknowledgement

The authors would like to thank the Universiti Sains Malaysia for the financial support through RU grant number 1001/PMEKANIK/814163.

References

[1] M. Toda, Theory of air flow generation by a resonant type PVF2 bimorph cantilever vibrator, Ferroelectrics 22 (1979) 911–918.
[2] M. Toda, Voltage-induced large amplitude bending device PVF2 bimorph its properties and applications, Ferroelectrics 32 (127–133) (1981).
[3] R.R. Schmidt, Local and average transfer coefficients on a vertical surface due to convection from a piezoelectric fan, Thermal Phenomena in Electronic Systems, 1994, I-THERM IV. 'Concurrent Engineering and Thermal Phenomena', InterSociety Conference on, 1994, pp. 41–49.
[4] T. Açlkalin, S.M. Wait, S.V. Garimella, A. Raman, Experimental investigation of the thermal performance of piezoelectric fans, Heat Transfer Engineering 25 (1) (2004) 4–14.
[5] A. Ihara, H. Watanabe, On the flow around flexible plates, oscillating with large amplitude, Journal of Fluids and Structures 8 (7) (1994) 601–619.
[6] P.I. Po, L. Byoung-Gook, Feasibility of using ultrasonic flexural waves as a cooling mechanism, IEEE Transactions on Industrial Electronics 48 (1) (2001) 143–150.
[7] T. Acikalin, A. Raman, S.V. Garimella, Two-dimensional streaming flows induced by resonating, thin beams, The Journal of the Acoustical Society of America 114 (4) (2003) 1785–1795.
[8] M. Kimber, S.V. Garimella, A. Raman, Local heat transfer coefficients induced by piezoelectrically actuated vibrating cantilevers, Journal of Heat Transfer 129 (9) (2007) 1168–1176.
[9] M. Kimber, S.V. Garimella, Measurement and prediction of the cooling characteristics of a generalized vibrating piezoelectric fan, International Journal of Heat and Mass Transfer 52 (19–20) (2009) 4470–4478.
[10] M. Kimber, S.V. Garimella, Cooling performance of arrays of vibrating cantilevers, Journal of Heat Transfer 131 (11) (2009) 111401.
[11] T. Açıkalın, S.V. Garimella, A. Raman, J. Petroski, Characterization and optimization of the thermal performance of miniature piezoelectric fans, International Journal of Heat and Fluid Flow 28 (4) (2007) 806–820.
[12] M.K. Abdullah, M.Z. Abdullah, M.V. Ramana, C.Y. Khor, K.A. Ahmad, M.A. Mujeebu, Y. Ooi, Z. Mohd Ripin, Numerical and experimental investigations on effect of fan height on the performance of piezoelectric fan in microelectronic cooling, International Communications in Heat and Mass Transfer 36 (1) (2009) 51–58.
[13] L.A. Florio, A. Harnoy, Use of a vibrating plate to enhance natural convection cooling of a discrete heat source in a vertical channel, Applied Thermal Engineering 27 (13) (2007) 2276–2293.
[14] S.-F. Liu, R.-T. Huang, W.-J. Sheu, C.-C. Wang, Heat transfer by a piezoelectric fan on a flat surface subject to the influence of horizontal/vertical arrangement, International Journal of Heat and Mass Transfer 52 (11–12) (2009) 2565–2570.
[15] M. Kimber, K. Suzuki, N. Kitsunai, K. Seki, S.V. Garimella, Pressure and flow rate performance of piezoelectric fans, IEEE Transactions on Components and Packaging Technologies 32 (4) (2009) 766–775.
[16] M. Kimber, R. Lonergan, S.V. Garimella, Experimental study of aerodynamic damping in arrays of vibrating cantilevers, Journal of Fluids and Structures 25 (8) (2009) 1334–1347.
[17] M. Choi, C. Cierpka, Y.H. Kim, Vortex formation by a vibrating cantilever, Journal of Fluids and Structures 31 (2012) 67–78.
[18] M. Choi, S.-Y. Lee, Y.-H. Kim, On the flow around a vibrating cantilever pair with different phase angles, European Journal of Mechanics - B/Fluids 34 (2012) 146–157.
[19] C.-N. Lin, Analysis of three-dimensional heat and fluid flow induced by piezoelectric fan, International Journal of Heat and Mass Transfer 55 (11–12) (2012) 3043–3053.
[20] C.-N. Lin, Heat transfer enhancement analysis of a cylindrical surface by a piezoelectric fan, Applied Thermal Engineering 50 (1) (2013) 693–703.
[21] M.K. Abdullah, N.C. Ismail, M. Abdul Mujeebu, M.Z. Abdullah, K.A. Ahmad, M. Husaini, M.N.A. Hamid, Optimum tip gap and orientation of multi-piezofan for heat transfer enhancement of finned heat sink in microelectronic cooling, International Journal of Heat and Mass Transfer 55 (21–22) (2012) 5514–5525.

International Communications in Heat and Mass Transfer 52 (2014) 140–151

Contents lists available at ScienceDirect

International Communications in Heat and Mass Transfer

journal homepage: www.elsevier.com/locate/ichmt

Effect of piezoelectric fan mode shape on the heat transfer characteristics ☆

Z.M. Fairuz *, S.F. Sufian, M.Z. Abdullah, M. Zubair, M.S. Abdul Aziz

Aerodynamic and Advanced Cooling Laboratory, School of Mechanical and Aerospace Engineering, Engineering Campus, Universiti Sains Malaysia, 14300 Nibong Tebal, Penang, Malaysia

ARTICLE INFO

Available online 4 December 2013

Keywords:
Electronic cooling
Piezoelectric fan
Heat transfer enhancement
Vortex
Mode shape

ABSTRACT

Piezoelectric fans with their low noise and power consumption, are an effective means of enhancing heat transfer and is a viable alternative to the natural convection process. Several studies have been extensively carried out at the fundamental resonance mode. In this work, three-dimensional numerical studies on the effect of first, second and third mode shapes driven at frequency and the tip amplitude of the first mode are accomplished to investigate their effects on the heat transfer characteristics. The experimental and numerical model of the first mode shows a reasonably good agreement between them. The results showed that the increase in the mode number decreased the induced air flow velocity on the top of the heated surface, thus impeding the cooling capabilities at higher mode number. The vibrating blade of the first mode produced a pair of asymmetric vortex of opposite circulation around front and the back the piezofan tip, which disappear with the increase of mode number. It is thus established from this work that higher mode of vibrations is ineffective and therefore the fundamental resonance mode is suggested for all practical piezofan applications.

1. Introduction

Recent advances in the field of electronics have maximized the density integration, clock rates, and miniaturization of modern electronics. This has tremendously increased the dissipation of heat flux, which might in turn cause thermal failures such as mechanical stresses, thermal debonding and thermal fracture. Therefore, it is of significant importance for any electronic engineer to manage temperature and its adverse effects on electronic packages to ensure optimal performance and reliability.

Piezoelectric fans can be used to generate airflow for cooling microelectronic devices. Their outstanding features include noise-free operation, low power consumption and suitability for confined spaces which make them easy replacement to the conventional rotary fan. It consists of a thin flexible cantilever blade bonded with a piezoelectric patch near its base end. When an alternating input signal is applied to the piezoelectric material it contracts and expands periodically in the lengthwise direction at the frequency of the input voltage. This causes bending moment at the beginning and end of the patch, which can be effectively used to replicate the necessary oscillatory motion at the free end of the blade. When frequency of the input signal is applied at the resonance frequency of the piezofan, the amplitude of the oscillation is maximized resulting in a more complex flow field suitable for use as a practical cooling application.

A number of studies have been carried out to study the cooling capabilities and flow characteristics of piezoelectric fans under first mode orientations. Toda [1,2] proposed the basic models for vibration and airflow and demonstrated a significant reduction in the temperature on placing the piezofan on either side of the transistor panel. Schmidt [3] studied the local and average heat transfer coefficients on a vertical surface cooled by two piezoelectric fans resonating out of phase. It was observed that change in the distance between the fans or between the surface and the fans effected the heat transfer coefficients. Meanwhile, Açıkalın et al. [4] examined the feasibility of placing piezofans in an actual laptop and cell phone enclosure. They determined a significant increase in heat transfer in both cases. On the other hand, Ihara and Watanabe [5] investigated quasi 2D flows around the free ends of a flexible single plate and two plates, both oscillating with a large amplitude. Ro and Loh [6] studied the feasibility of using ultrasonic flexural waves as a cooling mechanism. Analytical, computational, and experimental investigations on incompressible 2D streaming flows induced by resonating thin beams were conducted by Açıkalın et al. [7]. Closed-form analytical streaming solutions were presented for an infinite beam; these solutions were also used to motivate a computational scheme to predict the streaming flows from a baffled piezofan. The predicted asymmetric streaming flows were in good agreement with the experimental flow profiles. Kimber et al. [8–10] experimentally investigated single and arrayed piezoelectric fans vibrating near an electrically heated stainless steel foil. The temperature field was measured by an infrared camera. 2D contours of the local heat transfer coefficient were presented for different vibration amplitudes and gaps. Moreover, correlations were developed with appropriate Reynolds and Nusselt number definitions that described the area average thermal performance of the piezoelectric piezofan with an error of less than 12%. An experimental analysis design for the effects of piezofan amplitude, tip gap, piezofan length at resonance frequency, and piezofan offset from the center of

☆ Communicated by W.J. Minkowycz.

* Corresponding author.
E-mail address: zmfairuz@gmail.com (Z.M. Fairuz).

0735-1933/$ – see front matter © 2013 Elsevier Ltd. All rights reserved.
http://dx.doi.org/10.1016/j.icheatmasstransfer.2013.11.013

Nomenclature

A_{pf}	Amplitude of piezofan (mm)
A_{mc}	Exposed surface area of the microelectronic component (m^2)
l_{pf}	Length of piezofan (mm)
D_{pf}	Width of piezofan (mm)
t_{pf}	Piezofan thickness (mm)
l_{vb}	Length of un-patch piezofan (mm)
q''	Heat flux (W m^{-2})
Q''	Power input to the heat source (W)
	Average heat transfer coefficient (W m^{-2} K^{-1})
	Average temperature of heated surface (K)
T_a	Ambient temperature (K)
	Average force convection (W m^{-2} K^{-1})
	Average natural convection (W m^{-2} K^{-1})
	Velocity vector
u	Velocity (m s^{-1})
	Local grid velocity
	Volume force
x, y, z	Space coordinates
i, j, k	Coordinate indices
t	Time (s)
P	Static pressure (N m^{-2})
g	Gravitational acceleration (m s^{-2})
c_p	Specific heat of air, J kg^{-1} K^{-1}
T	Temperature, K
k	Thermal conductivity, W m^{-1} K^{-1}
CCW	Counter-clockwise
CW	Clockwise

Greek symbols

Φ	Vibration phase angle (degree)
Θ	Traveling wave phase angle (degree)
	Heat transfer coefficient enhancement ratio
δ	Dimensionless spacing between fan tip and heated surface
ρ	Fluid density (kg m^{-3})
	Cauchy stress tensor
τ_{ij}	Viscous stress tensor (N m^{-2})

the heat source was reported by Açıkalın et al. [11]. The heat transfer coefficient could be enhanced by as much as 375% with appropriate specifications of the design parameters. 2D computational fluid dynamics simulation and experimental analysis were performed by Abdullah et al. on the effect of piezofan height on the performance of a single piezoelectric fan in microelectronic cooling system placed in horizontal orientation [12]. A 2D finite element method was reported by Florio and Harnoy to enhance the natural convection cooling of a discrete heat source in a vertical channel with the use of a piezoelectric piezofan [13]. An enhancement of up to 52% in the local heat transfer coefficient was observed relative to that achieved by natural convection. Six piezoelectric piezofans with various blade geometries were made and tested on a flat heated surface by Liu et al. [14]. They experimentally investigated the influence of geometric parameters, including horizontal/vertical arrangement and location of the piezoelectric piezofan. They found that the heat transfer augmentation of the piezoelectric piezofan came from the entrained airflow during each oscillation cycle and the jet-like air stream at the piezofan tip. The heat transfer performance for the vertical arrangement showed a symmetrical distribution and peaked at the center region, whereas the horizontal arrangement possessed an asymmetrical distribution and showed an early peak. The heat transfer performance for the horizontal arrangement was not necessarily lower than that of the vertical arrangement. Kimber et al. [15] experimentally determined the relationship between the pressure and flow rate generated by miniature piezoelectric piezofans. They considered the proximity of surrounding walls with the use of three different enclosures. The aerodynamic interactions between two vibrating piezofans were explored by Kimber et al. [16]. They found that damping is significantly influenced by the proximity of neighboring piezofans and by vibration phase difference. A comparative investigation between 2D numerical flow simulations and experimental data on particle image velocimetry was conducted by Choi et al. [17,18]. They observed the vortex formation and unsteady flow fields around a single and dual vibrating piezofan in free stream. Lin [19,20] recently analyzed 3D heat and fluid flow induced by a single piezofan on flat and cylindrical heat surfaces. He showed that vibrating blade produced a pair of contour-rotating screw type flow structure on either side of the blade and a pair of asymmetric vortex was formed around the piezofan tip. His experimental and numerical results indicated that the piezoelectric piezofan improved the heat transfer coefficient by 1.2 to 3.6 times. Abdullah et al. [21] reported an orientation of multi-piezoelectric piezofan (set in edge-to-edge arrangement) to enhance the heat transfer of finned heat sink in microelectronic cooling with 3D numerical simulation. Their results showed that an enhancement in convective heat transfer coefficient exceeding 88% can be achieved in comparison to that with only natural convection. Sufian et al. [22] reported the influence of single and face to face dual vibrating piezofans, on flow and thermal fields through numerical analyses and experimental measurements. Computed results show that the single piezofan enhanced heat transfer performance by approximately 2.3 times the heated surface. On the contrary, the dual piezofans enhanced heat transfer performance by 2.9 times for out-of-phase vibration and 3.1 for in-phase vibration.

It can be observed from the literature that most studies using numerical and experimental investigations were accomplished while operating at their first resonance mode. There is lack of evidence with regards to the cooling capabilities of piezofan operating at its higher resonance mode. Therefore, in this work attempt has been made to carry out numerical investigation, in order to understand the effect of piezofan mode shape operating at first, second and third mode on the airflow behavior and thermal performance. In addition to this, the experimental results of the first mode obtained using the thermocouples are utilized to compare it with the findings of numerical simulations.

2. Experimental and numerical methods

2.1. Experimental procedures

A commercial piezoelectric piezofan consisting of a bimorph-lead zirconate titanate patch bonded to a thin stainless steel beam and resonating at its first mode natural frequency was used in this investigation. This type of piezofan is ideal for cooling application because of its high elongation properties at relatively low power input requirements (Table 1).

The piezofans was arranged vertically oriented to the heated surface with a spacing of 1.8 mm. A vibrometer (laser displacement sensors KEYENCE LK-G152) was utilized and positioned near the piezofan tip to detect the piezofan-tip deflection and measure the amplitude.

Table 1
Specifications of the piezoelectric piezofan (Piezo Systems Inc., USA).

Specification	Value
Material	Stainless steel
Size (mm)	47 (l_{pf}) × 12 (D_{pf}) × 0.4 (t_{pf})
Length without patch (mm)	23 (l_{vb})
Resonance frequency (Hz)	110 (first mode of vibration)
Power consumption (mW)	42
Weight (kg)	0.002

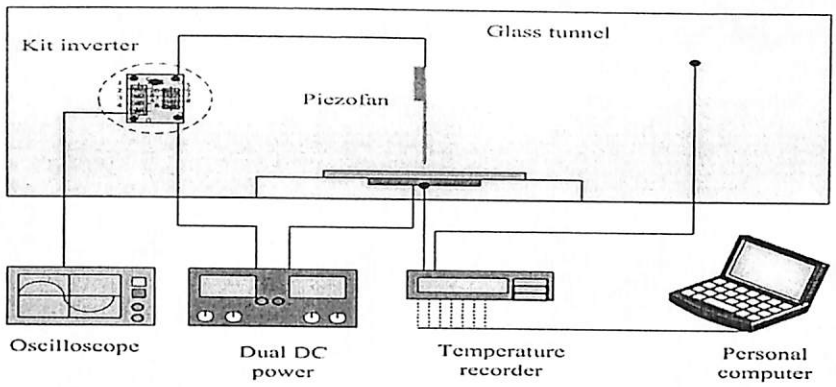

Fig. 1. Schematic experimental setup for piezoelectric fan.

The measurement point of the focal laser beam to the piezofan surface was 1 mm from the piezofan tip. A digital storage (DSO3062A Oscilloscope) connected to an inverter drive circuit was provided to tune the frequencies and supply the input signals for the piezofan. The inverter circuit was also joined with an input channel provided by a DC dual power supply (GWinstek GPS2303) to deliver the voltages required for the piezofan operation, whereas the other channel was fed to the chip (heat source). The inverter circuit was used to convert the DC to AC voltage, in order to drive the piezoelectric fan. The frequency was adjusted by turning the trimmer pot on the printed circuit board. The piezoelectric fan was driven at a first resonance frequency (approximately 110 Hz) with an input of 42 mW. The piezofan movement was recorded using, the IMC DAQ system and the input displacement along with the frequency signal of the sensor was stored in the computer. The error of the displacement sensor was found to be $-/+0.02\%$.

The microelectronic component was simulated by an aluminum foil (size 82 mm × 90 mm × 1 mm) heated with a uniform heat flux of 1200 W m^{-2} by means of a stainless steel electrical heater attached beneath the foil. The foil-heater was fixed into the cavity of a wooden platform in such a way that their top surfaces were coplanar. The wooden platform served as an insulator and enabled only the top surface of the heated foil to be exposed to the ambient environment. Therefore, the heat loss through the wooden platform was assumed negligible. A heat sink compound RS® of high conductivity was used to bind the heater with the foil. Six thermocouples (K-type, TTK-36-SLE) were attached on the outer surface of the plate to determine the average surface temperature, and one thermocouple was used to measure the ambient temperature. All thermocouples were linked to a desktop PC that utilized a data acquisition system (Advantech USB-4718, eight-channel). The temperatures were recorded every 60 s, and the ambient temperature was maintained at 22 °C. Figs. 1 and 2 shows the assembly of the microelectronic component and the piezofan housed in a glass tunnel to reduce ambient effects.

The rate of heat flux (q'') generated by the heat source was computed according to the following equation:

$$q'' = \frac{Q}{A_{mc}} \tag{1}$$

where (Q°) and (A_{mc}) are the power input and surface area of the microelectronic component, respectively.

The average heat transfer coefficient was defined based on the difference between the average temperature of the heated surface and the ambient temperature over the heated surface:

$$\overline{h} = \frac{q''}{(\overline{T}_s - T_a)} \tag{2}$$

where $\overline{T}_s$ is the average temperature of the aluminum plate surface, and (T_a) is the ambient temperature.

In order to estimate the cooling effect on account of using the piezofan, the enhancement ratio [14] which represents convection during piezofan operation was divided by that obtained under natural convection:

$$\xi = \overline{h}_{pf} / \overline{h}_n \tag{3}$$

where $\overline{h}_{pf}$ is the average heat transfer coefficient achieved under force convection (ON-piezofan), and $\overline{h}_n$ is the average heat transfer coefficient achieved under natural convection condition for the experiment (OFF-piezofan), which was about 22 W K^{-1} m^2.

2.2. Computational methods and boundary conditions

In the computational approach, real time coupling between finite volume method (FVM) and FEM-based software was carried out using

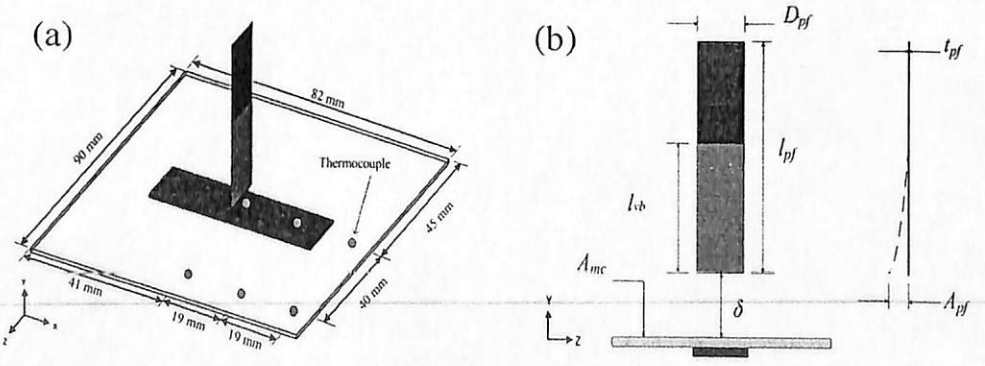

Fig. 2. Details of experimental setup inside the glass tunnel showing the a) thermocouples positioned on the heated surface and b) geometric description of piezoelectric fan.

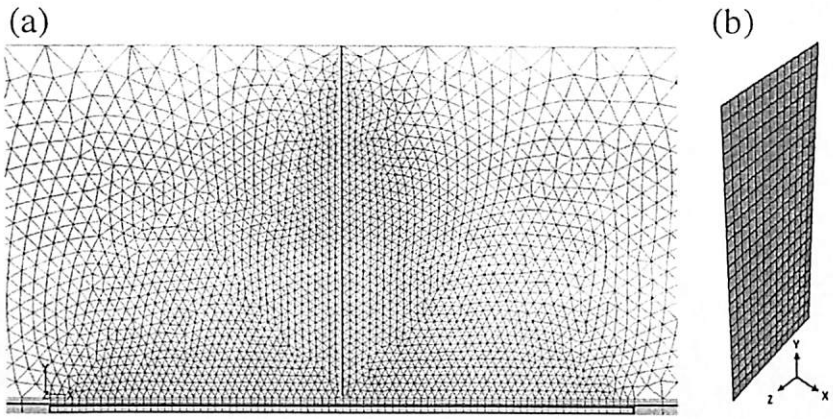

Fig. 3. The meshed model (a) at the middle of computational domain in FLUENT and (b) vibrating beam in ABAQUS.

the MpCCI software. The structural solver ABAQUS was employed to impose the movement of the vibrating beams in the fluid domain. Whereas, FLUENT was used to solve the fluid flow around the beams and to simulate the heat transfer characteristics of the microelectronic device.

The heated surface area of the microelectronic component was similar to that used in the experiment, and the clamp of the piezoelectric fan was neglected. The computational domain was $7.3l_{pf}$ in length and width and $1.05l_{pf}$ in height. The unstructured tetrahedral mesh elements were clustered around beam surfaces, to avoid the formation of highly skewed elements due to the beam movement [21]. Similarly, structured quadrilateral elements with the $y+$ value equal to 1 was developed at the vicinity of the heated surface in order to treat turbulent flow at the near-wall region as shown in Fig. 3a. The total mesh count in the fluid domain amounted to nearly about 0.8 million cells. The unsteady and incompressible RANS equations were solved using an implicit and segregated three-dimensional finite-volume method.

The first-order upwind discretization scheme was used both for momentum and energy equations, with the SIMPLE scheme for pressure–velocity coupling. Shear stress transport (SST) k–ω model was used to describe the flow induced by the vibrating piezofan, which has local turbulence. A uniform heat flux was applied on the heated surface similar to the experimental setup, whereas the surrounding area (wooden platform) at the bottom boundary was insulated at wall $q = 0$ having no-slip boundary definition. The top and four side boundaries of the computational domain were treated as pressure boundaries. A time step size of 0.0001 s was chosen for all cases, with 100 time steps per cycle of piezofan vibration. The total duration of the simulation was selected, such that the temperature reached a steady value during this period. A total of 10,000 iterations were required for the entire operation which corresponded to approximately five days of computation time per case on a Pentium Dual Core processor (2.8 GHz) computer with 2.0 GB memory.

Actuation kinematics of all three mode shape of the vibrating beam vibration was developed using the ABAQUS algorithm having maximum tip amplitude of 5 mm identical to the first mode of the experiment. Fig. 3b shows the vibrating beam model of solid finite element where 300 C3D8 (8-node linear brick) elements were applied. The modal deformations of the piezofan at each mode are shown in Fig. 4. The deformable structure for FEM includes the geometrical entities of the vibrating beam and the beam's corresponding mechanical properties. The components were modeled as homogeneous materials with isotropic material behavior, constant densities, and linear Young's modulus. To implement the beam motion in the structural model, dynamic implicit functions were applied. The beam was assumed to vibrate at a frequency of 100 Hz; a round off value compared with the experimental value of 109 Hz was made to achieve numerical stability. The exact values of the beam vibration amplitudes A_{pf} were considered in performing the simulation in accordance with the experimental measurements. The gravitational force was assumed negligible owing to light weight of the beam under study.

2.2.1. Geometrical modeling and grid generation

2.2.1.1. Governing equations. The numerical solution coupled two separated numerical models with two topological surfaces, flow, and structural solvers. The coupling process for the numerical simulation requires the equation for mass and momentum in arbitrary Lagrangian–Eulerian formulation. The conservation of mass and momentum

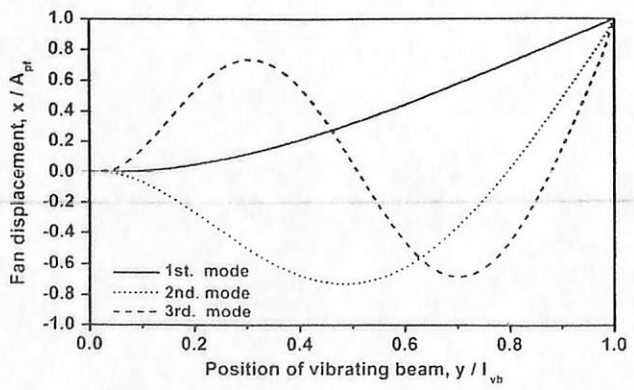

Fig. 4. The position and the amplitude of vibrating beam.

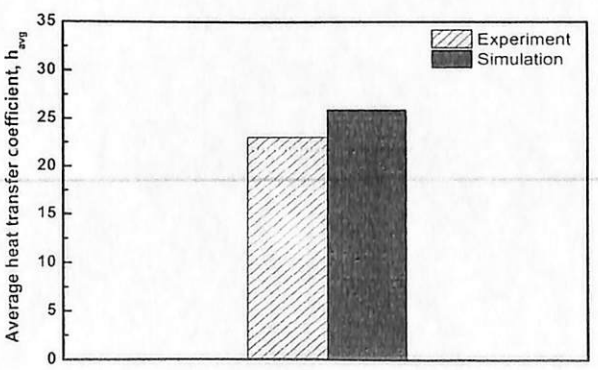

Fig. 5. Average heat transfer coefficient for the experimental and numerical findings.

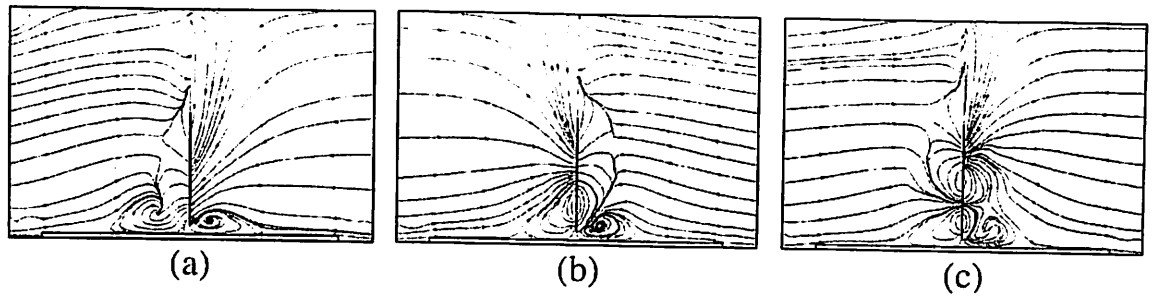

Fig. 6. Streamlines captured at middle plane (z-plane) of computational domain at neutral position during left swing: (a) first mode (b) second mode and (c) third mode.

equations of the continuum mechanic formulation for an incompressible medium are expressed as follows [23]:

$$\nabla \cdot \left(\vec{u} - \vec{u}_g\right) = 0 \tag{4}$$

$$\rho \cdot \left[\frac{\partial \vec{u}}{\partial t} + \left(\left(\vec{u} - \vec{u}_g\right) \cdot \nabla\right) \cdot \vec{u}\right] = \nabla\sigma + \vec{f} \tag{5}$$

where ρ is the density, u→ is the velocity vector, u→g is the local grid velocity, σ is the Cauchy stress tensor, and f→ is the volume force.

The kinematic and dynamic coupling conditions (i.e., corresponding to local normalized vector) for the data exchange via the topologically identical surface of the two computational domains must be identical. Thus, the equations are expressed as follows:

$$\vec{x}_{fluid} = \vec{x}_{solid} \tag{6}$$

$$\vec{u}_{fluid} = \vec{u}_{solid} \tag{7}$$

$$\vec{\sigma}_{fluid} = \vec{\sigma}_{solid} \tag{8}$$

where x→ is a position vector.

The governing equations employed in FLUENT to describe transient fluid flow are as follows:

Continuity:

$$\frac{\partial \rho}{\partial t} + \frac{\partial}{\partial x_i}(\rho u_i) = 0. \tag{9}$$

Momentum (non-accelerating reference frame):

$$\frac{\partial}{\partial t}(\rho u_i) + \frac{\partial}{\partial x_j}\left(\rho u_i u_j\right) = -\frac{\partial P}{\partial x_j} + \frac{\partial \tau_{ij}}{\partial x_j} + \rho g_i + F_i \tag{10}$$

where ρ is the fluid density, P is the pressure in the fluid, τ_{ij} is the viscous stress tensor, and g_i is the gravitational acceleration in the i-direction.

Energy:

$$\frac{\partial}{\partial t}\left(\rho c_p T\right) + \frac{\partial}{\partial x_j}\left(\rho u_i u c_p T\right) = k\frac{\partial^2 T}{\partial x_j^2} \tag{11}$$

where c_p is the specific heat of air, T is the temperature, and k is the thermal conductivity. For the structural solver, the finite-element method for nonlinear deformation are used and solved based on the following equation of motion [23]:

$$[M]\{q\} + [C]\{\dot{q}\} + [K]\{q\} = \{F\} \tag{12}$$

where $\{q\}$ is the displacement vector, $[M]$ is the mass matrix, $[C]$ is the damping matrix, $[K]$ is the stiffness matrix, and $\{F\}$ is the force vector due to the fluid dynamic load, inertial load and shear stresses.

3. Results and discussions

Fig. 5 illustrates the comparison between measured and computed heat-transfer coefficients for the first mode case achieved on the heated surface. The results show a relatively good agreement between the experimental and numerical findings. The deviations between numerical simulation and experimental work are estimated to be 12.65%, which is attributed to the omission of the radiation effect in the numerical model. This is further corroborated by deducting the experimentally determined radiative contribution based on the predicted value. Besides, the thickness of the thermal compound in the simulation is assumed to be uniform, which in reality might be uneven owing to its manual application. Another reason for this discrepancy can be attributed to the use of only a single thermocouple to measure the ambient temperature in the experiments. In addition to this, only the average fluid temperature was considered for the simulation inside the heat piezo domain.

Figs. 6a,b,c and 7a,b,c present the streamlines obtained for the middle plane (z-plane) of calculation domain at neutral position during left (i.e., in negative x-direction) and right swing (i.e., in positive x-direction) respectively. For the purpose of simplicity, the streamlines are studied only at the neutral position corresponding to a complete half-cycle where the maximum velocity is achieved. Here the vortex formation is still in its early stage and at the beginning of the swing,

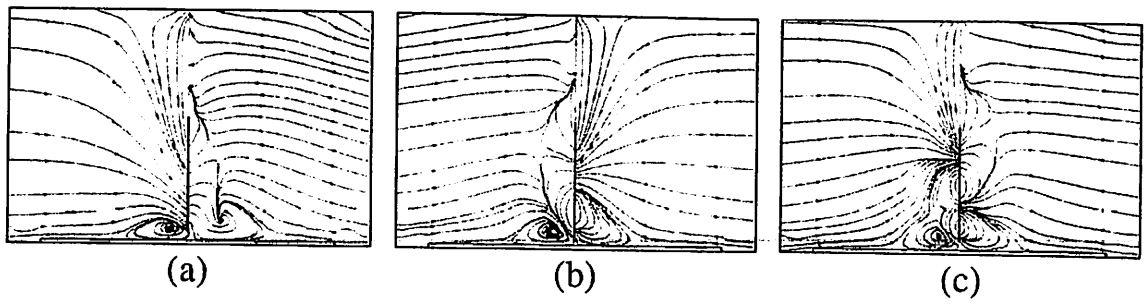

Fig. 7. Streamlines captured at middle plane (z-plane) of computational domain at neutral position during right swing: (a) first mode (b) second mode and (c) third mode.

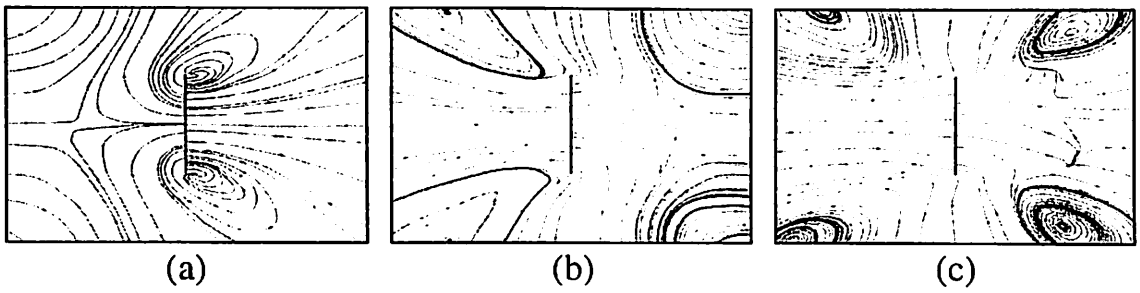

Fig. 8. Streamlines captured at $0.6l_{vb}$ (y-plane) of computational domain at neutral position during left swing: (a) first mode (b) second mode and (c) third mode.

which otherwise is usually shed at end of the swing as reported by Acikalin et al. [11] and Sufian et al. [22].

Figs. 6a and 7a present the streamlines for the piezofan operating at its first mode. It can be seen from the figures that the tip displacement due to the first mode shape results in the formation of a pair of asymmetric vortex (i.e. recirculation flow) having diametrically opposite flow direction just near the front and the back of the piezofan tip. The most prominent vortex can be observed around the piezofan tip just behind the vibrating beam, in the direction of the beam sweep. The blade motion, induces suction just behind the vibrating plate, wherein a stream of air is sucked from the top (high pressure and low velocity region) towards the bottom (low pressure and high velocity region) of the piezofan resulting in a high velocity jet impinging on the heated surface. This flow regime after striking the surface is pushed further outwards and encounters the already induced vortex, thereby resulting in a stronger vortex in the vicinity of the piezofan tip. The suction phenomenon and the formation of a pair of asymmetric vortex observed around the piezofan tip due the first mode vibration are similar to that reported by Acikalin et al. [4,11].

Figs. 6b and 7b present the streamlines for the piezofan operating at its second mode. It can be observed from these figures that, vortex is generated around the piezofan tip just behind the vibrating beam, in the direction of the beam sweep. In contrast to the first mode, suction of air stream is limited to middle region around the blade. This can be attributed to second mode vibration which tends to create ripple effect neutralizing the low pressure region created earlier. Consequently, the vortex formed might not be of the same intensity as that obtained under single mode condition, naturally hampering its heat transfer abilities. In case of second mode, a distinct suction occurs along the midpoint of vibrating beam corresponding to the antinode of the second mode of vibration. When the out of phase antinodes in the mid of beam and the piezo tip vibrate alternately through multiple oscillations, the airflow stream is disturbed and hampers the formation of recirculatory flow at the front tip of vibrating beam. As a result, the vortex is not generated in front of the piezofan tip in the direction of the beam sweep. This in turn causes reduction in the induced velocity impinging on the heated surface.

The streamlines of the piezofan operating at its third mode are shown in Figs. 6c and 7c. Similar to the second mode behavior, a distinct suction occurs near the antinode point during third mode of vibration. This can drastically reduce the velocity induced on the heated surface and this decrease could be much lesser than that observed for the second mode vibration. Furthermore, in comparison to the second mode vibration, the higher velocity suction zone if observed to be smaller. Consequently, as the vibrating beam sweeps during both swing motions (Figs. 6c and 7c), a less distinct recirculation zone is observed around the piezofan tip. This may be the primary reason for the reduction in the induced velocity on the heated surface.

In general, any increase in the mode numbers, will reduce the higher velocity suction along the bottom of the vibrating beam, thereby drastically decreasing the heat transfer performance of the thermal boundary layer developed on top of the heated surface. The higher modes of vibration result in localized disturbance of the airflow patterns relative to the anti node position, which rather impedes the general thrust of flow as observed during the first mode of vibration. Thus, it does not significantly contribute towards the objective of providing high velocity jet impinging on the heater surface located at the bottom of the piezofan.

Figs. 8a,b,c and 9a,b,c present the streamlines at two different horizontal sections (y-plane) of computational domain i.e., at $0.6l_{vb}$ and $0.9l_{vb}$ respectively. The streamlines are captured at neutral position during left swing corresponding to a complete half-cycle. Since, the length is measured from top to the bottom of vibrating beam, the location of computational domain at $0.9l_{vb}$ is located in close proximity to the bottom of the vibrating beam.

It can be seen from the Figs. 8a and 9a for the first mode piezofan operation that, a pair of vortex of the opposite circulation is formed at both side of the vibrating beam edges. The upper flow structure rotates in the clockwise-direction whereas the lower flow structure rotates in the counter-clockwise direction. As the vortex is spiraling downwards toward the bottom of the vibrating beam it tends to gradually detach from the vibrating beam and strike the heated surface. As a consequence it can increase the induced velocity on top of the heated surface and thereby improve the heat transfer performance as well.

The description of the streamlines for the second mode is shown in Figs. 8b and 9b. It is observed from these figures that at $0.6l_{vb}$ no vortex is formed at both side of the vibrating beam in contrast to that determined in case of the first mode vibration. On the other hand, at $0.9l_{vb}$, a smaller and less distinct pair of vortex of the opposite circulation is formed when compared to that observed during the first mode. Furthermore, vortex created at upper side of the piezofan is pushed away on

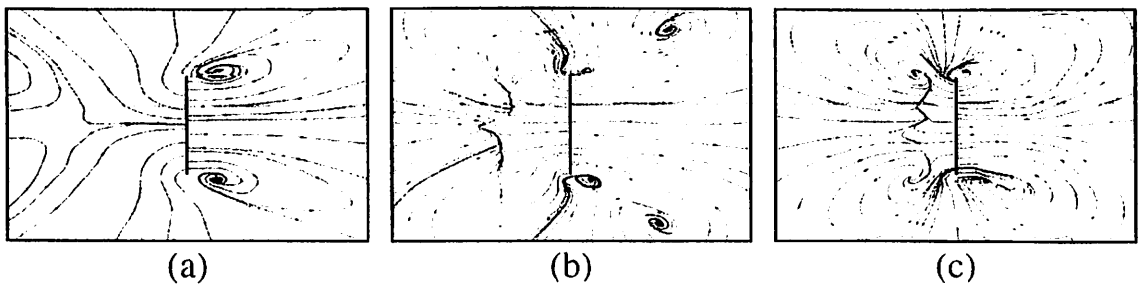

Fig. 9. Streamlines captured at $0.9l_{vb}$ (y-plane) of computational domain at neutral position during left swing: (a) first mode (b) second mode and (c) third mode

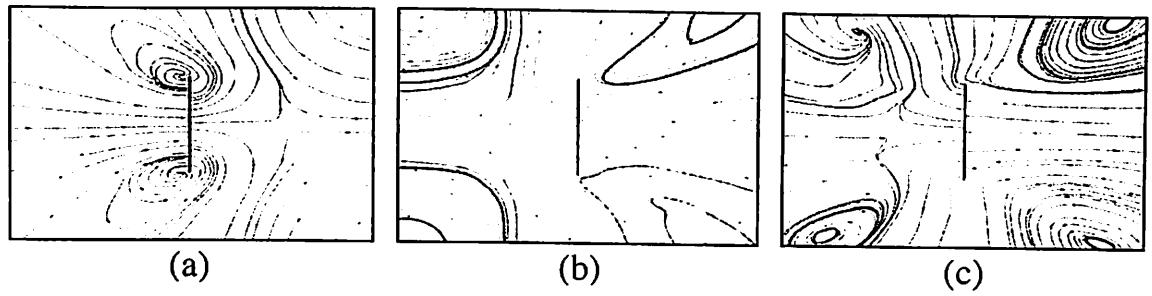

Fig. 10. Streamlines captured at plane $0.6l_{vb}$ (y-plane) of computational domain at neutral position during left swing; (a) first mode (b) second mode and (c) third mode.

subsequent vibrations (Fig. 8b), whereas that induced at the blade tip tends to impinge on the heater surface (Fig. 9b). Similar findings can be seen in case of the third mode vibrations (Fig. 8c), wherein vortex at the upper part are pushed away from the piezofan during subsequent oscillations. However, a pair of vortex of the opposite circulation is formed on either side of the beam as shown in the Fig. 9c in contrast to that observed during the second and first mode vibrations.

Similar to Figs. 8 and 9, the streamline plot for right swing of the piezofan is shown in Figs. 10a,b,c and 11a,b,c at two different horizontal sections of the computational domain i.e., at $0.6l_{vb}$ and $0.9l_{vb}$ respectively. Figs. 10a and 11a identify a distinct pair of vortices of the opposite circulation during its first mode, commensurate with the beam shift direction. Similar behavior is observed at the first mode as shown in Figs. 8a and 9b but in different rotational directions. Figs. 10b and 11b present the streamlines operating at its second mode. It is similar to that observed in Figs. 8b and 9b at $0.6l_{vb}$ and $0.9l_{vb}$ respectively but in different rotational directions. Similarly, the third mode vibrations represented in Figs. 10c and 11c have identical behavior to that presented in Fig. 8c and 9c but in different rotational directions. This pair of vortex of the opposite circulation observed at the both sides of the vibrating beam edges is shown in Figs. 8, 9, 10 and 11 are similar to that presented by Lin [19,20].

It can be seen that the air stream is pushed along the edges (Figs. 8a, 9a, 10a and 11a) and pulled from the top towards the bottom (Figs. 6a and 7a) during the first mode of vibrating beam. This results in the formation of a pair of vortex of opposite circulation flowing downward on both side of vibrating beam edges. In contrast, as the second and the third mode of vibrating beam oscillate through a complete cycle, the air is pulled either from the top or bottom of the piezofan (Figs. 6b,c and 7b, c) to the antinode point of vibration mode and consequently disturb the induced supplemented air flow for the formation of the vortex at both side of vibrating beam edges. As a result no or less distinct vortex is formed with the higher mode number. This can drastically reduce the velocity of flow impinging on the heated surface and therefore can reduce its overall heat transfer ability.

As the vibrating beam oscillates periodically, the induced velocity in the thermal boundary layer on the top of the heated surface varies over time. Fig. 12 presents the induced velocity magnitude distributions at different beam positions operating under their representative mode shapes; neutral position Fig. 12a,e and i and maximum displacement position Fig. 12b,f and j during left swing, and neutral position Fig. 12c,g and k and maximum displacement Fig. 12d,h and i during right swing.

Fig. 12a,b,c and d presents the velocity magnitude distributions operating at its first mode. It is observed from the figures that an elliptical-shape contour of velocity profile appears as the vibrating beam swept through multiple oscillations, whereas a uniform low velocity distribution was observed at the remaining system domain. It can be clearly seen in Fig. 12a that a higher velocity profile is observed at the back of the piezofan in the direction of the beam sweep. This can be attributed to the formation of a distinct vortex as shown in Fig. 6a. As the vibrating beam moves from neutral position to the point of maximum displacement (Fig. 12b), the velocity decreases on either side of the piezofan due to the vortex shedding. The change in the oscillation direction prompts a higher velocity profile at the other side of the piezofan tip (Fig. 12c), which is identical to the distinct vortex formed as shown in Fig. 7a. Finally, as the vibrating beam reaches maximum displacement (Fig. 12d), the velocity decreases on either side of the piezofan due to vortex shedding.

Fig. 12e,f,g and h presents the velocity magnitude operating at its second mode. In case of the second mode vibration, a circular-shape contour of velocity profiles appear on the top of the heated surface in contrast to first mode which developed elliptical contours of velocity magnitude. Although a more prominent higher velocity profile appears at the back of the piezofan tip in the direction of the beam sweep (Fig. 12e and g) on account of the vortex formed as shown in Figs. 6b and 7b, it is dimmer than that observed at the first mode. This shows that the velocity distribution on top of the heated surface is substantially reduced. Finally, as the vibrating beam reaches maximum displacement (Fig. 12f and h), the velocity decreases on either side of the piezofan due to vortex shedding with much lower velocity magnitude then that observed at first mode. The third mode transition shows similar behavior observed during the second mode with substantially reduced velocity distribution and circular-shaped contours. Another characteristic feature of higher mode vibrations is the effect of blade area envelop that contributes towards the flow patterns. It can be observed from the figure that, only the bottom one third of the surface area of blade effectively contributes to the velocity that impinges on the heater surface, whereas rest of the blade area is out of phase and creates localized disturbance near to the mode deformation vicinity (refer Figs. 6b, c, 7b

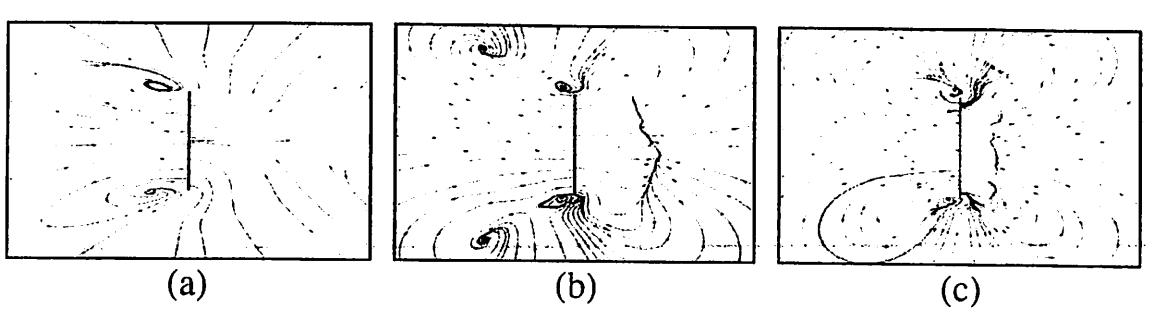

Fig. 11. Streamlines captured at plane $0.9l_{vb}$ (y-plane) of computational domain at neutral position during left swing; (a) first mode (b) second mode and (c) third mode.

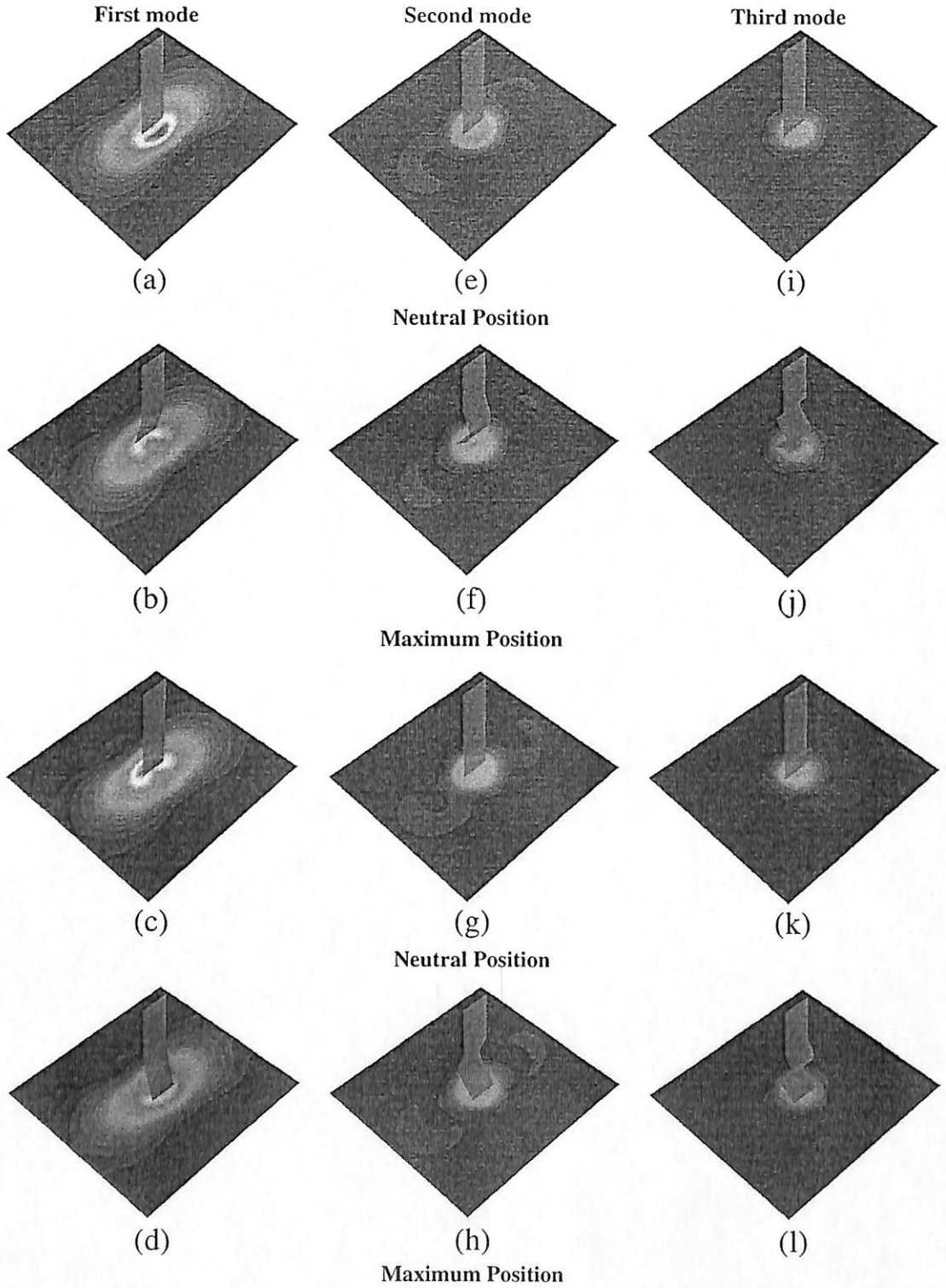

Fig. 12. Velocity contours at different beam positions starting from left swing to the right swing.

and c). In contrast, the first mode vibration has the entire piezo blade contributing to the air blanket that impinges on the heater surface. The entire surface area of the blade strikes the air blanket on the blade swept direction, thereby pushing the flow towards its intended target. This results in highly effective flow over the heater surface and therefore, the first mode vibration is better than the higher modes.

To further substantiate the behavior of piezofan quantitatively, a local trace of dimensionless velocity distribution is plotted along

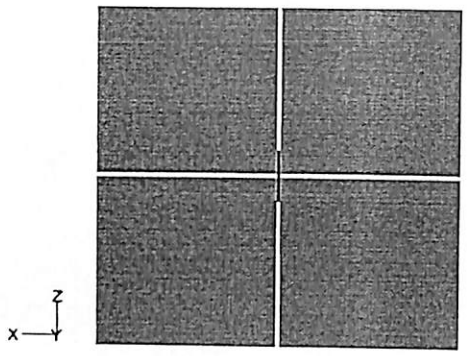

Fig. 13. The location of measurements along x-axis (along swept direction) and z-axis on the plane surface.

x-axis and z-axis on the same plane of computational domain as in Fig. 12 at neutral position of the vibrating beam displacement during both left and right swing corresponding to a complete half-cycle as shown in Figs. 14, 15, 16 and 17. The location of measurement lines are shown in Fig. 13. The black and light gray lines represent the piezofan (at neutral position) and measurement line respectively.

Fig. 14 presents the dimensionless velocity distribution along x-axis for the representative mode shape at neutral position during the left swing corresponding to the complete half-cycle. As observed from the figure, the dimensionless velocity distribution shows a significant decrease with increase in mode number. Along the middle plane, the dimensionless distribution of velocity along the x-axis for all mode shapes remains relatively constant. At the mid plane a massive jump in velocity magnitude appears which increases rapidly, roughly from $x = 0.02$ (or $x = -0.02$), making its highest peak around $x = 0.0055$ (or $x = -0.0055$) at both sides of the beam beyond which it starts to decline. The higher peak velocity observed can be attributed to the formation of a stronger vortex on either side of the piezofan tip and impingement jet developed by the vibrating beam (Fig. 6) with the decrease of mode number. Meanwhile, at $x > 0.02$ (or $x < -0.02$), the dimensionless velocity for all modes is relatively lower, which indicates that the natural convection condition dominates the heat transfer in this region.

Fig. 15 presents the dimensionless velocity distribution along z-axis, representing mode shape conditions at neutral position during the left swing corresponding to a complete half-cycle. It is observed in the figure that the velocity distributions are almost symmetric about the middle plane for all mode shape, however showcasing significant decrease in its magnitude with increase in the mode number. Along

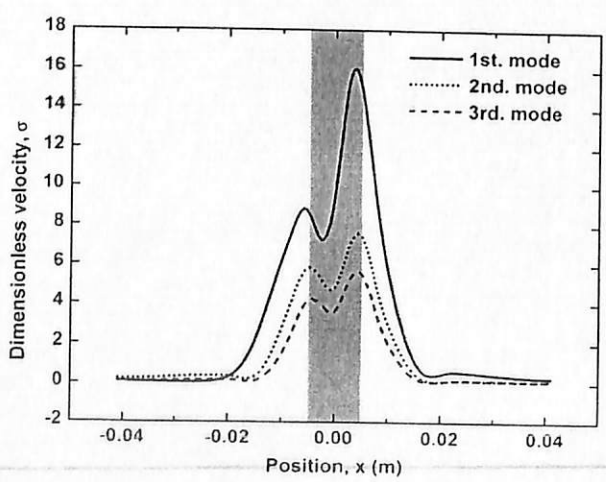

Fig. 14. The variation of dimensionless velocity as a function of position along x-axis of the plane at neutral position during the left swing. Shaded region represent vibration envelope.

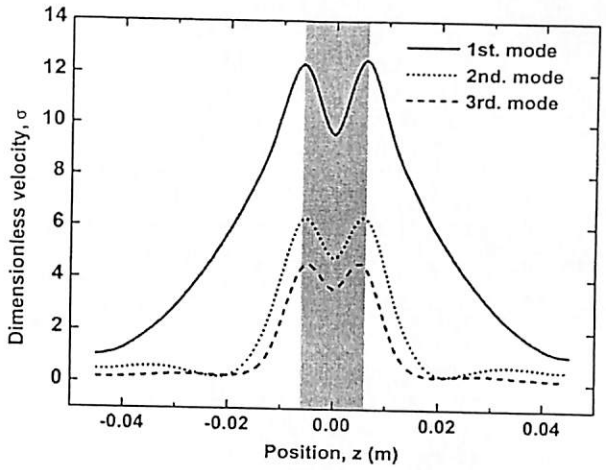

Fig. 15. The variation of dimensionless velocity as a function of position along z-axis of the plane at neutral position during the left swing. Shaded region represent vibration envelope.

the middle plane for the second and third modes, the dimensionless distribution of velocity remain relatively constant initially, than a massive jump of velocity profiles appears roughly from $z = 0.02$ (or $z = -0.02$), making its highest peak around $z = 0.005$ (or $z = -005$), beyond which it starts to decline. Meanwhile, at $z > 0.02$ (or $z < -0.02$), the air stream velocity profiles for the second and third mode is relatively low which signifies that the natural convection condition dominate the heat transfer in this region. However, in case of the first mode, the dimensionless velocity distribution increase rapidly along the middle plane, achieving its highest peak around $z = 0.005$ (or $z = -0.005$), beyond which it starts to decline. Furthermore, it can be seen that the highest peaks of dimensionless velocity appear at the edge of vibrating beam for all mode shapes. This is due to high velocity induced by pair vortex formed at the edge of vibrating beam that spiral out downward and impingement jet developed by the vibrating beam shown in Figs. 6, 7, 8, 9, 10 and 11.

Fig. 16 presents the dimensionless velocity distribution along x-axis for all mode numbers, at neutral position during the right swing corresponding to a complete half-cycle. It can be seen that the pattern and behavior observed for right swing is similar to that observed for left swing (refer Fig. 16) with the only exception that the two highest peak are formed at the other side of the middle plane.

Fig. 17 presents the dimensionless velocity distributions along z-axis for all mode number, at neutral position during the right swing

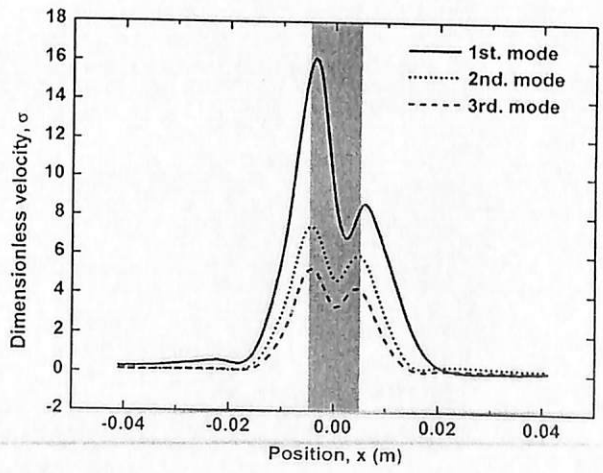

Fig. 16. The variation of dimensionless velocity as a function of position along x-axis of the plane at neutral position during the right swing. Shaded region represent vibration envelope.

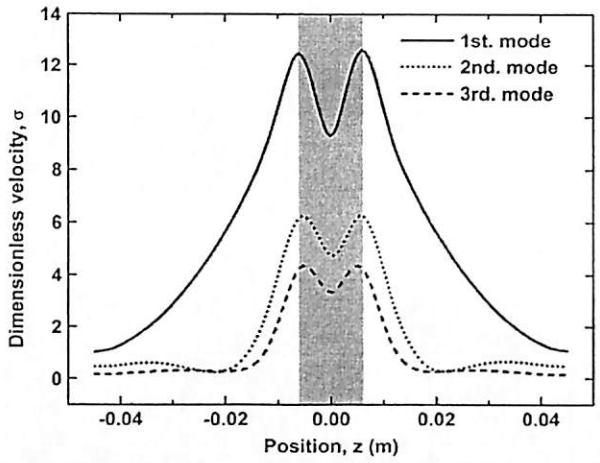

Fig. 17. The variation of dimensionless velocity as a function of position along z-axis of the plane at neutral position during the right swing. Shaded region represent vibration envelope.

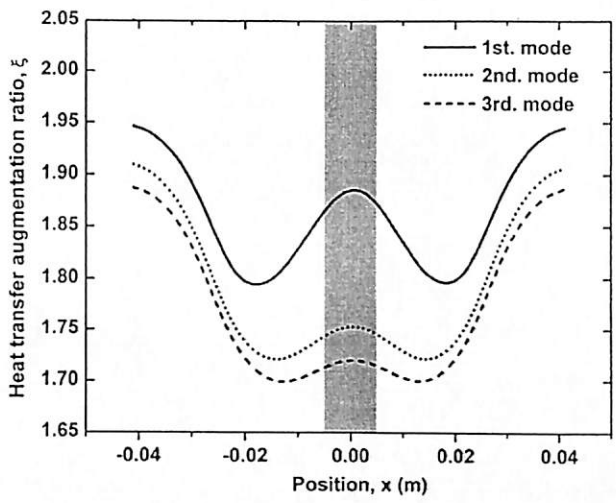

Fig. 19. Variations of heat transfer augmentation ratio along the x-axis as a function of position on the top of heated surface at neutral position during left swing. Shaded region represents vibration envelope.

corresponding to a complete half-cycle. It can be seen from the figure that the pattern and behavior observed for right swing is similar to that determined for left swing (refer Fig. 15).

Figs. 12, 14, 15, 16 and 17 clearly shows a clear reduction in suction of the air stream towards the bottom of the piezofan with the increase in mode number. Any further decrease in the air stream results in weaker vortex formation which affects the velocity of the impingement jet directed towards the bottom of the piezofan. In addition to this, it can be seen that, as the vibrating beam cycles through multiple oscillations, more vortices are generated and pushed away from the piezofan at the upper side than at the tip of the vibrating beam without striking the heater surface as the mode number increases. As a consequence, the impact of velocity distribution on the top of the heated surface is drastically reduced.

The effect of mode shape on temperature distribution is also evaluated. Fig. 18 presents the temperature distributions on top of the heated surface at neutral position during both the left (Fig. 18a, b and c) and right swings (Fig. 18d, e and f) corresponding to a complete half-cycle. It is observed in the figure that the temperature distributions are symmetrical about the middle plane with almost identical temperature magnitudes and contour for both the left and right swing. Inspection of Fig. 18 around the vibrating beam shows a couple of higher

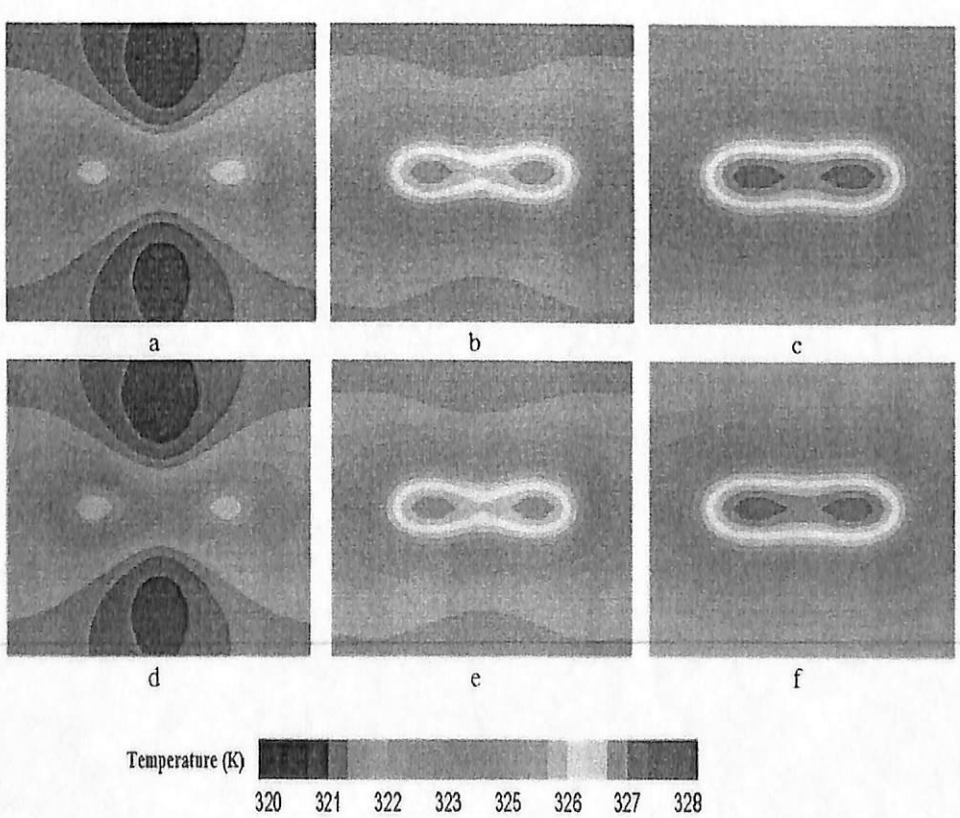

Fig. 18. Temperature contours at neutral position during left swing: (a) first mode (b) second mode, (c) third mode and right swing: (d) first mode (e) second mode and (f) third mode.

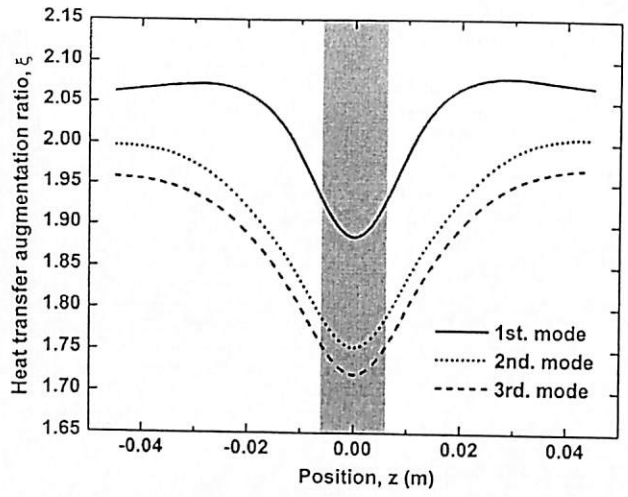

Fig. 20. Variations of heat transfer augmentation ratio along the *z*-axis as a function of position on the top of heated surface at neutral position during left swing. Shaded region represents vibration envelope.

temperature spots at the left and right of the middle plane with the lowest temperature at the middle plane. This area of higher temperature spot around the middle plane is where the heat source is located. The two higher temperature spots are located farthest between the vibrating beam and the heated surface, whereas lower temperature region in the middle is nearest (i.e., at neutral position) during oscillation. It can be clearly observed from the figure that the hourglass shaped temperature contour propagating from the two higher temperature spots change increasingly to a bigger shape (i.e., of higher temperature) with the increase in mode number. Besides, a couple of cooler spots at the upper and lower portions of the figure during the first mode can be attributed to the higher velocity of elliptical shape profile demonstrated in Fig. 12.

The heat transfer coefficient augmentation ratio along *x*-axis and *z*-axis obtained on top of the heated surface are also analyzed. Since the heat transfer coefficient augmentation ratio is relatively similar during both swings under representative mode shape condition as shown in Fig. 18, the traces along *x*-axis and *z*-axis are analyzed for only the left swing.

As seen in Fig. 19, for heated surface along *x*-axis the heat transfer augmentation ratio varies relative the velocity profile seen in Fig. 14a, b and c. In contrast to velocity distribution, the heat transfer augmentation ratio is symmetrical about the middle plane and a clear decrease in its magnitude can be seen with the increase in mode numbers. It can be seen that the average heat transfer augmentation ratio for second and third mode is reduced by 4% and 5% relative to first mode vibrations. Similarly the maximum heat transfer augmentation ratio at the middle plane has indicated reduction by about 7% and 9% for both the higher modes of vibrations relative to the first mode.

Fig. 20 shows the heat transfer coefficient augmentation ratios along the *z*-axis. It can be seen in the figure that the heat transfer augmentation ratio is symmetrical about the middle plane which substantially decreases with the increase of mode number. The heat transfer augmentation ratio of the first mode decreases from $x = 0.15$ to the middle plane where it reaches its minimum beyond which it remains relatively constant. Whereas the heat transfer augmentation ratio for the second and third mode decreases significantly in comparison with the first mode. The second and third mode vibrations have demonstrated a reduction of the average heat transfer augmentation ratio by 6% and 7%, whereas the maximum heat transfer augmentation ratio at the middle plane by 7% and 9% relative to the first mode.

Thus, it has been established in this study that the increase in the mode number, causes reduction in the velocity magnitude. The lower fluid velocity attributed to the higher mode numbers, results in increase of thermal resistance across the boundary layer developed over the heated surface. This in turn decreases the amount of heat carried away by the fluid accounting for lower heat transfer augmentation ratio.

Higher mode of vibrations requires increased power consumption. In addition to this the higher operating frequency results in more noise which makes the piezofan impractical for future cooling application. Therefore, these findings show that it is recommended to operate the piezofan at its fundamental resonance mode.

4. Conclusions

Numerical investigation was carried to study the effect of three different mode shapes (first, second and third modes) on flow and heat transfer performance of the piezefan. The average heat transfer coefficients obtained using experimental and numerical studies for the first mode have shown good agreement between them.

The vibrating blade of the first mode produced a pair of asymmetric vortex (i.e. recirculation flow) of opposite circulation around front and the back the piezofan tip, and a pair of vortex of opposite circulation at both side of vibrating beam edges. With the increase of mode number these vortex tend to disappear around the vibrating blade.

As the mode of vibration increases, a clear reduction in suction of the air stream towards the bottom of the piezofan with the increase in mode number is observed. Any further decrease in the air stream results in weaker vortex formation and impingement jet directed towards the bottom of the piezofan. As a consequence, the impact of velocity distribution on the top of the heated surface is substantially reduced due to higher mode number.

The low fluid velocity due to the increase of the mode number, causes increase in the thermal resistance across the boundary layer from the fluid to the heated surface. This, in turn, decreases the amount of heat that is carried away by the fluid, accounting for the lower heat transfer augmentation ratio with the increase in mode number. The second and third mode vibrations have demonstrated a reduction of the average heat transfer augmentation ratio by 6% and 7%, whereas the maximum heat transfer augmentation ratio at the middle plane by 7% and 9% relative to the first mode. Thus it is found that higher mode of vibrations is ineffective and therefore the fundamental resonance mode is suggested for all practical piezofan applications.

Acknowledgement

The authors would like to thank the Universiti Sains Malaysia for the financial support through RU Grant Number 1001/PMEKANIK/814163.

References

[1] M. Toda, Theory of air flow generation by a resonant type PVF2 bimorph cantilever vibrator, Ferroelectrics 22 (1979) 911–918.
[2] M. Toda, Voltage-induced large amplitude bending device PVF2 bimorph its properties and applications, Ferroelectrics 32 (1981) 127–133.
[3] R.R. Schmidt, Local and average transfer coefficients on a vertical surface due to convection from a piezoelectric piezofan, Thermal Phenomena in Electronic Systems, 1994. I-THERM IV. 'Concurrent Engineering and Thermal Phenomena' InterSociety Conference on, 1994, pp. 41–49.
[4] T. Acikalin, S.M. Wait, S.V. Garimella, A. Raman, Experimental Investigation of the thermal performance of piezoelectric piezofans, Heat Transf. Eng. 25 (1) (2004) 4–14.
[5] A. Ihara, H. Watanabe, On the flow around flexible plates oscillating with large amplitude, J. Fluids Struct. 8 (7) (1994) 601–619.
[6] P.I. Po, L. Byoung-Gook, Feasibility of using ultrasonic flexural waves as a cooling mechanism, IEEE Trans. Ind. Electron. 48 (1) (2001) 143–150.
[7] T. Acikalin, A. Raman, S.V. Garimella, Two-dimensional streaming flows induced by resonating, thin beams, J. Acoust. Soc. Am. 114 (4) (2003) 1785–1795.
[8] M. Kimber, S.V. Garimella, A. Raman, Local heat transfer coefficients induced by piezoelectrically actuated vibrating cantilevers, J. Heat Transf. 129 (9) (2007) 1168–1176.
[9] M. Kimber, S.V. Garimella, Measurement and prediction of the cooling characteristics of a generalized vibrating piezoelectric piezofan, Int. J. Heat Mass Transf. 52 (19–20) (2009) 4470–4478.
[10] M. Kimber, S.V. Garimella, Cooling performance of arrays of vibrating cantilevers, J. Heat Transf. 131 (11) (2009) 111401.

[11] T. Acikalin, S.V. Garimella, A. Raman, J. Petroski, Characterization and optimization of the thermal performance of miniature piezoelectric piezofans, Int. J. Heat Fluid Flow 28 (4) (2007) 806–820.
[12] M.K. Abdullah, M.Z. Abdullah, M.V. Ramana, C.Y. Khor, K.A. Ahmad, M.A. Mujeebu, Y. Ooi, Z. Mohd Ripin, Numerical and experimental investigations on effect of piezofan height on the performance of piezoelectric piezofan in microelectronic cooling, Int. Commun. Heat Mass Transf. 36 (1) (2009) 51–58.
[13] L.A. Florio, A. Harnoy, Use of a vibrating plate to enhance natural convection cooling of a discrete heat source in a vertical channel, Appl. Therm. Eng. 27 (13) (2007) 2276–2293.
[14] S.-F. Liu, R.-T. Huang, W.-J. Sheu, C.-C. Wang, Heat transfer by a piezoelectric piezofan on a flat surface subject to the influence of horizontal/vertical arrangement, Int. J. Heat Mass Transf. 52 (11–22) (2009) 2565–2570.
[15] M. Kimber, K. Suzuk, N. Kitsunai, K. Seki, S.V. Garimella, Pressure and flow rate performance of piezoelectric piezofans, IEEE Trans. Components Packag. Technol. 32 (4) (2009) 766–775.
[16] M. Kimber, R. Lonergan, S.V. Garimella, Experimental study of aerodynamic damping in arrays of vibrating cantilevers, J. Fluids Struct. 25 (8) (2009) 1334–1347.
[17] M. Choi, C. Cierpka, Y.H. Kim, Vortex formation by a vibrating cantilever, J. Fluids Struct. 31 (2012) 67–78.
[18] M. Choi, S.-Y. Lee, Y.-H. Kim, On the flow around a vibrating cantilever pair with different phase angles, Eur. J. Mech. - B/Fluids 34 (2012) 146–157.
[19] C.-N. Lin, Analysis of three-dimensional heat and fluid flow induced by piezoelectric piezofan, Int. J. Heat Mass Transf. 55 (11–12) (2012) 3043–3053.
[20] C.-N. Lin, Heat transfer enhancement analysis of a cylindrical surface by a piezoelectric piezofan, Appl. Therm. Eng. 50 (1) (2013) 693–703.
[21] M.K. Abdullah, N.C. Ismail, M. Abdul Mujeebu, M.Z. Abdullah, K.A. Ahmad, M. Husaini, M.N.A. Hamid, Optimum tip gap and orientation of multi-piezofan for heat transfer enhancement of finned heat sink in microelectronic cooling, Int. J. Heat Mass Transf. 55 (21–22) (2012) 5514–5525.
[22] S.F. Sufian, M.Z. Abdullah, J.J. Mohamed, Effect of syncronized piezoelectric piezofans on microelectric cooling performances, Int. Commun. Heat Mass Transf. 43 (2013) 81–89.
[23] Z.M. Fairuz, M.Z. Abdullah, H. Yusoff, M.K. Abdullah, Fluid structure interaction of unsteady aerodynamics of flapping wing at low Reynolds number, Eng. Appl. Comput. Fluid Mech. 7 (1) (2013) 144–158.

Microelectronics Reliability 54 (2014) 1534–1543

Contents lists available at ScienceDirect

Microelectronics Reliability

journal homepage: www.elsevier.com/locate/microrel

Thermal analysis of dual piezoelectric fans for cooling multi-LED packages

S.F. Sufian [a,*], Z.M. Fairuz [a], M. Zubair [c], M.Z. Abdullah [a], J.J. Mohamed [b]

[a] School of Mechanical Engineering, Universiti Sains Malaysia, Engineering Campus, Nibong Tebal 14300, Penang, Malaysia
[b] School of Material and Mineral Resources Engineering, Universiti Sains Malaysia, Engineering Campus, Nibong Tebal 14300, Penang, Malaysia
[c] Department of Aerospace Engineering, Universiti Putra Malaysia, Campus, Serdang 43400, Selangor, Malaysia

ARTICLE INFO

Article history:
Received 30 December 2013
Received in revised form 21 March 2014
Accepted 21 March 2014
Available online 30 April 2014

Keywords:
LED package
Piezoelectric fan
Transient numerical simulation
Fluent
MpCCI
Junction temperature

ABSTRACT

This paper reports on the dissipation of heat generated by a high power LED array using piezoelectric fans. Both numerical and experimental studies were carried out to evaluate the heat dissipation efficiency of high power LED package operating under multiple vibrating fans. Two vibrating fans were vertically oriented to the LED package and arranged according to configuration A (for edge to edge arrangement), and configuration B (for face to face arrangement). The junction temperature (T_j), thermal resistance (R) and average heat transfer coefficient $\bar{h}$ were estimated. The results show that the single fan enhanced heat transfer performance approximately 1.8 times for the LED package. On the contrary, the dual fans enhanced heat transfer performance approximately by 2.3 times for configuration A and 2.4 for configuration B. A significant decrease in the thermal resistance was observed for all the configurations when fan separation distance δ was reduced. The best performance relative to natural convection was found to be at ($\delta = 0.1$) which decreased the thermal resistance using single fan by about 38%, whereas the dual fan accounted for 49.5% in case of configuration A, and 50.6% for configuration B.

1. Introduction

Over the last few years, light emitting diode (LED) has seen a tremendous surge in its application as new generation lighting technology, replacing the conventional general lighting (gas lights), such as incandescent and fluorescent lamps. Light emitting diode (LED) is a solid state semiconductor device that converts electrical energy into a visible light. Several applications such as the LCD back light source, television, automotive and general lighting use LEDs on account of its compact size, low power consumption, long lifetime, short response time and environmental protection.

Only a minor portion of the LED power input converts into a visible light of particular wave length, and the rest appears as unwanted heat which adversely affects the maintainability of low LED die temperature. Accordingly, most of the applications that require very high lumens necessitate multi-chip LED module. Thermal characterization of LEDs packages in an array is very different from that of single LED package. The junction temperature of LEDs packages will be significantly influenced not only by ambient temperature but the side effect from multiple chips [1]. Sustaining LEDs in lower junction temperature results in higher luminous efficacy, longer lifetime, and stable emission wavelength of the light output [2]. Thus, in order to extract maximum benefits from LEDs, heat dissipation solutions become crucial. The commonly methods of cooling used for the present applications of LEDs in the market are mostly confined on heat sinking techniques (passive cooling) [3]. However, the passive cooling relatively has very low cooling efficiency and therefore, higher heat dissipation solutions are urgently needed.

Many heat dissipation solutions have been investigated for the thermal management of LEDs. Jang et al. [4] optimized the cooling performance and mass of a pin-fin radial heat sink for LED lighting applications. They reported that the system was sensitive to the number of fin arrays, as well as the length of the long and middle fins. Their design for the optimum radial heat sink reduced the mass by more than 30% while maintaining a similar cooling performance to that of a plate-fin heat sink. Ha and Graham [5] developed a thermal resistance model for chip-on-board packaging of high power LED arrays. They proposed an analytical thermal resistance model for the LED array and validated by comparing it with finite element analysis (FEA) results.

Kim et al. [1] reported the thermal characterization of high power LED arrays cooled by a heat pipe. They used thermal transient methods to measure the junction temperature and calculate the thermal resistance with and without heat pipe. Also, Lu et al.

* Corresponding author. Tel.: +60 174773789.
E-mail address: sufianfarid@gmail.com (S.F. Sufian).

http://dx.doi.org/10.1016/j.microrel.2014.03.016
0026-2714/

Nomenclature

A_{pf}	amplitude of piezoelectric fan (mm)
A_b	exposed surface area of MCPCB (m^2)
l_{pf}	length of piezoelectric fan (mm)
D_{pf}	width of piezoelectric fan (mm)
t_{pf}	piezoelectric fan thickness (mm)
l_u	length of un-patch piezoelectric fan (mm)
q	heat flux ($W m^{-2}$)
Q	LED array heat input (W)
$\bar{h}$	average heat transfer coefficient ($W m^{-2} K^{-1}$)
T_j	LED array device junction temperature (K)
T_s	LED array solder point temperature (K)
T_b	board (MCPCB) temperature (K)
T_a	ambient temperature (K)
$\vec{u}$	velocity vector
u	velocity ($m s^{-1}$)
$\vec{u}_g$	local grid velocity
$\vec{f}$	volume force
x, y, z	space coordinates
n	number of LED chips
R	total thermal resistance ($K W^{-1}$), $R = R_{js} + R_{sb} + R_{ba}$
R_{js}	thermal resistance from device junction to solder point on the MCPCB top ($K W^{-1}$)
R_{sb}	thermal resistance from solder point to MCPCB bottom ($K W^{-1}$)
R_{ba}	thermal resistance from MCPCB bottom to the ambient ($K W^{-1}$)
i, j, k	coordinate indices
t	time (s)
P	static pressure ($N m^{-2}$)
g	gravitational acceleration ($m s^{-2}$)
c_p	specific heat of air ($J kg^{-1} K^{-1}$)
T	temperature (K)
k	thermal conductivity ($W m^{-1} K^{-1}$)
CCW	counter-clockwise
CW	clockwise

Greek symbols

δ	dimensionless spacing between fan tip and heated surface
ρ	fluid density ($kg m^{-3}$)
σ	Cauchy stress tensor
τ_{ij}	viscous stress tensor ($N m^{-2}$)

[6], Lin et al. [7], and Li et al. [8] proposed a combination of heat pipe with heat sink as a cooling technique for carrying out thermal analysis of high power LED. Shyu et al. [2] studied the thermal characterization of shrouded plate fin array (heat sink) on an LED backlight panel consisting of 270 1-W LEDs in an acrylic housing. Their results showed that the heat transfer coefficient slightly reduced with the rise of shroud clearance from 0 mm to 5 mm, followed by a notable rise. However, the heat transfer coefficient peaks at a shroud clearance between 10 and 20 mm and any further increase of shroud clearance leads to a marginal decrease of heat transfer coefficient. Thermal performance of three kinds of LED vapor chamber-based plates comparing the experiments, theories, and simulation thermal resistances were discussed by Wang [9]. His results showed that the thermal performance of the LED vapor chamber-based plate was better than that of the LED copper-based plate. Yung et al. [10] presented thermal analysis and experimental validation of natural convective air cooling of a high brightness 3 × 3 LED array package on a printed circuit board (PCB) during operation from 0° to 180° inclinations. Their analysis results revealed that the effect of position and inclination plays an important role in the heat dissipation of the LED package. Refrigerating liquid for LED's thermal management integrated within a fabricated prototype was proposed and investigated by Faranda et al. [11]. Their experimental results reported that the refrigerating liquid reduces the junction temperature, and can positively influence the luminous radiation performances. An active cooling solution using liquid metal as the coolant was proposed for high power (LEDs) by Deng and Liu [12]. Besides, Xiaobing and Sheng [13] and Liu et al. [14] proposed a microjet array cooling system for thermal management of high-brightness LEDs demonstrating excellent performance.

On the other hand, several researchers [15–22] have recently proposed the vibrating fans (piezoelectric fans) as potential cooling technique on account of its compact size, low power consumption, noise-free operation and adaptability in small spaces. Piezoelectric fans are micro-vibrating machines used as airflow generators to help dissipate heat. They consist of a cantilever beam bonded with a piezoelectric material near their base ends. An input signal to the piezoelectric material causes oscillatory motion at the free end of the beam; this signal could induce the surrounding flow.

Acikalin et al. [22] experimentally investigated the optimal design of single piezoelectric fan for extracting heat from a heat source and proposed its possibility for cooling light emitting diodes (LEDs). They considered different experimental configurations, and the effect of varying the fan amplitude, distance between the fan and heat source, fan length, its frequency offset from resonance, and the fan offset from the center of the heat source were studied to assess the cooling potential of piezoelectric fans. They found that applying piezoelectric fan resulted in a temperature drop at the heat source by more than 36.4 °C.

Although, many researchers focused on the thermal and flow analysis of vibrating fans over a single heat source (single chip) in microelectronic applications, the thermal analysis of vibrating fan for cooling LED package (multi-chips) is still lacking in the literature. Only Acikalin et al. [22] experimentally investigated the thermal performance of single vibrating fan in context of LED. This calls for further investigations into the study of characteristic influence of multiple vibrating fans on the resulting heat transfer associated with LED heating.

Therefore, in this work the thermal behavior of LED array system cooled by means of piezoelectric fans is carried out. Experimental and numerical analysis on the thermal characterization of LED package under natural and forced convection conditions are explored. Furthermore, dual vibrating fans are vertically oriented to the LED package and arranged in two different ways namely: configuration A (for edge to edge arrangement), and configuration B (for face to face arrangement). Vibrometers (laser displacement sensors KEYENCE LK-G152) are employed to measure the vibration amplitude fans. 3D simulations based on a dynamic meshing scheme are performed in FLUENT and ABAQUS with the use of code coupling interface MpCCI to investigate transient changes on the temperature and flow fields achieved by dual vibrating fans. The thermal performance of the dual fans is compared relative to the single fan, and the estimated results are also compared with the experimental findings.

2. Experimental setup and procedure

Experiments were performed to assess the thermal performance of dual piezoelectric fans on a package of multiple LED sources. The heat sources consisted of nine high power LEDs of type (LUW W5AM). They were soldered as package (82 mm × 60 mm) on the metal core of printed circuit board (MCPCB) and connected in a typical parallel electrical array. The bottom surface of this package was directly exposed to vibrating fans, while the mounted LEDs appeared on top of the MCPCB as shown in Fig. 1. The LED package was placed horizontally on a non-conductive Bakelite (k = 0.23 W/m K) platform which also serves as insulator. Thermal resistance characteristics were analyzed for the piezoelectric fans arranged in two different ways, edge to edge arrangement for configuration A, and face to face arrangement for configuration B, as shown in Fig. 2. The LED package was powered with 12.6 W direct current (DC) dual power supply (GW instek GPS2303) with ±5% accuracy. A portion of this power transformed into lighting, and the remaining into heat. Therefore, the transformation of the electrical energy into heat energy was estimated to be 80% at heating power (Q) of 10.08 W [23,24] for the nine LED chips. Eight points on the LED package were carefully selected at quarter zone of MCPCB to measure the temperature and were symmetrical about the entire heated zone (MCPCB). Four thermocouples (K-type, TTK-36-SLE) were attached at the top of MCPCB to the cathode leads of LED, and remaining four were attached to the opposite end of the LED at the bottom of the MCPCB as shown in Fig. 3. All of these thermocouples were linked to a desktop PC utilizing a data acquisition system (Advantech USB-4718, 8-channel). The temperature was recorded for every 60 s and the ambient temperature in the environmental chamber was always monitored to be 22 °C.

The commercially available piezoelectric fans used in present study consisted of a bimorph Lead Zirconate Titanate (PZT) patch bonded to a thin stainless steel blade. Table 1 shows the high elongation properties of this piezoelectric fan at relatively low power input.

Laser displacement sensors (KEYENCE LK-G152) was used to measure the vibration amplitude of the fans. The measurement points of the focal laser beam to the fan surfaces were (1 mm) from the fan tip and the error of the displacement sensor was ±0.02%. Slightly different resonance frequencies existed between the fans due to the discrepancy in manufacturing and a slight difference in phase could be expected between their motions. The input signal of the fans was carefully monitored with two-channel digital storage (DSO3062A Oscilloscope) connected with two inverter drive circuits provided for tuning the frequencies for each fan independently. All experiments were conducted with a fixed input driving power (42 mW) for each fan. Every fan has its own particular fundamental resonance frequency, which was experimentally determined to be 109.64 and 108.79 Hz for fans 1 and 2, respectively. No two fans can have identical resonance frequencies because of unavoidable defects during manufacturing and that yield to exchange the vibration phase during the fans' operation even with identical input signal [21]. This means that, in-phase (or out-of-phase) vibration cannot remain the same for longer duration. Therefore, in this work only in-phase vibration mode is considered to study the performance of the dual vibrating fans.

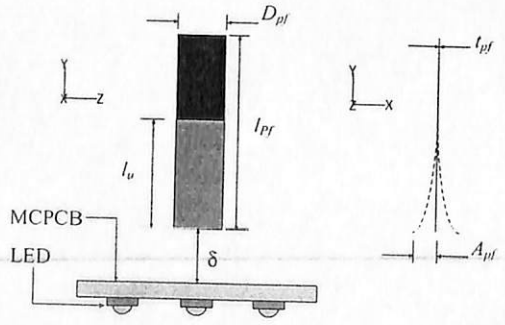

Fig. 1. Schematic of experimental setup for piezoelectric fans oriented vertically to the bottom of LED package.

Two essential parameters were investigated in this study; the arrangement of two vibrating fans relative to a single fan and separated distance between fans tip and LED package. The thermal resistance of LED is induced between the interfaces of the various elements that constitute the package [25]. The thermal resistance between junction and ambient air for the LED assembly on the metal core printed circuit board can be written as the sum of three thermal resistances as represented in Fig. 4 and is given by the relation:

$$R = R_{js} + R_{sb} + R_{ba} \tag{1}$$

where R_{js} is thermal resistance from device junction to solder point (given by manufacturer of LED on data sheet 6.5 K/W) [26], R_{sb} is thermal resistance from solder point on the top to the bottom of MCPCB, and R_{ba} is thermal resistance from MCPCB bottom to the ambient (R_{sb} and R_{ba} were experimentally determined).

$$R_{js} = (T_j - T_s)/Q \tag{2}$$

$$R_{sb} = (T_s - T_b)/Q \tag{3}$$

$$R_{ba} = (T_b - T_a)/Q \tag{4}$$

where T_j, T_s, T_b and T_a are device junction temperature, solder point temperature (MCPCB top), board (MCPCB bottom) temperature in a steady state condition and the ambient temperature respectively.

Thermal resistance of multiple LED arrays having multiple heat sources can be explained in terms of the parallel thermal resistance network as shown in Fig. 5. This model used parallel thermal resistance to represent each individual LED. The R_{js} and R_{sb} for multiple LED array was obtained by using parallel resistances and the total equation of the entire package can thus be simplified to Eq. (5).

$$R = \frac{1}{\sum_{n=1}^{n=9} \frac{1}{R_{jsn}+R_{sbn}}} + R_{\mathrm{ba}} \tag{5}$$

The average heat transfer coefficient $\bar{h}$ can be described in terms of thermal resistances for thermal convection which is represented by R_{ba} [27]:

$$R_{ba} = \frac{1}{\bar{h}A_b} \tag{6}$$

where A_b is the board exposed surface area to the fans.

3. Computational methods and boundary conditions

The simulation was performed in accordance with the procedures described in Sufian et al. [21]. However, in this computational method, coupling code (MpCCI 3.1) was used to couple finite volume method (FVM)- and FEM-based software in the fluid and heat transfer analyses. Therefore, the transformation of analysis generated from the FEM code (ABAQUS 6.9) to the FVM code (FLUENT 6.3.26) was conducted via MpCCI 3.1, resulting in the real-time data transfer. The piezoelectric fans were defined as the coupled regions. ABAQUS as a solid solver was employed to impose the movement of the vibrating beams into the fluid domain and deformations were simultaneously estimated. The forces induced from the solid acting on the fluid were directly solved

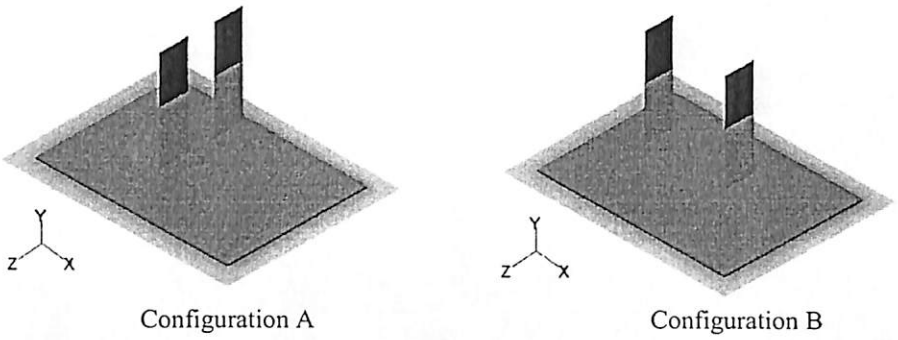

Fig. 2. Dual fan oriented vertically to the LED package, A (edge to edge arrangement) and B (face to face arrangement).

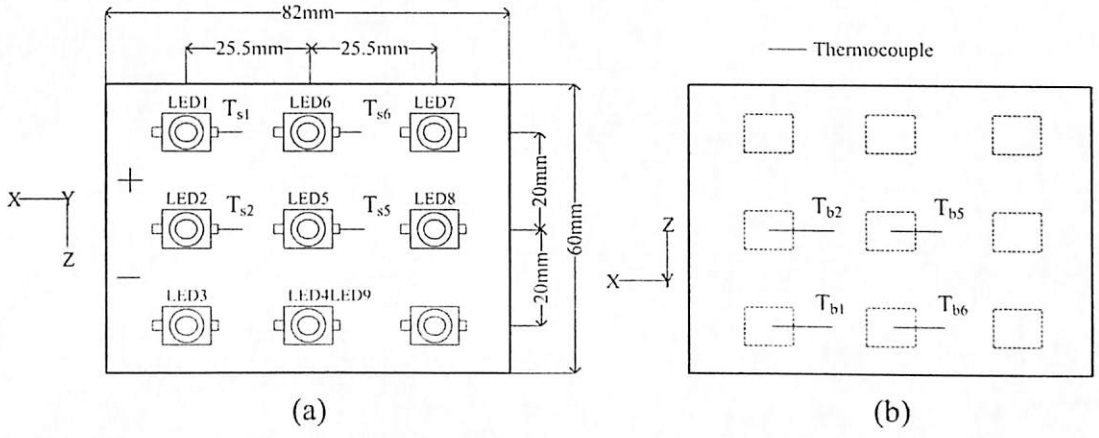

Fig. 3. Thermocouple locations at (a) top and (b) bottom of MCPCB.

Table 1
Specifications of the piezoelectric fan (Piezo Systems Inc., USA).

Specification	Value
Material	Stainless steel
Size (mm)	47 (l_{pf}) × 12 (D_{pf}) × 0.4 (t_{pf})
Length without patch (mm)	23 (l_u)
Resonance frequency (Hz)	110
Power consumption (mW)	42
Weight (kg)	0.002

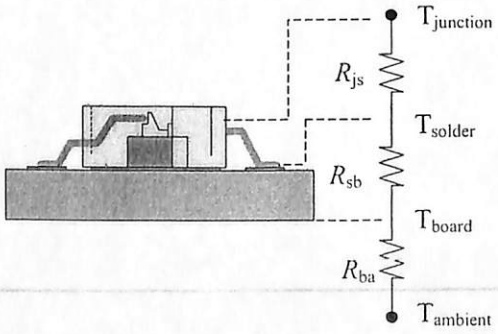

Fig. 4. Thermal resistance series of single LED soldered onto MCPCB.

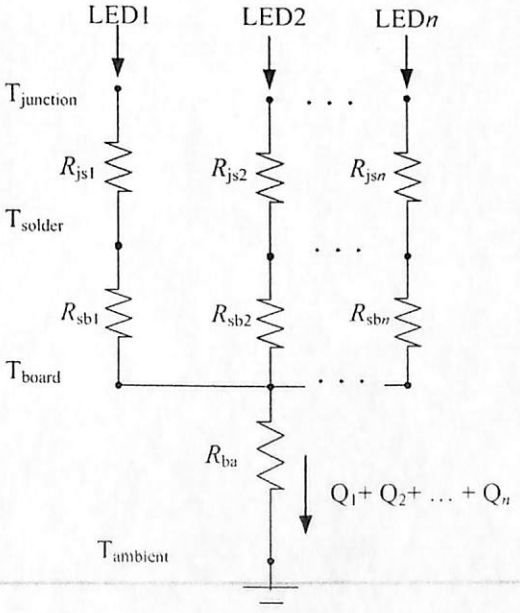

Fig. 5. Thermal network of LEDs arrays.

using FLUENT, which calculated the fluid flow field around the beams and heat rate of the microelectronic device.

The first-order upwind discretization scheme was used in FVM for momentum and energy equations, with the SIMPLE scheme utilized for pressure–velocity coupling. The y^+ value was set as 1 in treating turbulent flow at the near-wall region (heat source surface). A uniform heat flux from the contact surface area of each single LED chip was applied evenly on the MCPCB

according to the estimated value of $q = 28{,}400\ W/m^2$, whereas the surrounding area (Bakelite platform) at the bottom boundary was insulated at wall $q = 0$ under no-slip condition. The top and four side boundaries of the computational domain were treated as pressure boundaries. The beams were defined as coupling surface boundaries. The dynamic mesh option was activated in FLUENT during the calculations. A time step size of 0.0001 s was chosen for all cases, with 100 time steps per cycle of fan vibration. The total duration of the simulation was selected, such that the temperature reached a steady value during this period. A total of 10,000 iterations were reached, which correspond to approximately five days of computation time per case on a Pentium Dual Core processor (2.8 GHz) computer with 2.0 GB memory.

The deformable structure for FEM includes the geometrical entities of the vibrating beam and the beam's corresponding mechanical properties. The components were modeled as homogeneous materials with isotropic material behavior, constant densities, and linear Young's modulus (210 GPa). To implement the beam motion in the structural model, dynamic implicit functions were applied. The beam was assumed to vibrate at a frequency of 100 Hz; this round off compared with the experimental value of 109 Hz was made to achieve numerical stability. The exact values of the beam vibration amplitudes A_{pf} were considered in performing the simulation according to the experimental measurements.

3.1. Geometrical modeling and grid generation

Two types of 3D models were created for coupling purpose: (a) modeling of the fluid domain surrounding the heat surface and (b) modeling of the deformable beams. For the fluid domain, the surface and volume meshes were generated with GAMBIT 2.3.16 and exported to FLUENT 6.3.26 for analysis. The computational domain had dimensions of 14.2 cm length, 12 cm width, and the height varied from 4.82 cm to 6.7 cm according to the separation distance between the fans' tip and LED package. The entire package was modeled as MCPCB having dimension of (82 mm × 60 mm × 1 mm). Besides, the contact surface area for each chip had dimensions of (6.8 mm × 5.8 mm). Thus, the heat was assumed to be dissipated directly from the active region of each individual chip to MCPCB, and then to ambient by convection.

Hybrid grids (combination of tetrahedral and hexahedra element) was employed and interfaced into the fluid domain as shown in Fig. 6(a). The unstructured mesh of tetrahedral elements was clustered around beam surfaces to avoid damaged fluid cells. The fluid cells can be highly skewed because of beam movement. A structured mesh was required at the vicinity of the heated surface to treat turbulent flow at the near-wall region. Therefore, the fluid domains were meshed within 400,000 to half million cells for different cases according to the spacing between the beams and the heated surface. The spacing from the fan tip to the heated surface was varied from 1.2 mm to 20 mm. Thus, (δ) which is the ratio of the fan tip spacing to the fan width (D_{pf}) varied from 0.1 to 1.6. The deformable structures were created and meshed with FEM-based software (ABAQUS) as per their actual beam dimensions. The rigid beams were suspended in vertical ordination. Fig. 6(b) shows that the hexahedral element scheme is applied to generate a mesh of 380 elements for each beam.

3.2. Governing equations

The numerical solution coupled two separated numerical models which were flow and structural solvers. The coupling process for the numerical simulation requires the equation for mass and momentum in arbitrary Lagrangian–Eularian formulation. The conservation of mass and momentum equations of the continuum mechanic formulation for an incompressible medium are expressed as follows:

$$\nabla \cdot (\vec{u} - \vec{u}_g) = 0 \tag{7}$$

$$\rho \cdot \left[\frac{\partial \vec{u}}{\partial t} + ((\vec{u} - \vec{u}_g) \cdot \nabla) \cdot \vec{u}\right] = \nabla\sigma + \vec{f} \tag{8}$$

where ρ is the density, $\vec{u}$ is the velocity vector, $\vec{u}_g$ is the local grid velocity, σ is the Cauchy stress tensor, and $\vec{f}$ is the volume force.

The kinematic and dynamic coupling conditions (i.e., corresponding to local normalized vector $\vec{n}$) for the data exchange via the topologically identical surface of the two computational domains must be identical. Thus, the equations are expressed as follows:

$$\vec{x}_{fluid} = \vec{x}_{solid} \tag{9}$$

$$\vec{u}_{fluid} = \vec{u}_{solid} \tag{10}$$

$$\vec{\sigma}_{fluid} = \vec{\sigma}_{solid} \tag{11}$$

where $\vec{x}$ is a position vector.

The governing equations employed in FLUENT to describe transient fluid flow are as follows:

Continuity:

$$\frac{\partial}{\partial x_i}(\rho u_i) = 0 \tag{12}$$

Momentum (non-accelerating reference frame):

$$\frac{\partial}{\partial t}(\rho u_i) + \frac{\partial}{\partial x_j}(\rho u_i u_j) = -\frac{\partial P}{\partial x_j} + \frac{\partial \tau_{ij}}{\partial x_j} + \rho g_i + F_i \tag{13}$$

where ρ is the fluid density, P is the pressure in the fluid, τ_{ij} is the viscous stress tensor, and g_i is the gravitational acceleration in the i-direction.

Energy:

$$\frac{\partial}{\partial t}(\rho c_p T) + \frac{\partial}{\partial x_j}(\rho u_i u c_p T) = k\frac{\partial^2 T}{\partial x_j^2} \tag{14}$$

where c_p is the specific heat of air, T is the temperature, and k is the thermal conductivity.

4. Results and discussion

4.1. Flow field

The correlation between the flow fields and the thermal behavior induced by the piezoelectric fans are introduced by the numerical studies. The advantage of numerical method is that it provides an accurate solution to the complexity of the transient flow field generated by vibrating fans. In this work two basic piezoelectric fans configurations A and B are analyzed. Fig. 7 shows the velocity contours on the heated surface and the development of flow field induced by the dual vibrating fans. The velocity vectors and streamlines are also displayed for the computational plane of $z = 1.2$ mm and $z = 0$ mm (crossed the fans) at three different instants for both the configurations A and B.

It can be seen from the figure that, for configuration A, the plane of computational domain crosses only one fan at ($z = 1.2$ cm). However, identical pattern of flow is also observed for other fan and hence its results are not presented. Both the fans move simultaneously from their natural position towards its maximum deflection in the positive x-direction (Fig. 7a). The motion of the blade from its normal mean position to extreme right position results in the formation of a clockwise (CW) vortex just above the fan tip along the beam swept direction. Besides, a counterclockwise

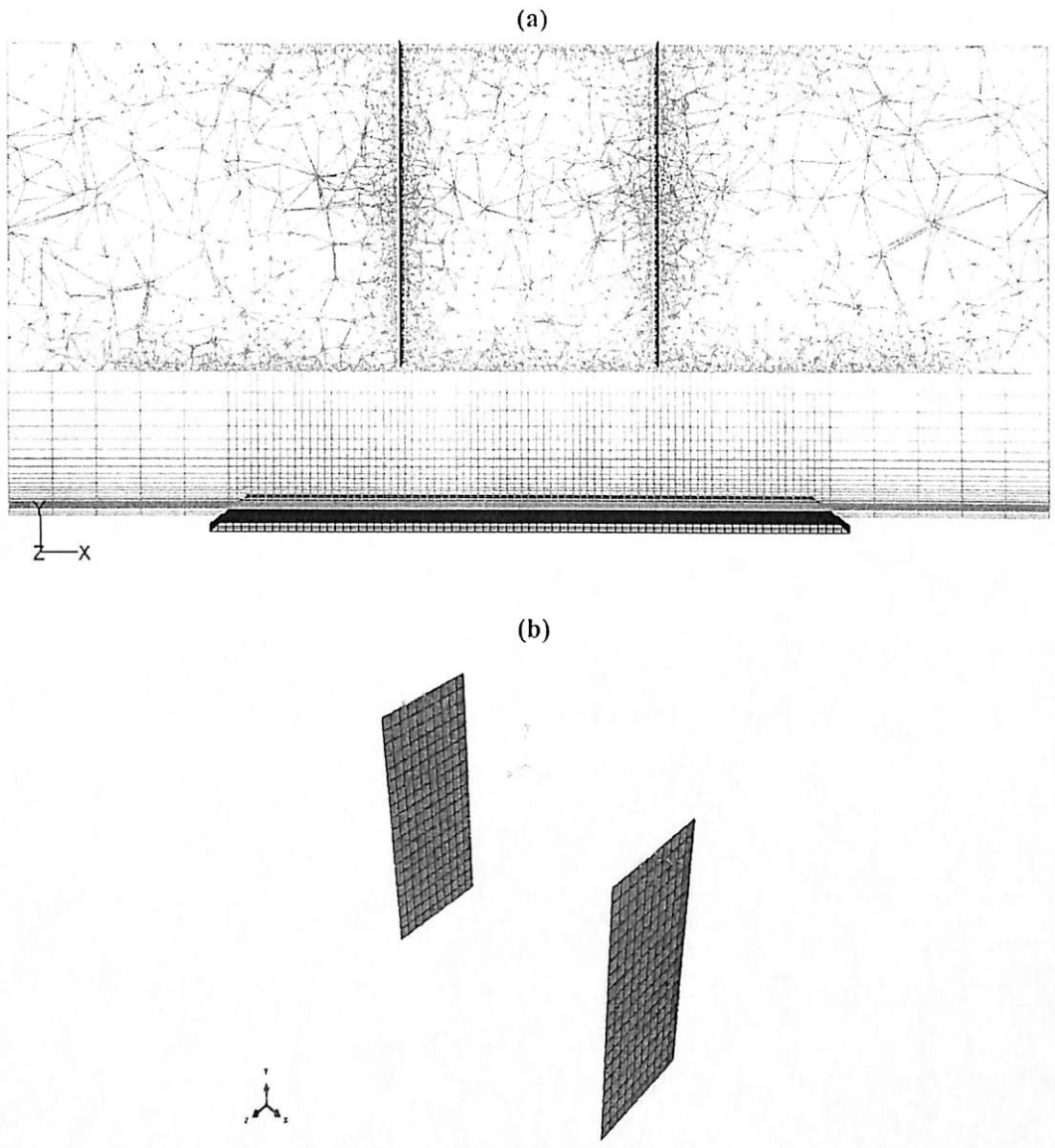

Fig. 6. The meshed model, (a) at the middle of computational domain in FLUENT and (b) vibrating beam in ABAQUS.

(CCW) vortex is developed on the left side of the beam tip due to the suction induced on account of the blade motion. The trajectory of these CW vortices is directed towards the heated surface thereby providing the necessary impetus for dissipation of heat. Moreover, as can be observed from the contour plot in Fig. 7a, the dual fans operating as per configuration A, is most effective in the middle of the heat domain along its width. On the contrary, Fig. 7ā shows that configuration B tends to be effective over the entire target domain. The figure clearly shows the formation of an array of CW and CCW vortex as the two fans move from their normal position to extreme right in case of configuration B. The vortex developed in type B are of bigger dimensions and therefore encompasses a larger heater surface area. It is evident from the figure that, one vortex in CW direction and another in CCW direction is developed in between the fans' blades. The airflow is sucked in from above and is drawn into the vortex and is later pushed over the heater surface as the blade is moved from its normal to extreme position. As the fans return to their natural position (Fig. 7b), the CCW vortex continues to be retained, and the vortices follow the fans to the maximum deflection in the negative x-direction (Fig. 8c). However, as the fan moves periodically to the right and left positions, the two counter vortexes are periodically formed on the right and left of each fan. Similar findings were reported by the earlier work of Açıkalın et al. but involving 2D simulation [15]. In case of configuration B, as the fans return to their natural position (Fig. 7b̄), four vortices are observed, and these vortices follow the fans to the maximum deflection in the negative x-direction (Fig. 7c̄). The two fans vibrate synchronously, and therefore no flow separation exists between them and this could lead to the formation of a net flow between the fans which can further increase their vibration amplitudes. Moreover, the trajectory of these vortices also follow the motion of the fans, and the cross flow trajectory is observed to exceed the centerline ($x = 0$). Besides, the motion of the fans back to its normal position from its extreme swing, resulted in a significant increase in the velocity impinging on the heater surface as can be observed from the contour plots in Fig. 7. The vortex developed in the right swing of the fan, starts to shed and propagate with the change in direction of the fan motion. The heat carried by these vortices, are thus dissipated in every subsequent fan movement.

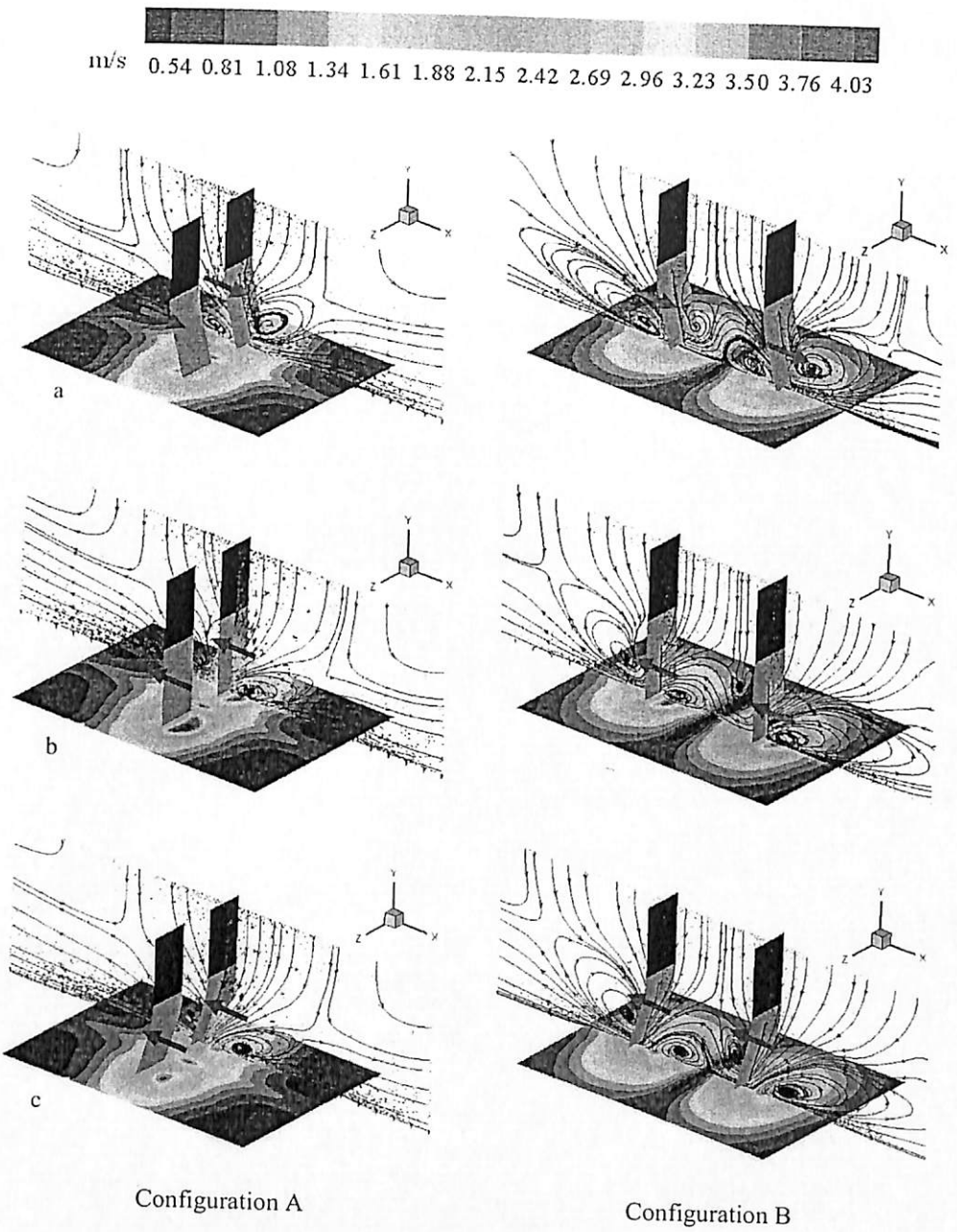

Fig. 7. Flow field induced with dual vibrating fan.

4.2. Thermal analysis

Fig. 8 shows the temperature contours of the nine LED chips placed on the MCPCB subjected to forced convection. The figure highlights three distinct cases; the effect of single fan, configuration A and configuration B, respectively (only the results of tip gap $\delta = 0.1$ are presented). The single fan is qualitatively and quantitatively compared with the two configurations of dual fans and the thermal contours of both the bottom and top portions of MCBCP surfaces are presented. The vibration envelope is overlaid on each contour of the first column showcasing the MCPCB bottom which directly exposed to the fans. The solid line in the center represents the fan at its zero natural position with the remaining dashed lines illustrating the extent of the vibration envelope, whose overall dimensions were twice the vibration amplitude.

It can be seen from the figure that MCPCB surface (82 mm × 60 mm) has undergone significant change in temperature distribution influenced by the fan motion. The high thermal conductivity of MCPCB facilitates faster heat removal from the LED chips and is spread across the board. This is further dissipated to the ambient air by means of convection imposed due to the piezoelectric fan vibration. For the single fan, a droplet cooling zone is formed as a lobed pattern and is observed at the MCPCB center, around the vicinity of fan motion. These lobes, which appear symmetric in the X and Z directions, indicate that the flow induced by the fan is evenly spread. However, the effective region of influence is limited to just the middle zone along the piezoelectric fan swing direction. An elliptical temperature contour is observed showcasing the low temperature region obtained on account of piezoelectric fan vibration, whereas, the hottest spots are the locations indicating the LED chips. The temperature on the entire LED

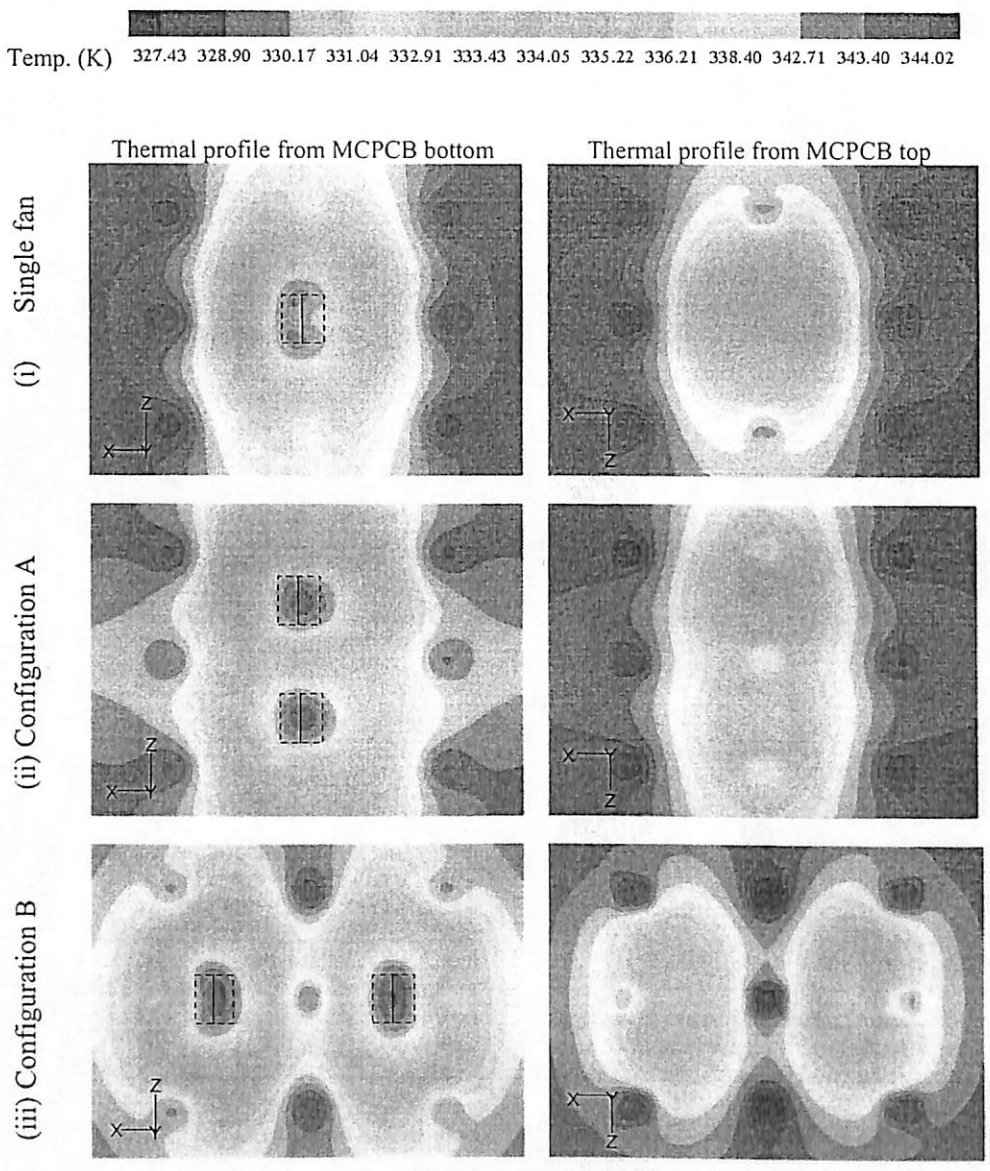

Fig. 8. Temperature contours under force convection at tip gap $\delta = 0.1$ for single vibrating fan first row, and second, and last rows for configurations A and B of the dual vibrating fans respectively. Each row represents the bottom and top of MCBCP surfaces.

package has remarkably dropped relative to the natural convection, and the lowest temperature magnitude is observed directly below the vibration envelop. The bottom of the MCPCB registers significant temperature drop when compared to its top surface. This is because the bottom surface of MCPCB is directly subjected to the impingement flow of the vibrating fan. At Fig. 8(ii), configuration A demonstrates a two lobed pattern along the mid plane of the MCPCB surface commensurate with the two fans arranged parallel to each other. A very high temperature drop is observed for this type of configuration, but its influence is localized along the centerline of Z-axis ($X = 0$) and the distance between the two centers of these lobed patterns is 1.17 cm. However, configuration A performed much better when compared to single fan and showcased higher heat dissipation abilities. On the other hand configuration B exhibits two separate lobes as can be seen in Fig. 8(iii). This can be attributed to the flow acceleration along the heated surface by the two fans' blades moving in tandem (refer Fig. 7a). Configuration B resulted in a bigger cooling envelop on MCPCB surface when compared to configuration A, and is localized along the centerline of X-axis ($Z = 0$) with 3.5 cm separation distance between the center of the two lobes. Moreover, it is clear from the temperature contour that, configuration B influences a large surface area and therefore is effective even in the vicinity outside the fan vibration zone. Thus, configuration B demonstrates superior heat transfer performance when compared to the single fan and configuration A.

A sample experiment of the transient temperature history under natural and forced convection modes for various thermocouples located on the heat source (MCPCB) is shown in Fig. 9. At $t = 0$, the LED package was switched on in natural convection, and the steady state was achieved at $t = 3600$ s. The piezoelectric fans were switched on at $t = 3600$ s, and the temperatures were recorded until a fresh steady state was reached. The piezoelectric fan caused a drastic reduction in the MCPCB temperature from approximately 109 °C in natural convection to 60 °C with the fans.

Fig. 10 shows the results of total thermal resistance R of the LED package cooled by the piezoelectric fan. The results are obtained

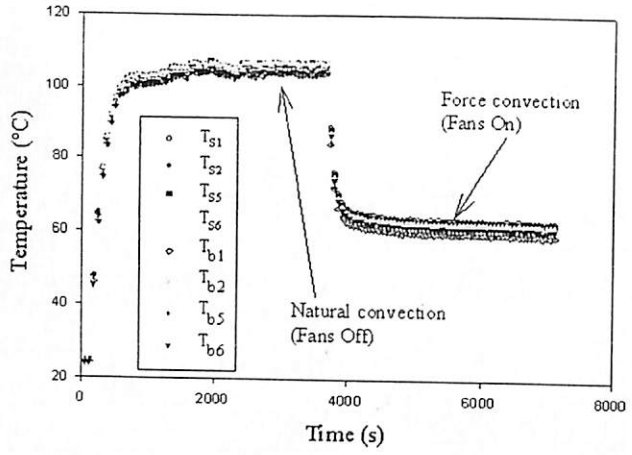

Fig. 9. Temperature history for natural and forced convection conditions.

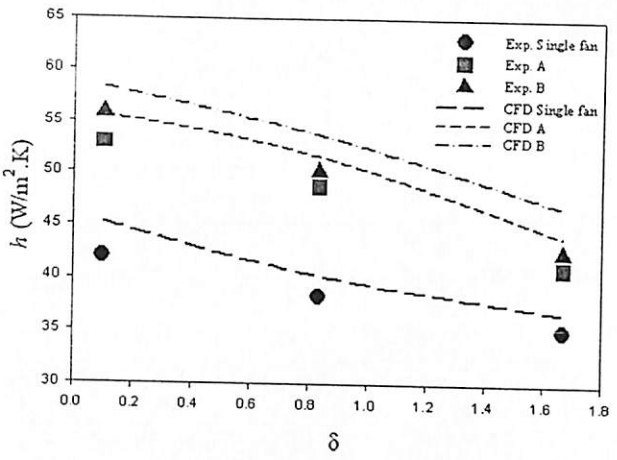

Fig. 11. Average heat transfer coefficients achieved under force convection on the MCPCB.

for both the configurations (A and B) at three different tip gap δ. The resistance is estimated based on the average of MCPCB surface temperature that includes all the nine LED chips (heat sources). It is clear from the figure that employing the piezoelectric fans decreases the thermal resistance to a very large extent. In addition to this, a further decrease in the thermal resistance is observed for all the configurations when fan separation distance δ is reduced. Thermal resistances of both the dual fan configurations (A and B) are approximately comparable and represent remarkable reduction over a single fan and natural convection (piezoelectric fan off). The best performance is found to be at ($\delta = 0.1$) which decreases thermal resistance to about 38% for single fan, 49.5% in case of configuration A, and the highest decrease is with configuration B at 50.6%, relative to natural convection.

Fig. 11 shows variations in the computed and measured average heat transfer coefficients on the MCPCB surface subjected to force convection for different fan tip gap δ. Overall magnitude of $\bar{h}$ increases with a decrease in δ which indicates that the cooling performance is high for minimal gaps. This outcome is expected because the flow velocity at the vicinity of the heated surface decreases with the increase in separation distance and thus results in a low convective heat transfer coefficient. The heat transfer achieved with a dual vibrating fan is significantly higher than that achieved with a single fan and difference is in the range of 26–33.7%. The cooling effect is noticed over a larger area in Configuration B, which is attributed to the dual fan arrangement which facilitates vortex formation and jet flow impinging over a large surface area of the MCPCB. As a consequence, configuration B results in the largest rate of heat transfer yielding a very high reduction in thermal resistance. Besides, the fluid over the heated surface (MCPCB) is displaced rapidly, whilst the higher velocity zone is mostly localized in the vicinity of the heated surface enabling effective heat removal. It is noted that the computed heat transfer is higher than that determined from the experimental measurement. The maximum error between the numerical simulation and experimental work is about 17.4%. This is because, the heat input was assumed to be 80% of the total power input of the LED package, while in reality it might be higher than the assumed rating. Moreover, only the LED chips are declared as heat flux zones at the board (MCPCB) in simulation, while the circuit resistances, cathode and anode also generate heat and is neglected. Besides, the omission of the radiation effect in the numerical model also contributes to this variation. Moreover, the ambient temperature in the experiments was measured with a single thermocouple, and the average fluid temperature inside the domain was used in the simulation. Nevertheless, the results show a good agreement between the estimated and measured results. The natural convection is estimated to be about 23 W/m^2 K. It is observed that, the enhancement in the heat transfer performance for the single fan varies about 1.8 times for the heated LED package. On the contrary, the dual fans enhance heat transfer performance by about 2.3 times for configuration A and 2.4 for configuration B for $\delta = 0.1$. These findings indicate that

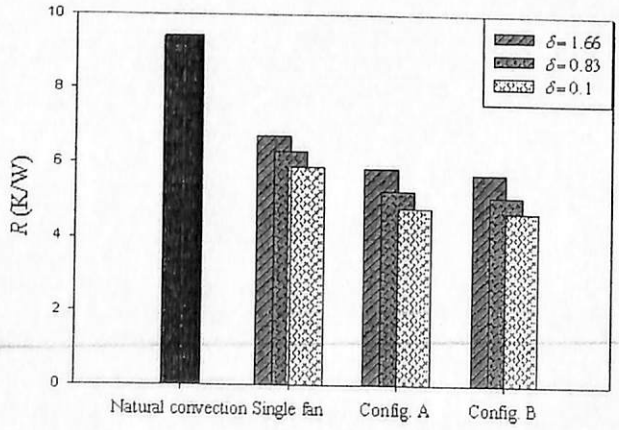

Fig. 10. Total thermal resistance of the LEDs package.

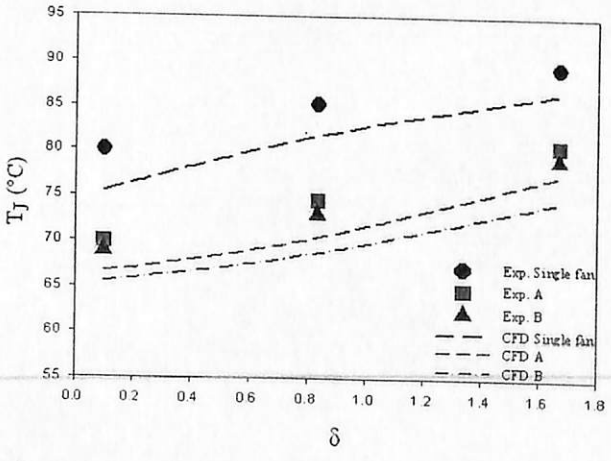

Fig. 12. Average junction temperature of LED package subjected to force convection.

adding a second fan significantly influences the effective heat removal rate and is an important factor to be considered in the actual implementation of such applications.

It is difficult to measure the junction temperature directly using thermocouple because of the silicone lens surrounding the LED die. The junction temperature is estimated based on the solder point (Cathode) temperature according to Eq. (2). The solder point temperature is the closest measured point to the junction device and can be related via the thermal resistance (R_{js}) from device junction to solder point which has a value of 6.5 K/W [26]. Fig. 12 depicts the computed and measured average junction temperature under force convection for varying tip gap δ. It can be seen that all values of the junction temperature increase linearly with the increase in the separation distance δ. The dual vibrating fans depict significant reduction in the junction temperature over a single fan and natural convection ($T_j = 117$ °C). Moreover, it can be seen that lower junction temperature is observed under configuration B at the smallest tip gap. The use of dual fan is successful in reducing the heating of LED package which in turn helps improve its performance and extends its lifetime, besides contributing towards good performance, it also lowers the power consumption.

5. Conclusion

Experimental measurements and numerical analysis were performed to investigate the transient thermal-fluid characteristics of high power LED package cooled by multiple piezoelectric fans. The effect of different configurations and location of the piezoelectric fans on the thermal performance of the LED package was studied. The results show a good agreement between the estimated and measured values. It was found that configuration B influences a large surface area of the MCPCB and is also effective even in the vicinity outside the fan vibration zone. Furthermore, configuration B provides better thermal performance when compared to configuration A and single fan. Besides, significant decrease in the thermal resistance was observed for all the configurations when fan separation distance δ was reduced. The best performance was found to be at ($\delta = 0.1$) which decreased the thermal resistance to about 38% for single fan, 49.5% in case of configuration A, and the highest decrease was with configuration B at 50.6%, in relation to natural convection. It was also found that configuration B showcases lowest junction temperature under the smallest tip gap. In general, it can be concluded that configuration B was best suited for heat dissipation in case of LED package.

References

[1] Kim L, Choi JH, Jang SH, Shin MW. Thermal analysis of LED array system with heat pipe. Thermochim Acta 2007;455:21–5.

[2] Shyu J-C, Hsu K-W, Yang K-S, Wang C-C. Thermal characterization of shrouded plate fin array on an LED backlight panel. Appl Therm Eng 2011;31:2909–15.

[3] Advanced thermal solutions, cooling high power LEDs, 2007. <www.qats.com>.

[4] Jang D, Yu S-H, Lee K-S. Multidisciplinary optimization of a pin-fin radial heat sink for LED lighting applications. Int J Heat Mass Transfer 2012;55:515–21.

[5] Ha M, Graham S. Development of a thermal resistance model for chip-on-board packaging of high power LED arrays. Microelectron Reliab 2012;52:836–44.

[6] Lu X-Y, Hua T-C, Wang Y-P. Thermal analysis of high power LED package with heat pipe heat sink. Microelectron J 2011;42:1257–62.

[7] Lin Z, Wang S, Huo J, Hu Y, Chen J, Zhang W, et al. Heat transfer characteristics and LED heat sink application of aluminum plate oscillating heat pipes. Appl Therm Eng 2011;31:2221–9.

[8] Li J, Lin F, Wang D, Tian W. A loop-heat-pipe heat sink with parallel condensers for high-power integrated LED chips. Appl Therm Eng 2013;56:18–26.

[9] Wang J-C. Thermal investigations on LED vapor chamber-based plates. Int Commun Heat Mass Transfer 2011;38:1206–12.

[10] Yung KC, Liem H, Choy HS, Lun WK. Thermal performance of high brightness LED array package on PCB. Int Commun Heat Mass Transfer 2010;37:1266–72.

[11] Faranda R, Guzzetti S, Lazaroiu GC, Leva S. Refrigerating liquid prototype for LED's thermal management. Appl Therm Eng 2012;48:155–63.

[12] Deng Y, Liu J. A liquid metal cooling system for the thermal management of high power LEDs. Int Commun Heat Mass Transfer 2010;37:788–91.

[13] Xiaobing L, Sheng L. A microjet array cooling system for thermal management of high-brightness LEDs. Adv Pack, IEEE Trans 2007;30:475–84.

[14] Liu S, Yang J, Gan Z, Luo X. Structural optimization of a micrnjet based cooling system for high power LEDs. Int J Therm Sci 2008;47:1086–95.

[15] Acikalin T, Garimella SV, Raman A, Petroski J. Characterization and optimization of the thermal performance of miniature piezoelectric fans. Int J Heat Fluid Flow 2007;28:806–20.

[16] Kimber M, Garimella SV. Measurement and prediction of the cooling characteristics of a generalized vibrating piezoelectric fan. Int J Heat Mass Transfer 2009;52:4470–8.

[17] Kimber M, Garimella SV. Cooling performance of arrays of vibrating cantilevers. J Heat Transfer 2009;131:111401.

[18] Abdullah MK, Abdullah MZ, Ramana MV, Khor CY, Ahmad KA, Mujeebu MA, et al. Numerical and experimental investigations on effect of fan height on the performance of piezoelectric fan in microelectronic cooling. Int Commun Heat Mass Transfer 2009;36:51–8.

[19] Liu S-F, Huang R-T, Sheu W-J, Wang C-C. Heat transfer by a piezoelectric fan on a flat surface subject to the influence of horizontal/vertical arrangement. Int J Heat Mass Transfer 2009;52:2565–70.

[20] Lin C-N. Heat transfer enhancement analysis of a cylindrical surface by a piezoelectric fan. Appl Therm Eng 2013;50:693–703.

[21] Sufian SF, Abdullah MZ, Mohamed JJ. Effect of synchronized piezoelectric fans on microelectronic cooling performance. Int Commun Heat Mass Transfer 2013;43:81–9.

[22] Acikalin T, Garimella SV, Petroski J, Raman A. Optimal design of miniature piezoelectric fans for cooling light emitting diodes, thermal and thermomechanical phenomena in electronic systems. In: ITHERM '04. the ninth intersociety conference on 2004, vol. 661, 2004. p. 663–71.

[23] Yung KC, Liem H, Choy HS, Lun WK. Thermal investigation and placement design of high brightness LED array package on PCB for uniform illuminance. J Electron Package 2011;133:011006.

[24] Wu H-H, Lin K-H, Lin S-T. A study on the heat dissipation of high power multi-chip COB LEDs. Microelectron J 2012;43:280–7.

[25] Fathi M, Aissat A, Abderrazak M. Optimization of the electronic driver and thermal management of LEDs lighting powered by solar PV. Energy Procedia 2012;18:291–9.

[26] Osram GDP. LED LUW W5AM; Technology for energy-efficient, flexible lighting solutions, 2013. Available: <www.osram-os.com>.

[27] Tsai MY, Chen CH, Kang CS. Thermal measurements and analyses of low-cost high-power LED packages and their modules. Microelectron Reliab 2012;52:845–54.